The Role of Tubulin Isotypes in Neuronal Microtubule Growth and Transport Processes

Die Rolle von Tubulin Isotypen in neuronalem Mikrotubuliwachstum und in Transportprozessen

Dissertation
zur Erlangung des Doktorgrades
an der Fakultät für Mathematik, Informatik und Naturwissenschaften
Fachbereich Physik
der Universität Hamburg

vorgelegt von
Jennifer Radwitz

Hamburg

2021

Gutachter der Dissertation:	Prof. Dr. Matthias Kneussel Prof. Dr. Michael Alexander Rübhausen
Zusammensetzung der Prüfungskommission:	Prof. Dr. Matthias Kneussel Prof. Dr. Michael Alexander Rübhausen Prof. Dr. Arwen Ruth Pearson Prof. Dr. Wolfgang Johann Parak Dr. Torben Hausrat
Vorsitzende der Prüfungskommission:	Prof. Dr. Arwen Ruth Pearson
Datum der Disputation:	09.12.2021
Vorsitzender Fach-Promotionsausschuss PHYSIK:	Prof. Dr. Wolfgang Hansen
Leiter des Fachbereichs PHYSIK:	Prof. Dr. Günter H. W. Sigl
Dekan der Fakultät MIN:	Prof. Dr. Heinrich Graener

Eidesstattliche Versicherung / Declaration on oath

Hiermit versichere ich an Eides statt, die vorliegende Dissertationsschrift selbst verfasst und keine anderen als die angegebenen Hilfsmittel und Quellen benutzt zu haben.

Hamburg, den 09.09.2021

Unterschrift der Doktorandin

Contents

Abstract

The brain, although studied for centuries, is still not completely understood. It is constructed of a delicate network of neurons, which are connected by synapses that transmit chemical and electrical signals between cells. The ability of the neuronal network and synapses to adjust to activity is called plasticity and enables the filtering of information by strengthening certain memory paths and weakening others. It was shown that synapses react to stimulation by activating a cascade of regulatory pathways, one of them being the adjustment of cytoskeletal elements as microtubules and actin filaments. This study focuses on microtubules, which perform numerous tasks in the cell. One of them is the directed transport of, for example, synaptic proteins. The building blocks of microtubules are alpha- and beta-tubulin dimers, which are assembled from a pool of tubulin isotypes. This study showed that chemical stimulation of hippocampal slices led to an increase of a distinct tubulin isotype, which confirmed that the cytoskeleton is changing after synaptic stimulation and points to an altered tubulin isotype composition. To put this in relation with microtubule function, the aim of this study was to elucidate the effect of tubulin isotype composition on microtubule growth and transport.

A tubulin-beta-3 knockdown was established and used in neuronal hippocampal dissociated cell culture experiments. Tubulin-beta-3 is one of the most prominent beta-isotypes in brain and specific to neurons. This study showed that cells with reduced tubulin-beta-3 expression upregulated tubulin-beta-4 and that microtubules with these changes in isotype composition grew faster in dendrites and axons. Also, the motor protein KIF5C and the cargo protein N-Cadherin moved faster in axons with changed isotype composition. These results show that tubulin isotype expression influences microtubule growth and motor driven transport. Therefore, it might play a role in supplying synapses with synaptic particles.

Additionally, this study included a mathematical model to simulate microtubule growth. As enhancement of already existing models, it included several tubulin isotypes as building blocks. With this model it was possible to reproduce microtubule growth data of the tubulin-beta-3 knockdown and predict microtubule growth ve-

locities in the case of a tubulin-beta-3 overexpression. It also enabled the analysis of the individual isotype amounts incorporated into the microtubule.

In conclusion this study showed that the tubulin isotype composition of microtubules influences microtubule growth and transport processes. So it is very likely that tubulin isotype expression acts as a regulator in synaptic plasticity and, therefore, memory formation.

German Abstract (Zusammenfassung)

Obwohl das Gehirn seit mehreren Jahrhunderten untersucht wird, ist seine Funktionsweise noch nicht vollständig verstanden. Es besteht aus einem komplexen Netzwerk von Neuronen, die über Synapsen miteinander verbunden sind. Diese übermitteln chemische und elektrische Signale von einer Zelle zur anderen. Die Fähigkeit des neuronalen Netzwerks und der Synapsen sich an Aktivität anzupassen wird Plastizität genannt und ermöglicht das Filtern von Informationen durch das Verstärken oder Abschwächen bestimmter Gedächtnispfade. Es wurde gezeigt, dass Synapsen auf Stimulierung mit dem Aktivieren einer Kaskade an regulierenden Signalwegen reagieren, einer davon ist die Anpassung von Zytoskelettelementen wie Mikrotubuli oder Aktin Filamenten. Diese Arbeit konzentriert sich auf Mikrotubuli, welche eine Vielzahl an Aufgaben in der Zelle verrichten, zum Beispiel, gerichteten Transport von synaptischen Proteinen. Die Grundbausteine von Mikrotubuli sind alpha- und beta-Tubulin Dimere, die sich aus einem Pool von Tubulin Isotypen zusammensetzen. Diese Studie zeigte, dass chemische Stimulation von hippocampalen Schnitten zu einem Anstieg eines bestimmten Tubulin Isotypen führte. Dies bestätigte, dass das Zytoskelett sich nach synaptischer Stimulierung veränderte und verweist auf eine geänderte Tubulin Isotypen Zusammensetzung. Um das in Verbindung mit der Mikrotubuli Funktion zu setzten, war das Ziel dieser Studie, den Effekt der Tubulin Isotypen Zusammensetzung auf das Mikrotubuliwachstum und den Transport aufzuklären.

Ein Tubulin-beta-3 Knock Down wurde etabliert und in neuronalen hippocampalen dissoziierten Zellkulturexperimenten verwendet. Tubulin-beta-3 ist einer der bedeutendsten Isotypen im Gehirn und spezifisch für Neurone. Diese Arbeit zeigte, dass Zellen mit reduzierter Tubulin-beta-3 Expression Tubulin-beta-4 hoch regulierten und, dass Mikrotubuli mit diesen Veränderungen in der Isotypen Verteilung in Dendriten und Axonen schneller wuchsen. Auch das Motorprotein KIF5C und das Cargoprotein N-Cadherin bewegten sich schneller in Axonen mit veränderter Isotypen

Konfiguration. Diese Ergebnisse zeigen, dass die Tubulin Isotypen Expression das Mikrotubuliwachstum und den motor-gesteuerten Transport beeinflussen. Vermutlich spielen sie damit eine Rolle in der Versorgung der Synapsen mit synaptischen Proteinen.

Zusätzlich enthält diese Studie ein mathematisches Modell, um das Mikrotubuliwachstum zu simulieren. Als Erweiterung schon existierender Modelle, enthält es verschiedene Tubulin Isotypen als Grundbausteine. Mit diesem Model war es möglich die Mikrotubuliwachstumsdaten des Tubulin-beta-3 Knock Downs zu reproduzieren und das Verhalten des Mikrotubuliwachstums im Falle einer Tubulin-beta-3 Überexpression vorherzusagen. Es ermöglichte außerdem die Analyse der individuellen Isotypenanzahl, die in das Mikrotubulus eingebaut wurde.

Zusammenfassend zeigt diese Arbeit, dass die Tubulin Isotypen Zusammensetzung das Mikrotubuliwachstum und Transport Prozesse beeinflusst. Damit hat sie sehr wahrscheinlich die Fähigkeit als Regulator der synaptischen Plastizität und damit der Gedächtnisformierung zu fungieren.

1. Introduction

1.1. Brain composition and hippocamus structure

The brain is part of the central nervous system and probably the most complex organ of the human body. It is composed of an intricate network of billions of cells which work together in a highly specialized manner. Neurons are the basis of brain function by transmitting signals between one another. They consist of a cell soma which possesses the typical components of an eukaryote cell and, what makes them unique, long and thin protrusions called neurites. Typically, neurons have many dendrites which receive signals from other neurons and one axon which passes signals onto further neurons. The connection points are called synapses. But neurons are not the only cells in the brain. They are assisted by glial cells which, among other things, provide a layer of membrane that insulates axons, regulate neurotransmitters at synapses, and remove debris left by dead or degenerating neurons and glia. Without the glial cells the delicate system of neurons would not function. Developmentally originated, the brain is divided into several parts. The one of interest in this study is the hippocampus which is part of the cerebral cortex. Since the brain has a symmetric structure there is one hippocampus in the left and one in the right hemisphere. [Bear et al., 2016] The hippocampus is involved in spatial learning and memory consolidation. All experiments in this thesis were conducted with mouse hippocampal cells, which is why figure 1.1 shows the typical structure of a mouse hippocampus. It consists of two thin sheets of neurons folded onto each other, which are called dentate gyros and ammon's horn (latin: cornu ammonis, CA). The CA is divided into several regions, whereby this chapter focuses on the CA1 and CA3 regions. Information enters the hippocampus from the entorhinal cortex through axons that connect to neurons of the dentate gyros (perforant path). Axons leaving from the dentate gyros, called mossy fibers, connect to CA3 synapses and neurons of CA3 are connected to CA1 neurons by axons called Schaffer collaterals. Because of its simple architecture and organization, the hippocampus is often used to study synaptic transmission. [Korte and Schmitz, 2016]

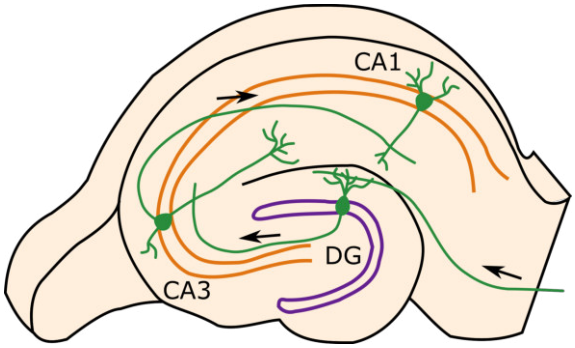

Figure 1.1. – Mouse hippocampal cross section. The mouse hippocampus consists of two cell layers folded onto each other. The dentate gyros (DG) and the cornu ammonis (CA), marked are the regions CA1 and CA3. The dentate gyros of the hippocampus gets input from the entorhinal cortex. From the dentate gyros axons called mossy fibers connect to CA3 neurons, which then send their axons called Schaffer collaterals to CA1 neurons.

1.2. Synaptic plasticity and long-term potentiation

For mammals being able to make new memories, loose old and store important ones, the neuronal network and synapses have to be adaptive. The quality of synapses to change in strength is called synaptic plasticity. The typical structure of a CA1 synapse of the hippocampus is shown in figure 1.2. The synapse has a presynaptic site, which is usually an axon terminal, and a postsynaptic site, which mostly sits at a dendrite. The names indicate that the signal flows from pre- to postsynaptic site, meaning from axon to dendrite. At most synapses, the signal that propagates along the axon in form of electrical impulses is converted into a chemical signal in form of neurotransmitters that cross the space between pre- and postsynapse and is then converted back into an electrical one. When an electrical impulse called action potential arrives at the presynaptic terminal it depolarizes the terminal membrane which causes voltage-gated calcium channels to open. Upon channel opening calcium ions flow into the presynapse which causes neurotransmitter release into the synaptic cleft. On the postsynaptic site these neurotransmitters bind to neurotransmitter receptors. Out of the many existing combinations of neurotransmitter and receptor, glutamate and α-amino-3-hydroxy-5-methyl-4-isoxazolepropionic acid (AMPA) receptors are shown in figure 1.2. Binding of glutamate leads to the opening of the AMPA receptors and sodium ions can flow from the synaptic cleft into the postsynaptic site. This depolymerizes the postsynaptic membrane and leads to an excitatory postsynaptic potential. After the closing of the sodium ion channels, potassium ion efflux leads to the re-polarization of the membrane. In most synapses

one excitatory postsynaptic potential is not able to produce an action potential, therefore, many synapses must be stimulated simultaneously, or the same synapse several times in a short time period. [Bear et al., 2016]
Additionally to AMPA receptors, CA1 neurons also have postsynaptic N-methyl-D-aspartate (NMDA) receptors which conduct calcium ions. They open upon glutamate binding, but only if at the same time the postsynaptic membrane is depolymerized enough to displace magnesium ions that clog the channel. The rise of postsynaptic calcium ion concentration leads to the activation of kinases which enable higher ionic conductance in already existing AMPA receptors and the incorporation of new AMPA receptors into the postsynaptic membrane. This process is called long-term potentiation (LTP) because it strengthens the synapse in its potential to generate action potentials. As antagonist the process of long-term depression weakens synapses. With this system the synapses, and with them the neuronal network, stay adjustable. [Bear et al., 2016] In order for synapses to strengthen and grow, new synaptic proteins are needed at the synaptic site. Most of them are delivered there through active transport along the cytoskeleton which is introduced in the following chapters.

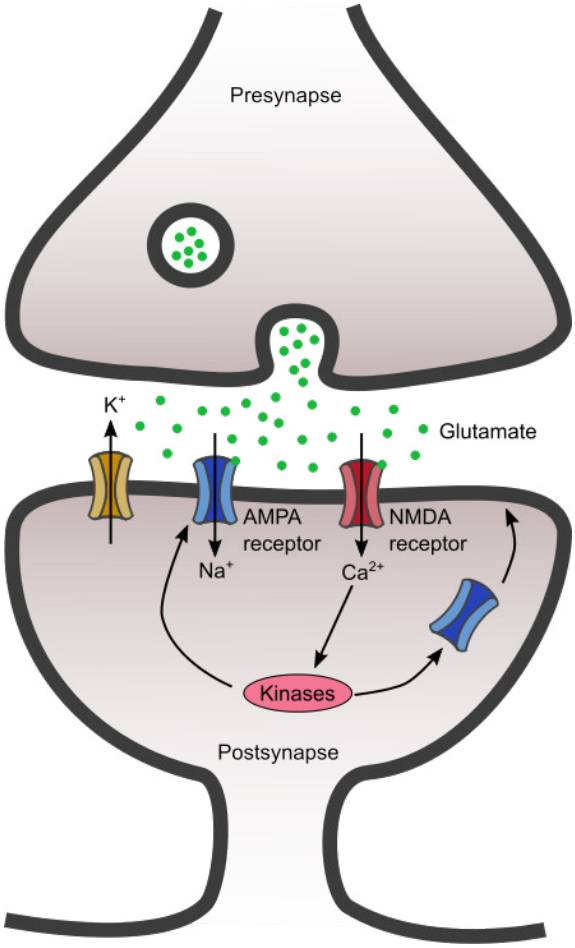

Figure 1.2. – Typical CA1 hippocampal synapse. When an action potential reaches the presynapse the neurotransmitter glutamate is released into the synaptic cleft. It binds to AMPA and NMDA receptors of the postsynapse. Sodium ions flow through the AMPA receptors into the postsynaptic site what depolymerizes the postsynaptic membrane. When the membrane is depolymerized enough to displace magnesium ions that clog the NMDA receptors, calcium ions flow into the postsynapse. This leads to the activation of kinases which enable new incorporation of AMPA receptors into the postsynaptic membrane and higher conductance of already existing AMPA receptors. This process of synapse strengthening is called LTP. After AMPA and NMDA receptor closing, efflux of potassium ion leads to the re-polymerization of the membrane.

1.3. Microtubules

Microtubules (MTs), together with actin and intermediate filaments, build up the cytoskeleton. Its functions are manifold and vary from morphology over cell movement to molecular transport. This study will focus on MTs. They are mostly known for dividing chromosomes during cell division, but here the focus lies on the guidance and transport characteristics of MTs. In small round cells diffusion is sufficient

to distribute proteins over the entire cell, whereas neurons are polarized and structurally highly complex cells with axons that can grow meters long. Via diffusion it would take a protein roughly 6.3 years to cover the distance of 10 cm ($D = 25\,\mu m^2/s$ [Lanzanò et al., 2017]). With the system of motor proteins running along MTs this distance can be covered in roughly 21.4 hours ($v = 1.3\,\mu m/s$ [this study]). Another significant advantage of this system is the possibility to regulate transport through a complex system of motor, adapter, and cargo proteins. Also, the structure of the MT itself is a tool to manipulate transport.

1.3.1. Microtubule structure

The building blocks of MTs are alpha- and beta-tubulin dimers which bind longitudinally together and build a protofilament. Several protofilaments assemble laterally and build up a hollow tube, the MT (Figure 1.3). Due to its dimer structure a MT has an intrinsic direction. The end where beta-tubulin is exposed is called plus-end and the end with exposed alpha-tubulin is called minus-end, which is not related to electric charge. In living cells MTs usually consist of 13 protofilaments and have a diameter of 25 nm. Protofilaments align next to one-another in the way that alpha- binds with alpha-tubulin and beta- binds with beta-tubulin, but with a slight longitudinal shift. This leads to an offset of three monomers between protofilaments one and 13, so that alpha- binds to beta-tubulin and vice versa. This interface is termed MT seam (Figure 1.3). With this structure protofilaments run straight along the MT, whereas, for example, 14 protofilaments would lead to protofilaments that twist around the MT surface [Chaaban and Brouhard, 2017]. Since motor proteins mostly run along a protofilament, they would spiral around the MT. So the 13 protofilament structure might offer selective advantage of efficient long range transport. But it was also shown that protofilament number varies between species, cell type and developmental stage [Chaaban and Brouhard, 2017]. Extreme numbers of protofilaments *in vivo* were found in *Prosthecobacter* with four protofilaments [Deng et al., 2017] and in mantidfly sperm with 40 protofilaments [Dallai et al., 2005]. *In vitro* MTs of 11 to 17 protofilaments were observed [Chrétien and Wade, 1991, Pierson et al., 1978]. Usually, MTs are formed at the centrosome, where the minus-end is anchored and the plus-end reaches out into the cell. In complex polarized cells, like neurons, MTs can also nucleate in a non centrosomal way, involving the gamma-tubulin ring complex (γTuRC) or Golgi-outposts [Kollman et al., 2011, Yu et al., 2016, Yau et al., 2014]. Another way to multiply MT number is to cut the MTs with MT severing enzymes like katanin or spastin [Roll-Mecak and McNally, 2010]. A specialty of

neurons is that dendrites contain MTs of mixed polarity, which means plus-ends can point towards both directions, the cell soma and the dendrite tip. Whereas in axons, MTs have uniform polarity, which means all plus-ends point to the tip [Yau et al., 2016] (Figure 1.4). Each tubulin molecule consists of a N-terminus, an intermediate domain and a C-terminus (Figure 1.5). The C-terminal tail contains a large percentage of negatively charged residues, which makes it intrinsically disordered and, therefore, it is not resolved in the crystal structure [Chakraborti et al., 2016]. In figure 1.5 it is depicted schematically as a pink line. The C-terminus builds most of the outer surface of the MT and the C-terminal tail is believed to stick out of the MT surface.

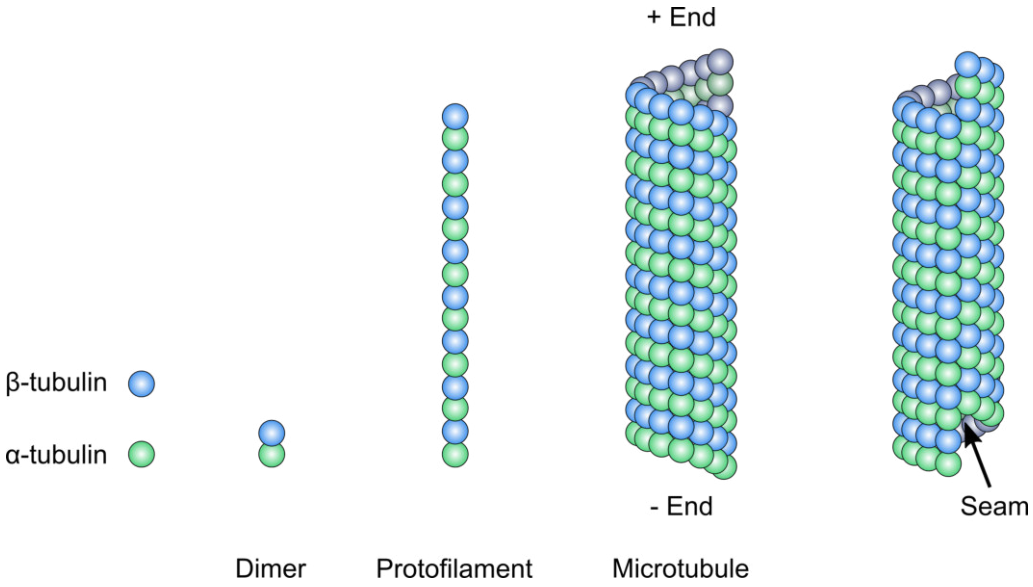

Figure 1.3. – Microtubule structure. MTs are build out of alpha- and beta-tubulin monomers (green and blue spheres, respectively), which bind to form a heterodimer. These dimers bind longitudinally together to protofilaments which assemble laterally to build the MT. Due to their heterodimer structure MTs are intrinsically ordered, the end where alpha-tubulin is exposed is called minus-end (- End) and the end with exposed beta-tubulin is called plus-end (+ End). Typically, MTs consist of 13 protofilaments which are slightly shifted to one-another. This leads to a three-monomer offset between protofilament one and 13 where alpha- binds to beta-tubulin and vice versa, which is called the MT seam. In the rest of the MT lattice alpha- binds to alpha-tubulin and beta- binds to beta-tubulin.

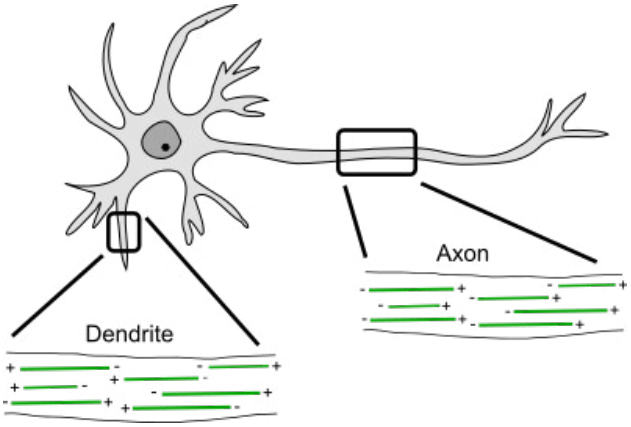

Figure 1.4. – Microtubule polarity. Neurons are polarized cells with several dendrites and one axon. MTs in dendrites can point into both directions, plus-end out or plus-end in, whereas MTs in axons are unidirectional with plus ends out.

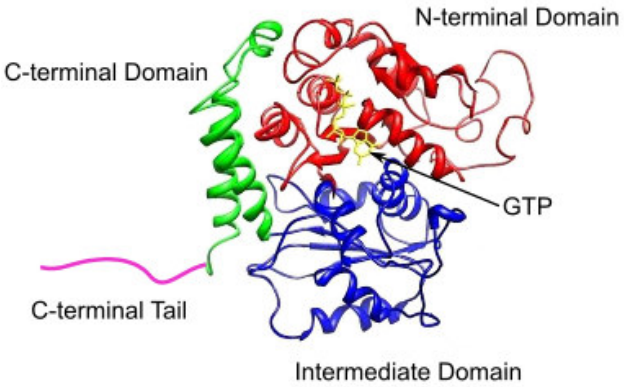

Figure 1.5. – Tubulin crystal structure. Ribbon structure of a tubulin monomer, with N-terminal domain, intermediate domain, and C-terminal domain. The C-terminal tail contains a large percentage of negatively charged residues, which makes it intrinsically disordered and not resolved in the crystal structure. Here it is schematically shown as a pink line. The bound GTP nucleotide is shown in yellow. Adapted from [Kumar et al., 2015].

1.3.2. Tubulin isotypes and post-translational modifications

Since MT functions are so multifaceted it stands to reason that several genes encode for alpha- and beta-tubulin. In mouse, eight alpha- and eight beta-tubulin isotypes have been identified so far [Hausrat et al., 2020] and in human, nine alpha- and nine beta-tubulin isotypes have been found [Janke and Magiera, 2020]. Figure 1.6 depicts the amino acid sequences of the C-terminal tails of mouse alpha- and beta-tubulin isotypes, which are the regions of highest divergence between isotypes. The existence of distinct tubulin isotypes is only known for roughly 40 years and still

a field of fruitful research. This thesis is focused on beta-tubulin isotypes, which have a higher sequence and expression variety in neurons. Alpha-tubulin isotypes in brain are mostly Tuba1a, Tuba1b and Tuba1c which share a high sequence homology [Hausrat et al., 2020]. Additionally, the antibody availability for beta-tubulin isotypes is higher [Hausrat et al., 2020]. Figure 3.1 of the results chapter shows mRNA expression levels of mouse beta-tubulin isotypes in different tissues. The following is an overview over their distinct expression and functions. Tubb1 is mainly expressed in lung and spleen. It is connected to the highly flexible MT coil (marginal band) in platelets [Schwer et al., 2001]. Tubb1 is the most divergent beta-tubulin isotype in mammals and is speculated to have evolved especially to sustain the high degrees of bending required for platelet formation [Janke and Magiera, 2020]. Tubb2, Tubb3, Tubb4 and Tubb5 are highly expressed in brain. Tubb2, Tubb4b and Tubb5 are abundantly expressed, whereas Tubb3 and Tubb4a are only weakly expressed in other tissues. It was shown, that dimers of Tuba1b and Tubb2b preferentially assemble into 14 and 15 protofilament MTs, whereas Tuba1b and Tubb3 dimers assemble into 13 protofilament MTs [Ti et al., 2018]. The influence of tubulin isotypes on MT dynamics is described in detail in the discussion. Human recombinant MTs formed by Tuba1b plus Tubb2b dimers were more resistant to spontaneous or catalyzed depolymerization than Tuba1b plus Tubb3 MTs [Ti et al., 2018, Pamula et al., 2016]. Additionally it was shown that Tubb1 is important for viability during neuronal differentiation, Tubb2 plays a role in neurite outgrowth and Tubb3 is helpful for viability in chemical stress situations [Guo et al., 2010]. Tubb4 was connected to cilia functionality and it was suggested that Tubb4 possesses properties essential for formation of the axoneme [Renthal et al., 1993]. Breuss et al. showed the expression of Tubb5 in neurogenic progenitor cells and that the depletion of Tubb5 perturbs their cell cycle [Breuss et al., 2012]. Tubb6 is only minimally expressed in brain but shows an abundant expression in other tissues, especially the ovary and bladder. Literature describes its expression in muscle fiber MTs and that overexpression of Tubb6 can alter the organization of specific cortical muscle MTs [Randazzo et al., 2019]. This illustrates the huge variety of beta-tubulin isotype expression patterns and functions and the importance to further elucidate their role in cellular processes.

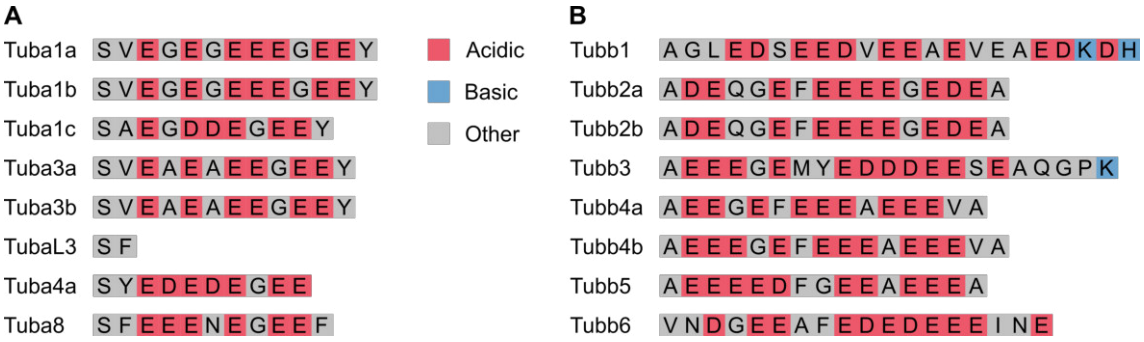

Figure 1.6. – Amino acid sequences of mouse alpha- and beta-tubulin isotype C-terminal tails. (A): Amino acid sequences of mouse alpha-tubulin C-terminal tails. Start is the serine residue at 439, for TubaL3 at 445. **(B):** Amino acid sequences of mouse beta-tubulin C-terminal tails. Start is the alanine residue at 430, for Tubb6 valine. The color code marks acidic (red), basic (blue) and other (grey) residues.

In addition to tubulin isotypes, many tubulin molecules get post-translationally modified, which increases the number of possible MT variations even more. Many post-translational modifications (PTMs) occur at the C-terminal tail of tubulin, for example glutamylation, glycylation, detyrosination, tyrosination, Δ2-tubulin and Δ3-tubulin. Others, as acetylation, phosphorylation and polyamination, occur at the tubulin body [Gadadhar et al., 2017]. Figure 1.7 depicts a MT with tubulin dimers of different isotypes with the C-terminal tails sticking out of the MT surface. On the right side of the MT, PTMs on the C-terminal tails are indicated by side chains for polyglutamylation and polyglycylation and a black rectangle for detyrosination, tyrosination, Δ2-tubulin and Δ3-tubulin. PTMs are variably distributed over functionally divers MTs, but are mostly enriched in stable, long-lived MTs, such as neuronal MTs [Gadadhar et al., 2017]. For polyglutamylation, one or several glutamate residues are added to glutamate at the C-terminal tail of alpha- or beta-tubulin and build negatively charged side chains. This regulates the interaction of MTs with several microtubule binding proteins, for example tau, MAP2 and kinesin-1 [Boucher et al., 1994, Bonnet et al., 2001, Sirajuddin et al., 2014], influences flagellar motility [Kubo et al., 2010], and regulates spastin activity [Lacroix et al., 2010]. Also, polyglutamylation on beta-tubulin increases with neuronal differentiation [Audebert et al., 1994], hyperglutamylation is linked to neurodegeneration [Rogowski et al., 2010, Magiera et al., 2018], and changes in synapse activity regulate polyglutamylation [Maas et al., 2009]. Polyglycylation, the addition of glycine residues to glutamate, has so far only been observed in axonemal MTs [Gadadhar et al., 2017, Janke and Magiera, 2020]. In the detyrosination, tyrosination cycle, a tyrosine is removed or added to the end of the C-terminal tail of alpha-tubulin.

Detyrosination influences the binding and motility of kinesin-1 and kinesin-2 [Dunn et al., 2008, Sirajuddin et al., 2014], prevents kinesin-13 from disassembling MTs [Peris et al., 2009] and is important for proper neurite outgrowth [Marcos et al., 2009]. Tyrosination is required for dynein binding [McKenney et al., 2016], and controls the interaction with some plus-end tracking proteins [Peris et al., 2006]. The role of acetylation is more ambiguous, especially because the most investigated acetylation site (K40 on alpha-tubulin) sits on the inside of the MT. But it could be shown, that the organization of the particular 15-protofilament MTs in *C.elegans* touch receptor neurons depends on K40 acetylation [Topalidou et al., 2012]. Another acetylation site (K252 on beta-tubulin), which localizes at the interface of the tubulin dimer slows down the incorporation into MTs by neutralizing the positive charge at K252 [Chu et al., 2011]. A relatively newly discovered PTM is polyamination. It adds positively charged branch chains to glutamine and is involved in the stabilization of MTs [Song et al., 2013].

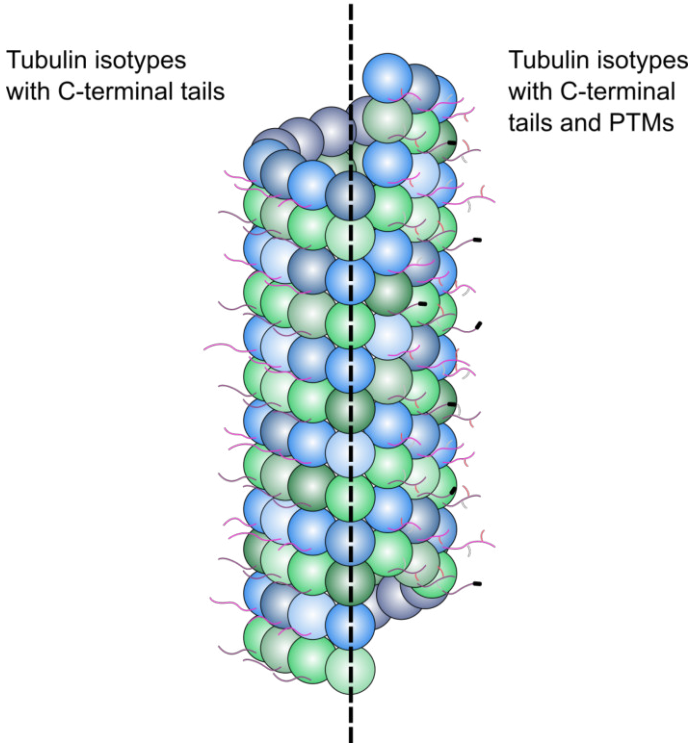

Figure 1.7. – MT composed of different tubulin isotypes with C-terminal tails and PTMs. Several shades of blue and green mimic different beta- and alpha-tubulin isotypes, respectively. C-terminal tails sticking out of the MT surface are shown as pink (beta-tubulin) and violet (alpha-tubulin) lines. On the right side of the MT, PTMs on the C-terminal tails are schematically indicated by side chains for polyglutamylation and polyglycylation and a black rectangle for detyrosination, tyrosination, Δ2-tubulin and Δ3-tubulin. PTMs on the tubulin body are not shown.

1.3.3. Tubulin-beta 3

The focus of this study lies on Tubb3, which is one of the most prominent beta-tubulin isotypes in brain, specific to neurons [Lee et al., 1990, Burgoyne et al., 1988], and its down- or upregulation can influence MT dynamics [Vemu et al., 2017, Panda et al., 1994, Banerjee et al., 1990]. It was shown that a Tubb3 knockdown influences the cortical development in mice. It leads to delayed bipolar morphology and radial migration. A rescue with Tubb3 was successful, whereas other tubulin isotypes were unable to rescue the phenotype [Saillour et al., 2014]. Apart from expression levels, mutations in the tubulin genes can lead to several neurological disorders called tubulinopathies [Minoura, 2017]. Tischfield et al. investigated eight heterozygos missense mutations of TUBB3 in humans which led, in differing severity, to congenital fibrosis of the extraocular muscles type 3 (CFEOM3) and malformations of the commissural axon and basal ganglia. A knockin mouse model of the most common mutation (R262C) revealed impaired axon guidance, but normal cortical architecture. Also this mouse had reduced Tubb3 protein levels, increased detyrosinated alpha-tubulin levels and decreased KIF21b MT interactions [Tischfield et al., 2010]. Poirer et al. published six further TUBB3 missense mutations in human which led to a different phenotype, namely malformations of cortical development (MCD) associated with neuronal migration and axon guidance defects. Also, some of these mutations lead to reduced heterodimer yield, but mutated dimers are still incorporated into MTs [Poirier et al., 2010]. Later, two new TUBB3 mutations were found that combine MCD and CFEOM3 syndromes [Whitman, 2016]. It was also shown that Tubb3 expression was upregulated in human and rat epileptic tissue. Tubb3 downregulation reduced the behavioral phenotypes of epileptic seizures in two chemical induced seizure protocols and Tubb3 overexpression had the opposite effect [Xu et al., 2017]. During the work on this thesis a Tubb3 knockout mouse model was published by Latremoliere et al. [Latremoliere et al., 2018]. They showed that Tubb3 deficient mice have no detectable neurobehavioral or neuropathological deficits. Also the lack of Tubb3 protein was compensated by 10 to 20 % upregulation of most of the other beta-tubulin isotypes, leading to equivalent total beta-tubulin levels as in wild type mice. They found that adult dorsal root ganglia lacking Tubb3 have decreased growth cone MT dynamics and decreased neurite outgrowth. Another characteristic of Tubb3 worth mentioning is its increased expression in several tumor tissues. For example, in gliomas and lung cancer, the expression of Tubb3 is associated with increased malignancy and in various epithelial cancer cell lines it is associated with a chemo-resistance to taxanes (MT stabilizing drugs) [Katsetos et al., 2003].

1.3.4. Microtubule dynamics

Although part of the cytoskeleton, MTs are very dynamic structures. In 1984 Mitchison and Kirschner observed that in a MT population under the same conditions, they were growing, shrinking and switching between the two states infrequently, which they termed as dynamic instability [Mitchison and Kirschner, 1984]. Figure 1.8 depicts this process schematically. Alpha- and beta-tubulin molecules contain a guanosine-5'-triphosphate (GTP) binding site, from which, in dimer formation, the alpha binding site is buried in the dimer interface, but the beta binding site is free for GTP binding and hydrolysis. This thesis focuses on the MT plus-end, which is the more dynamic end. In the growth state of MTs, GTP-tubulin dimers bind to the MT tip and get hydrolyzed in time, which leads to the formation of a so called GTP cap. When the binding of new GTP-tubulin dimers lags behind GTP hydrolysis the cap is lost and a catastrophe occurs, the MT starts shrinking. Either the MT disassembles completely, or a so-called rescue occurs where the MT starts growing again. Since the discovery of this process, it was intensely investigated.
In cryo-electron microscopy studies it was shown that growing MT ends exhibit a range of structures, from blunt over one side elongated to outwardly curved and flattened sheets [Mandelkow et al., 1991, Chrétien et al., 1995]. Literature very often describes the ends as tapered, with the taper length being the distance between the longest protofilament and the fully closed lattice [Guesdon et al., 2016, Maurer et al., 2014]. This length was estimated to 124 nm [Brouhard and Rice, 2018]. For a while, it was assumed that GTP-tubulin has a straight conformation which bends upon GTP hydrolysis and leads to an unstable guanosine diphosphate (GDP)-tubulin lattice, that is stabilized by the GTP cap. But it was shown that unpolymerized GTP-tubulin has an intrinsic curvature [Buey et al., 2006, Rice et al., 2008]. In atomic-resolution crystal structures of soluble GDP- and GTP-tubulin it was shown that they differ locally in the neighborhood of the nucleotide. A loop movement in GTP-bound tubulin favors its binding to MT ends and facilitates its curved to straight transition [Nawrotek et al., 2011]. It has been proposed that the straightening of the GTP dimer would be driven by the alignment of lateral bonds between neighboring dimers [Rice et al., 2008]. So the MT end is shaped by two opposing forces, the tendency to curve outward due to GTP-tubulin curvature and the tendency to straighten due to lateral interactions between subunits that close up the lattice [Brouhard and Rice, 2018]. It even was suggested that protofilaments of growing and shrinking MTs have the same intrinsic curvature and that lateral bonds are responsible for the different shapes [Jánosi et al., 1998]. Following GTP hydrolysis and phosphate release, the dimers compact in the lattice, shortening in

length through a movement of an alpha-tubulin subdomain [Alushin et al., 2014]. This compaction was found in mammalian MTs, whereas studies with yeast MTs did not show compaction of the GDP lattice [Howes et al., 2017, Von Loeffelholz et al., 2017]. Catastrophe is still believed to occur when the GTP cap is lost, then GDP-tubulin relaxes back into the curved state, peeling outward into often called "ram's horns" [Mandelkow et al., 1991]. Rescues are rarely observed *in vitro*, but often in cells, so it is likely that microtubule-binding proteins play a role as rescue factors [Brouhard and Rice, 2018]. Also it was shown, that sites of MT damage can be repaired by fresh GTP-tubulin and that rescues cluster at these sites of repair [Schaedel et al., 2015, Aumeier et al., 2016].

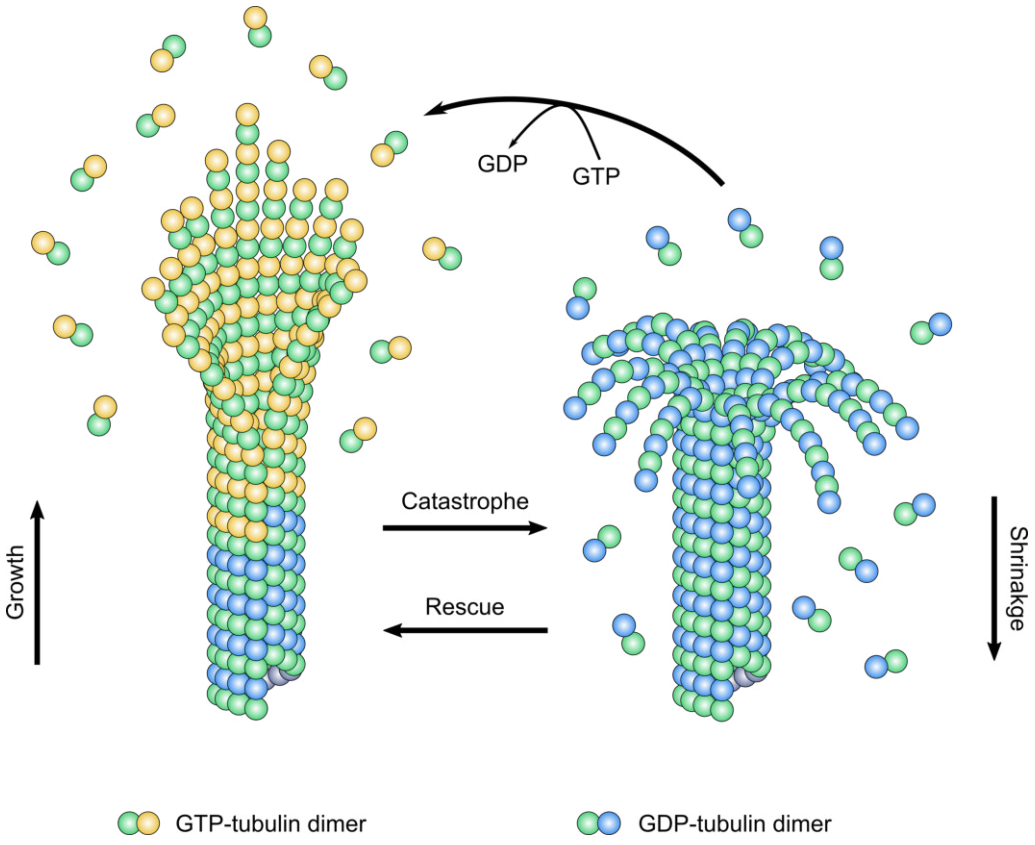

Figure 1.8. – MT dynamics. In the growing phase of the MT plus-end GTP-tubulin dimers (yellow-green) bind to the protofilaments. In time GTP is hydrolyzed, which leads to the formation of a GTP cap and a GDP-tubulin (blue-green) lattice. When the GTP cap is lost, the MT starts shrinking, which is called catastrophe. If at some point the MT starts growing again it is called rescue.

1.4. Microtubule binding proteins

Microtubule binding proteins (MTBPs) are basically all proteins that were experimentally shown to bind to MTs. The often used term MAP (microtubule associated protein) usually describes a subset of MTBPs that cosediment with MTs through multiple rounds of polymerization and depolymerization [Goodson and Jonasson, 2018]. Many different MTBPs with a great variety of functions exist. To give a broad overview, MTBPs can be functionally categorized into stabilizers, destabilizers, capping proteins, and cross-linkers. Other MTBPs include motors, cytoplasmic linkers, and cytoskeletal integrators [Goodson and Jonasson, 2018]. MTBPs can also be categorized by the location where they bind to the MT. Lattice binding proteins are stabilizers as tau and MAP2 [Dehmelt and Halpain, 2005], destabilizing severing proteins as katanin and spastin [Roll-Mecak and McNally, 2010], cross-linkers as PRC1 [Walczak and Shaw, 2010], and motor regulators as tau [Dixit et al., 2008]. MT end-binding proteins can be divided into minus-end and plus-end binding proteins. Minus-end binding proteins are stabilizers as γ-TuRC and CAMSAPs [Kollman et al., 2011, Akhmanova and Hoogenraad, 2015], and destabilizers as stathmin [Cassimeris, 2002]. Plus-end binding proteins, also called +TIPs, are stabilizers as EB1, EB3, XMAP-215 and CLIP-170 [Akhmanova and Steinmetz, 2015], and destabilizers as stathmin, kinesin 8 and kinesin 13 [Gupta et al., 2013, Walczak et al., 2013].

In this study an EB3-Tomato fusion protein was used to visualize the growing MT plus-end. Mammalian cells express up to three different end-binding proteins (EB1, EB2 and EB3). EBs contain a positively charged amino-terminal calponin homolgy (CH) domain followed by a variable linker region and a negatively charged C-terminal domain [Akhmanova and Steinmetz, 2015]. Up to a few hundred EB molecules bind to a region of growing MT ends, where they form comet-like accumulations [Seetapun et al., 2012]. The highest density occurs tens of nanometers away from the outmost MT end [Maurer et al., 2014] which indicates that structure, protofilament number, and the tapering of the distal MT end reduces the binding affinity of EB proteins to MTs [Akhmanova and Steinmetz, 2015]. Studies revealed that EBs preferentially bind to stabilized MTs assembled in the presence of GTP [Maurer et al., 2011] which suggests that EBs recognize the GTP-cap structure. Cryo-electron microscopy analysis of EB-MT interactions showed that the positively charged CH domain of EBs binds to MT protofilaments at the corners of four tubulin dimers [Zhang et al., 2015], which is illustrated in figure 1.9. It was shown that the MT plus-end growth rates measured with various GFP +TIPs are similar to values obtained from fluorescently labeled tubulin [Komarova et al., 2002],

which indicates that the dynamic behavior of MTs is not significantly changed by low expression levels of exogenous +TIPs [Stepanova et al., 2003]. EB3 messenger ribonucleic acids (mRNAs) are enriched in the central nervous system [Nakagawa et al., 2000] making it a good candidate for analyzing MTs in hippocampal neurons. Also, Stepanova et al. showed that EB3 is a good marker of growing MT ends in neuronal cells, and in contrast to EB1, the EB3 signal is stronger in neurons than in glial cells [Stepanova et al., 2003].

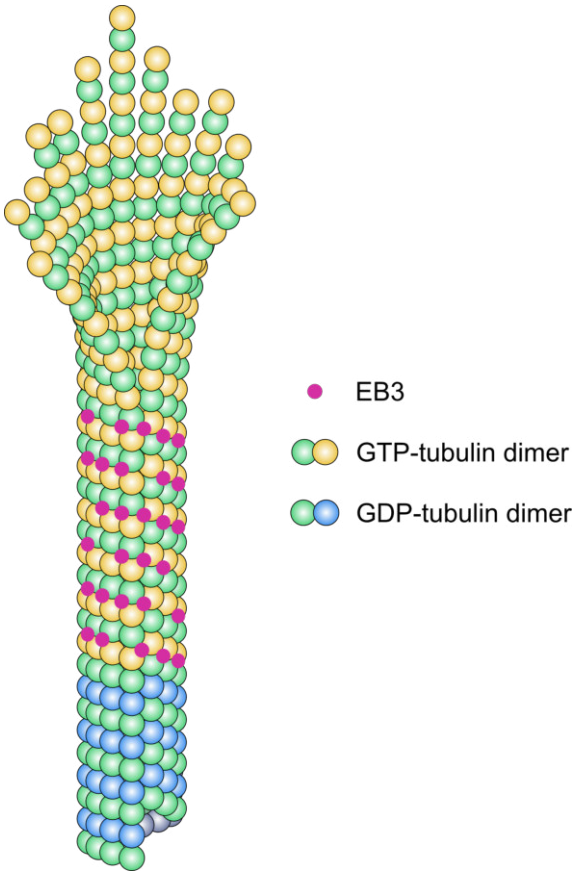

Figure 1.9. – Growing MT plus-end with bound EB3 proteins. Schematic drawing of a growing MT plus-end. GDP-tubulin dimers are shown in green and blue, GTP-tubulin dimers in green and yellow. The positively charged CH domain of EB3 binds between the edges of four GTP-tubulin dimers. The tapered end with curved protofilaments has less affinity for EB3 binding.

1.4.1. Motor proteins

Two superfamilies of motor proteins power directed movement on MTs: kinesin motors that move towards the plus-end and dynein motors that move towards the minus-end. These molecular motor proteins all convert the energy from adenosine triphosphate (ATP) hydrolysis into mechanical force to move along MT tracks [Lee Sweeney and Holzbaur, 2018]. Each case of cargo transport requires three processes, an interaction between motor and cargo, the binding of the motor to a MT track, and the subsequent movement of the motor along the MT [Barlan and Gelfand, 2017]. Each of these processes is subject to a variety of regulatory mechanisms. Many motor proteins use autoregulatory mechanisms (autoinhibition) to turn off their catalytic activity when they are not involved in transporting cargo [Verhey et al., 2011]. This prevents the unnecessary hydrolysis of ATP and the overcrowding of MTs by motors not carrying cargo [Barlan and Gelfand, 2017]. Binding cargo terminates the autoinhibition, leads to MT binding and the stimulation of the transport activity [Verhey and Hammond, 2009]. Although some cargoes can bind directly to motor proteins, many require adaptor molecules to mediate these interactions [Akhmanova and Hammer, 2010]. Because a single class of, for example, kinesins contributes to the motility of many distinct cargoes, the regulation of the specific motor-cargo interactions provide an efficient way to influence the transport of a single cargo type [Kneussel et al., 2014].
In this study the kinesin motor KIF5C-Tomato fusion protein was used to visualize motor movement on MTs. Kinesins are a superfamily with 14 classes (kinesin-1 - 14). KIF5C belongs to the kinesin-1 class [Hirokawa et al., 2010]. They are composed of two identical heavy chains and two associated light chains. Each heavy chain includes an N-terminal motor domain that holds the catalytic activity followed by a neck linker and a coiled-coil stalk that facilitates dimerization [Gennerich and Vale, 2009]. The light chains are associated with the C-terminal cargo binding domain [Valentine and Gilbert, 2007]. The motor domains bind to the MT tracks and processively walk towards the plus-end, hydrolyzing one ATP per step. They bind to the beta-tubulin isotypes of each tubulin dimer, which leads to a step size of 8 nm [Valentine and Gilbert, 2007].

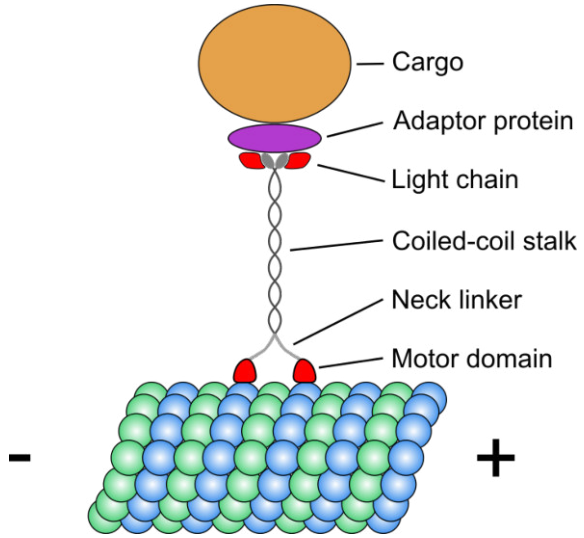

Figure 1.10. – Structure of Kinesin-1. Kinesins from the kinesin-1 class consist of two heavy chains that hold the motor domains, the neck-linkers, and the coiled-coil stalk. The two light chains are involved in cargo binding. For most cargos, the binding is mediated by an adaptor protein. Kinesin walks processively towards the plus-end of the MT, binding to the beta-tubulin isotypes.

2. Methods

2.1. Chemical long-term potentiation induction in acute hippocampal slices

To induce chemical long-term potentiation (cLTP) in acute hippocampal slices the potassium ion channel blocker tetraethylammonium (TEA) was used. The hippocampi of adult C57BL/6 mice were dissected and cut into 400 µm thick slices. They recovered for one hour in artificial cerebral spinal fluid (ACSF). ACSF contained 125 mM NaCl, 25 mM $NaHCO_3$, 25 mM glucose, 2.5 mM KCl, 1.25 mM NaH_2PO_4, 1 mM $MgCl_2$ and 2 mM $CaCl_2$, saturated with 95 % O_2 and 5 % CO_2. Control slices were kept in ACSF, whereas slices for cLTP were transferred into TEA-ACSF and incubated for 10 minutes. TEA-ACSF contained 110 mM NaCl, 25 mM $NaHCO_3$, 15 mM glucose, 2.5 mM KCl, 1.25 mM NaH_2PO_4, 1 mM $MgCl_2$, 2 mM $CaCl_2$ and 25 mM TEA, saturated with 95 % O_2 and 5 % CO_2. Then the slices were transferred back into ACSF for washing. The first group was just dipped, the second washed for 10 minutes and the third washed for 20 minutes. Then the slices were homogenized in lysis buffer (1 % Triton-X-100; protease inhibitor complete 1x, PhosSTOP 1x; in PBS) and centrifuged at 1000 x g at 4°C for 10 minutes. 10 µl of the supernatant were used to determine the total protein concentration with the Pierce BCA Protein Assay Kit (Thermo Scientific, REF: 23227). The rest of the supernatant was mixed with 1x SDS sample buffer (4x stock: 250 mM Tris (pH 6.8); 40 % glycerin; 8 % SDS; 20 % β-mercaptoethanol; 0.008 % bromophenol blue; in water) and boiled at 95°C for 6 minutes. The samples were loaded to a SDS gel or stored at -80°C.

2.2. microRNA knockdown of Tubb3

To achieve a knockdown of *Tubb3* expression, the endogenous miRNA pathway that leads to degradation of complementary mRNA was utilized by transfecting engi-

neered miRNA of the target gene into cells. The BLOCK-iT™ Pol II miR RNAi Expression Vector Kit from Invitrogen (REF 45-1102) was used to produce the engineered miRNA vectors. The Kit provides the vector pcDNA™6.2-GW/EmGFP-miR holding the human CMV promoter and a resistance to spectinomycin. To find complementary sequences with the length of 21 nucleotides that are specific to Tubb3 and not any other gene, especially other tubulin isotypes, the recommended Invitrogen RNAi designer and the Sigma-Aldrich Batch Search for shRNA were used. Additionally, the suggested sequences were confirmed with NCBIs Blast to ensure that they do not have similarities to other tubulin isotypes. The resulting sequences are listed in table 2.1. According to the protocol of the kit, single stranded oligos with the following characteristics were designed:

Top strand from 5' end to 3'end:
1. 5' TGCTG
2. Reverse complement of the 21-nucleotide target sequence
3. Terminal loop GTTTTGGCCACTGACTGAC
4. Nucleotides 1-8 of sense target sequence
5. Nucleotides 11-21 of sense target sequence

Bottom strand:
1. Reverse complement of the top strand without 5' TGCT
2. CCTG added to the 5' end

The control sequence was constructed in our lab team by Franco Lombino and is a scrambled deoxyribonucleic acid (DNA) sequence that is predicted to not target any vertebrate gene. The top and bottom strand oligos are listed in table 2.1. The ordered oligos were resuspended in water to a final concentration of 200 µM before use. The next step was to anneal the single strand oligos to obtain the double strand oligos. Therefore, 5 µl of the top strand, 5 µl of the bottom strand, 2 µl of 10x oligo annealing buffer and 8 µl of DNase/RNase-free water were mixed to a total volume of 20 µl. This was heated for 4 minutes at 95°C and afterwards cooled down at RT for 10 minutes. Then the sample was briefly centrifuged at 6000 x g and afterwards mixed gently. For further dilution 1 µl of 50 µM double strand oligo solution was mixed with 99 µl DNase/RNase free water to get a 500 nM concentration. This was used to verify the annealing of the oligos using agarose gel electrophoresis. Then, 1 µl of the 500 nM oligo solution was mixed with 5 µl of 10x oligo annealing buffer and 44 µl of DNase/RNase-free water to a total volume of 50 µl to get a final concentration of 10 nM. All stock solutions were stored at -20°C. For the ligation of

the double strand oligos into the vector, 4 µl of 5x ligation buffer, 2 µl of linearized pcDNA^{TM}6.2-GW/EmGFP-miR (5 ng/µl), 4 µl of double strand oligos (10 nM), 9 µl of DNase free water and 1 µl of T4 DNA Ligase (1 U/µl) were mixed to a total volume of 20 µl. As negative control the double strand oligo was left out and 13 µl of DNase/RNase free water were used instead. Then the ligation reaction was mixed through pipetting up and down, incubated at RT for 5 minutes and placed on ice. The following transformations and DNA extractions were performed after different protocols described in chapter 2.4 and 2.5.

Table 2.1. – List of designed miRNA sequences and oligos.

miRNA Sequence 1	
21 nucleotide target sequence	CACCAGCTAGTGGAGAACACA
Top strand oligo	TGCTGTGTGTTCTCCACTAGCTGGTGGTTTTGGCCACT GACTGACCACCAGCTTGGAGAACACA
Bottom strand oligo	CCTGTGTGTTCTCCAAGCTGGTGGTCAGTCAGTGGCCA AAACCACCAGCTAGTGGAGAACACAC
miRNA Sequence 2	
21 nucleotide target sequence	CAGGCCCGACAACTTTATCTT
Top strand oligo	TGCTGAAGATAAAGTTGTCGGGCCTGGTTTTGGCCACT GACTGACCAGGCCCGAACTTTATCTT
Bottom strand oligo	CCTGAAGATAAAGTTCGGGCCTGGTCAGTCAGTGGCCA AAACCAGGCCCGACAACTTTATCTTC
miRNA Sequence 3	
21 nucleotide target sequence	CTCCCTTCGATTCCCTGGTCA
Top strand oligo	TGCTGTGACCAGGGAATCGAAGGGAGGTTTTGGCCACT GACTGACCTCCCTTCTTCCCTGGTCA
Bottom strand oligo	CCTGTGACCAGGGAAGAAGGGAGGTCAGTCAGTGGCCA AAACCTCCCTTCGATTCCCTGGTCAC
miRNA Sequence 4	
21 nucleotide target sequence	CGTGCGGAAAGAGTGTGAGAA
Top strand oligo	TGCTGTTCTCACACTCTTTCCGCACGGTTTTGGCCACT GACTGACCGTGCGGAGAGTGTGAGAA
Bottom strand oligo	CCTGTTCTCACACTCTCCGCACGGTCAGTCAGTGGCCA AAACCGTGCGGAAAGAGTGTGAGAAC

Continued on next page

miRNA Sequence 5	
21 nucleotide target sequence	CCTAGATGTCGTGCGGAAAGA
Top strand oligo	TGCTGTCTTTCCGCACGACATCTAGGGTTTTGGCCACT GACTGACCCTAGATGGTGCGGAAAGA
Bottom strand oligo	CCTGTCTTTCCGCACCATCTAGGGTCAGTCAGTGGCCA AAACCCTAGATGTCGTGCGGAAAGAC
miRNA Control	
23 nucleotide target sequence	GGCCTTGCCGGTATATACGACAG
Top strand oligo	TGCTGCTGTCGTATATACCGGCAAGGCCGTTTTGGCCA CTGACTGACGGCCTTGCGTATATACGACAG
Bottom strand oligo	CCTGCTGTCGTATATACGCAAGGCCGTCAGTCAGTGGC CAAAACGGCCTTGCCGGTATATACGACAGC

2.3. Molecular cloning

Molecular cloning was used to produce recombinant DNA that combines genetic material from multiple sources. A DNA fragment was cut out of the source vector with restriction enzymes and incorporated into the target vector. The general mixture to digest source and target vector consisted of: vector DNA; 10x FastDigest Green Buffer (Thermo Scientific); restriction enzymes and water. After incubation at 37°C for 30 minutes the digestion mix was loaded to an 1 % agarose gel to seperate the DNA fragments. They were cut out of the gel and extracted with the NucleoSpin Gel and PCR Clean-up Kit from Macherey-Nagel (REF: 740609.250). The general mixture to ligase the insert DNA into the target vector consisted of: 10x T4 DNA Ligase Buffer (Thermo Scientific), insert DNA; target vector DNA; water and T4 DNA Ligase (5 U/µl) (Thermo Scientific). A molar ratio of vector to insert of 1:3 was used. The ligation mix incubated for 1 hour at RT and the following transformation and DNA extraction are described in chapter 2.4 and 2.5. The exact composition of the cloning mixtures for EB3-Tomato and DNA3-Tubb3 are shown in table 2.2 and 2.3.

Table 2.2. – Cloning mixtures for EB3-Tomato.

Digestion mix source vector	Digestion mix target vector	Ligase mix
5 µg (5 µl) EB3-pEGFP-N1 (Gift from A. Akhmanova [Stepanova et al., 2003])	5 µg (5 µl) ptd-Tomato-N1 vector (kanamycin resistance)	2 µl 10x T4 DNA Ligase Buffer
5 µl 10x FastDigest Green Buffer	5 µl 10x FastDigest Green Buffer	80 ng (4 µl) EB3
2.5 µl EcoR*I*	2.5 µl EcoR*I*	100 ng (3 µl) ptd-Tomato-N1
2.5 µl BamH*I*	2.5 µl BamH*I*	10 µl water
35 µl water	35 µl water	1 µl T4 DNA Ligase
total volume 50 µl	total volume 50 µl	total volume 20 µl

Table 2.3. – Cloning mixtures for DNA3-Tubb3.

Digestion mix source vector	Digestion mix target vector	Ligase mix
4 µg (40 µl) pAcGFP1-C3-Tubb3 (cloned in our lab by P. Breiden)	4 µg (16 µl) pcDNA3 (ampicillin resistance)	2 µl 10x T4 DNA Ligase Buffer
6 µl 10x FastDigest Green Buffer	6 µl 10x FastDigest Green Buffer	70 ng (15 µl) Tubb3
3 µl Hind*III*	3 µl Hind*III*	70 ng (2 µl) pcDNA3
3 µl Xba*I*	3 µl Xba*I*	1 µl T4 DNA Ligase
8 µl water	32 µl water	
total volume 60 µl	total volume 60 µl	total volume 20 µl

2.4. Transformation of plasmid DNA into bacteria

To amplify plasmid DNA and ligated vectors they got transformed into chemical competent *E. coli* Dh5α bacteria, which were stored at -80°C. For the transformation 50 µl of *E. coli* (2.5×10^{-7} CFU/µg) were mixed with 2 µl of ligation reaction or 1 µg of plasmid DNA. This incubated for 20 minutes on ice and was put to 42°C for 45 seconds. Afterwards the mix incubated 2 minutes on ice and then 200 µl of SOC medium (2 % bacto-tryptone; 0.5 % yeast extract; 8.6 mM NaCl; 2.5 mM KCl; 10 mM $MgCl_2$; 10 mM $MgSo_4$; 20 mM glucose) was added. The solution shook at 37°C for

1 hour and was plated on LB agar plates with the respective antibiotic (in my case: kanamycin, ampicillin or spectinomycin). The plates were incubated overnight at 37°C and the next day single clones were picked and proliferated in LB medium with the respective antibiotic. Afterwards the DNA was extracted from the bacteria (see chapter 2.5).

2.5. DNA extraction from bacteria

For DNA extraction the NucleoBond Xtra Midi EF DNA purification Kit from Macherey-Nagel was used (REF 740420.50). The Midiprep was conducted according to the corresponding protocol: Endotoxin-free plasmid DNA purification (April 2017/Rev.07).

2.6. Cell lines

N2A (mouse neuroblastoma) cells and HEK (human embryonic kidney 293) cells were cultured in DMEM supplemented with 10 % fetal bovine serum and 1 % penicillin-streptomycin. Both were split every two to three days using 5 % trypsin.

2.7. Primary hippocampal neurons

To culture primary neurons pregnant C57BL/6 mice were sacrificed by CO_2 suffocation and embryos were removed at embryonic stage 15 to 17. They were decapitated and hippocampi were dissected in ice cold HBSS (Gibco, Thermo Scientific, REF: 14170-088). To dissociate the cells, the hippocampi were incubated in 0.05 % trypsin plus EDTA at 37°C for 5 minutes, the reaction was stopped with prewarmed DMEM plus 10 % fetal bovine serum, and then they were triturated with two fire polished Pasteur pipettes of different diameter in prewarmed HBSS. To estimate cell count a Neubauer chamber was used. For immunofluorescent stainings 80 000 cells were seeded onto a 12 mm glass coverslip (24 well plate) coated with poly-l-lysine in 1 ml Neurobasal Plus Medium (Gibco, Thermo Scientific, REF: A35829-01). For time lapse imaging 50 000 cells were seeded onto the middle of a 25 mm glass coverslip (6 well plate) coated with poly-l-lysine in 3 ml Neurobasal Plus Medium.

2.8. Transfection

2.8.1. N2A cell transfection via ScreenFect

To transfect N2A cells the ScreenFect A-plus Transfection Reagent (InCella, catalog no. S-6000-1) was used according to the provided manual.

2.8.2. Neuron and HEK cell transfection via calcium phosphate

Primary hippocampal neurons and HEK cells were transfected using the calcium phosphate method. For transfecting a 12 mm coverslip (24 well plate) 2 µg DNA were mixed with water to a volume of 18.75 µl and then 6.25 µl $CaCl_2$ (1M) were added. This was mixed dropwise with 25 µl 2x HBS (280 mM NaCl; 10 mM KCl; 1.5 mM Na_2HPO_4; 12 mM dextrose; 50 mM HEPES) and incubated 10 minutes at RT. For a 25 mm coverslip (6 well plate) the double amount was used. In the case of transfecting neurons, 2/3 of the medium was removed and then the transfection mix was added. It incubated for 45 minutes to 2 hours, corresponding to the construct, at 37°C and 5 % CO_2. Afterwards the medium containing the transfection mix was removed and the cells washed 2 times with HEPES buffer (10 mM HEPES; 135 mM NaCl; 5 mM KCl; 2 mM $CaCl_2$; 2 mM $MgCl_2$; 15 mM glucose; pH 7.4), then the remaining conditioned medium was returned to the cells. For HEK cells the transfection mix was added to the medium and incubated over night until the cells were further processed.

2.8.3. Neuron transfection via Lipofectamine

Primary hippocampal neurons were transfected using Lipofectamine. For transfecting a 25 mm coverslip (6 well plate) 2 µg DNA were mixed with 23 µl Optimem (Opti-MEM I(1x), gibco, REF 31985-070) and 2 µl Lipofectamine (Lipofectamine 2000, invitrogen, REF 11668-019) were mixed with 23 µl Optimem. These two solutions were mixed and incubated for 20 minutes. Then 2/3 of the neuron medium was removed and the transfection mix was added. It incubated for 2 hours at 37°C and 5 % CO_2. Afterwards the medium containing the transfection mix was removed and the cells washed 2 times with HEPES buffer (10 mM HEPES; 135 mM NaCl; 5 mM KCl; 2 mM $CaCl_2$; 2 mM $MgCl_2$; 15 mM glucose; pH 7.4), then the remaining conditioned medium was returned to the cells.

2.9. Immunofluorescent staining

Cells were fixed by dipping them into PBS (137 mM NaCl; 2.7 mM KCl; 8.1 mM Na_2HPO_4; 1.4 mM KH_2PO_4) and incubating them in 4 % paraformaldehyde plus 4 % sucrose in water for 12 minutes at RT. After washing two times with PBS they were permeabilized in 0.25 % Triton-X-100 in PBS for 4 minutes. Then they were washed one time with PBS and blocked in 1 % BSA in PBS for 60 minutes at RT. Afterwards the primary antibody was diluted in 1 % BSA in PBS and incubated for 60 minutes at RT. After washing four times with PBS the secondary antibody incubated 45 minutes at RT. Then the cells were washed again four times with PBS and the coverslips were dipped into water before mounting them with Aqua-Poly/Mount (Polysciences, Inc., Cat.-No. 18606-20) onto glass slides. All antibodies are listed in table 2.5 and 2.6.

2.10. Biochemical sample preparation

To harvest cells for biochemical experiments they were washed with ice cold PBS and scraped of the coverslip in lysis buffer (1 % Triton-X-100; protease inhibitor complete 1x, 1 mM PMSF; in PBS). After resuspending the cells through a pipette, they were shaken at 4°C for 30 minutes. Then the mix was vortexed and centrifuged at 1000 x g at 4°C for 10 minutes. 10 µl of the supernatant were used to determine the total protein concentration with the Pierce BCA Protein Assay Kit (Thermo Scientific, REF: 23227). The rest of the supernatant was mixed with 1x SDS sample buffer (4x stock: 250 mM Tris (pH 6.8); 40 % glycerin; 8 % SDS; 20 % β-mercaptoethanol; 0.008 % bromophenol blue; in water) and boiled at 95°C for 6 minutes. The samples were loaded to a SDS gel or stored at -80°C.

2.11. SDS-PAGE

For four resolving gels 15.9 ml water was mixed with 6 ml acrylamide mix (40 %), 7.7 ml Tris-Cl (1.5 M, pH 8.8), 0.3 ml SDS (10 %), 0.018 ml TEMED and 0.3 ml ammonium persulfate (10 %) to a total volume of 30 ml. This was casted into four gel chambers and each was overlayed with 1 ml isopropanol to remove bubbles. After 45 minutes of polymerizing the isopropanol was removed and the stacking gels were casted on top of the resolving gels. They consist of: 8.6 ml water with Orange G, 1.63 ml acrylamide mix (40 %), 1.25 ml Tris-Cl (1 M, pH 6.8), 0.1 ml SDS (10 %), 0.01 ml TEMED and 0.1 ml ammonium persulfate (10 %) which gives a total volume

of 12 ml. After adding a comb, they incubated 45 minutes at RT to polymerize. Then they were put into an electrophoresis chamber with running buffer (10x stock: 250 mM Tris; 2.5 M glycine; 1% SDS in ddH_2O) and the protein Ladder (BlueStar Plus Prestained Protein Marker, Cat. No. MWP 04) and samples were loaded. The gels ran at 90 V for 30 minutes and then at 120 V until the samples passed through the resolving gel. The transfer of the proteins to a PVDF membrane was conducted in a wet transfer chamber with transfer buffer (48 mM Tris; 39 mM glycine; 0.037% SDS; 20% MeOH in ddH_2O) for 3 hours with 80 V at 4°C or overnight at 4°C with 30 V. Afterwards the membrane was washed in TBST (10x stock: 200 mM Tris; 1.5 M NaCl; 20 % Tween 20; pH 7.5) and blocked for 1 hour in milk (5 % (w/v) in TBST). Then the primary antibody diluted in milk (5 % (w/v) in TBST) incubated for 1 hour at RT. After washing three times with TBST the secondary antibody diluted in milk (5 % in TBST) incubated for 45 minutes at RT. Then the membrane was washed again three times with TBST and imaged after adding ECL solution (Immobilon Western HRP Substrat, Millipore, Cat.-No. WBKLS0500). In case a second protein was analyzed on the same membrane, the antibodies were removed by incubating the membrane in stripping buffer (25 mM glycine; 1% SDS; in ddH_2O; pH 2.2) for 1 hour at RT. Afterwards the membrane was washed once in TBST and then processed as described before, starting with the blocking step.

2.12. Imaging

Time lapse imaging was conducted with a spinning disc confocal microscope (Nikon ECLIPSE T*i*) at 37°C and 5 % CO_2 and a CCD camera (Hamamatsu, EM-CCD, Digital Camera C9100). Videos were acquired with a 100 x objective (NA 1.45) and a sample rate of 1 second over 3 minutes with the Visiview software from Visitron Systems. Fixed samples were imaged with a confocal microscope from Olympus (Olympus Fluoview FV1000) and a 60 x objective (NA 1.35). The used software was Fluoview from Olympus.

2.13. ImageJ Macro for video analysis

The analysis of spinning disc confocal videos was conducted with a self-written ImageJ macro. The source code is given in appendix A.1. When applying the macro, first the user must set the scale and the frame rate in seconds. Then, clicking with the point tool on the tracked particle in successive frames leads to saving of the x-

and y-positions and the frame number of each clicked spot. When a track is finished the closing of the Log window induces the calculations of the track length, duration, and velocity. The length is the sum of the distances between the single spots, the duration the number of frames multiplied with the frame rate and the velocity the ratio of length and duration. Then the next track analysis can be started, or the macro is closed.

2.14. Statistics

All statistic tests were conducted with SigmaPlot (version 14.0). First, data were tested for normal distribution with the Shapiro-Wilk test and if they were normally distributed, equal variance was tested with the Brown-Forsythe test. For two samples of normal distributed data a Student's t-test was used for equal variances and a Welch's t-test for unequal variances. For three or more samples of normal distributed data a one way ANOVA was used with the Dunnett's Method for multiple comparisons. If the data were not normally distributed the Mann-Whitney rank sum test was used for two samples and the Kruskal-Wallis one way ANOVA on ranks with Dunn's Method for multiple comparisons for three or more samples.

2.15. DNA-Constructs

Table 2.4. – Constructs used for cloning and transfection.

Short name	Full name	Source
GFP-C3	pAcGFP1-C3	Clontech (Cat.-No. 632482)
GFP-Tubb3	pAcGFP1-C3-Tubb3	Petra Breiden, ZMNH
DNA-GFP-miR	pcDNA^{TM}6.2-GW/EmGFP-miR	Invitrogen (REF 45-1102)
miRNA-S1	pcDNA^{TM}6.2-GW/EmGFP-miR-Sequence1	This study
miRNA-S2	pcDNA^{TM}6.2-GW/EmGFP-miR-Sequence2	This study
miRNA-S3	pcDNA^{TM}6.2-GW/EmGFP-miR-Sequence3	This study
miRNA-S4	pcDNA^{TM}6.2-GW/EmGFP-miR-Sequence4	This study
miRNA-S5	pcDNA^{TM}6.2-GW/EmGFP-miR-Sequence5	This study
miRNA-C	pcDNA^{TM}6.2-GW/EmGFP-miR-Control	Franco Lombino, ZMNH
Tomato-N1	ptd-Tomato-N1	Clontech (Cat.-No. 632532)
EB3-GFP	EB3-pEGFP-N1	Gift from A. Akhmanova
EB3-Tomato	EB3-ptdTomato-N1	This study
KIF5C-Tomato-PEX	KIF5C-tdTomato-PEX26	[Lopes et al., 2020]
NCad-RFP	pCXN2-N-Cadherin-RFP	[Heisler et al., 2014]
DNA3	pcDNA3	Invitrogen
DNA3-Tubb3	pcDNA3-Tubb3	This study
mCherry-Tuba	mCherry-α-tubulin	[Dompierre et al., 2007]

2.16. Antibodies

Table 2.5. – List of primary antibodies.

Target	Species	Company	Cat. No.	Clone	Dilution
Tubb3	mouse	Biolegend	801202	TUJ1	WB 1/5000; IF 1/1000
γ-Adaptin	mouse	BD Bioscience	610386	88	WB 1/5000
panTubb	rabbit	Abcam	ab151318	polyclonal	IF 1/200
panTuba	mouse	Sigma	T9026	DM1A	IF 1/1000
Tubb1	mouse	Novus	NBP2-46245	OTI4A3	IF 1/200
Tubb2	rabbit	Abcam	ab179512	EPR16773	IF 1/200
Tubb4	mouse	Novus	NB-120-11315	ONS1A6	IF 1/100
Tubb5	mouse	Novus	NB-120-11312	SAP.4G5	IF 1/200
Ankyrin-G	rabbit	Santa Cruz	sc-28561	polyclonal	IF 1/500
N-Cadherin	mouse	BD	610921	32/N-Cadherin	IF 1/500
GAPDH	mouse	GeneTex	Gtx28245	6C5	WB 1/4000

Table 2.6. – List of secondary antibodies.

Name	Company	Cat. No.	Dilution
donkey anti-mouse HRP-conjugated	Dianova	715-036-151	WB 1/10000
Cy3 donkey anti-mouse IgG	Dianova	715-165-150	IF 1/500
Cy3 donkey anti-rabbit IgG	Dianova	711-166-152	IF 1/500
Cy5 goat anti-mouse IgG	Dianova	115-175-071	IF 1/500
Cy5 goat anti-rabbit IgG	Dianova	111-175-144	IF 1/500
DAPI	Thermo Fischer	D1306	1/1000

3. Results

3.1. Beta-tubulin isotype mRNA expression

The introduction gave an overview over beta-tubulin isotypes and their functions. To illustrate the expression patterns, figure 3.1 shows mRNA expression levels of mouse beta-tubulin isotypes in different tissues and for brain tissue at two points in development (embryonic day 14.5 and 8 weeks). For this, data from the BioProject PRJNA66167, which is part of the mouse ENCODE (ENCyclopedia Of DNA Elements) project [Yue et al., 2014], were reanalyzed. The shown data for whole brain at 8 weeks of age are averaged values of "cerebellum adult", "cortex adult" and "frontal lobe adult", the other tissue samples also originate from adult mice (8 weeks). In general, the tubulin expression in embryonic brain was much higher than in adult brain, which led to a down-regulation with brain development of almost all isotypes. Only tubulin-beta-4a (Tubb4a) was up-regulated and tubulin-beta-4b (Tubb4b) stayed equal in adult brain tissue. Tubulin-beta-1 (Tubb1) was very little expressed in brain, but highly in lung and spleen. Tubulin-beta-2a (Tubb2a) and tubulin-beta-2b (Tubb2b) were the most expressed isotypes in brain, but they were also abundantly expressed in other tissues. Whereas tubulin-beta-3 (Tubb3), the third highest expressed isotype, was in brain specific to neurons and almost nonexistent in other tissues. Tubb4a was mostly brain specific and Tubb4b was broadly distributed over several tissues, with a peak in testis. Tubulin-beta-5 (Tubb5), which was still highly expressed in embryonic brain, was reduced in adult brain and was also present in other tissues. Tubulin-beta-6 (Tubb6) was little expressed in brain, but highly in other tissues as ovary and bladder. It was shown by our lab that the mRNA levels of developing brain mostly correlate with protein expression [Hausrat et al., 2020]. This illustrated, that in brain the isotypes of interest were Tubb2, Tubb3, Tubb4, and Tubb5, from which only Tubb3 and Tubb4a were brain specific. Tubb3 was also highly expressed in the developing brain, often used as a neuronal marker, and associated with MT diseases and cancer. For these reasons, this thesis focused on Tubb3.

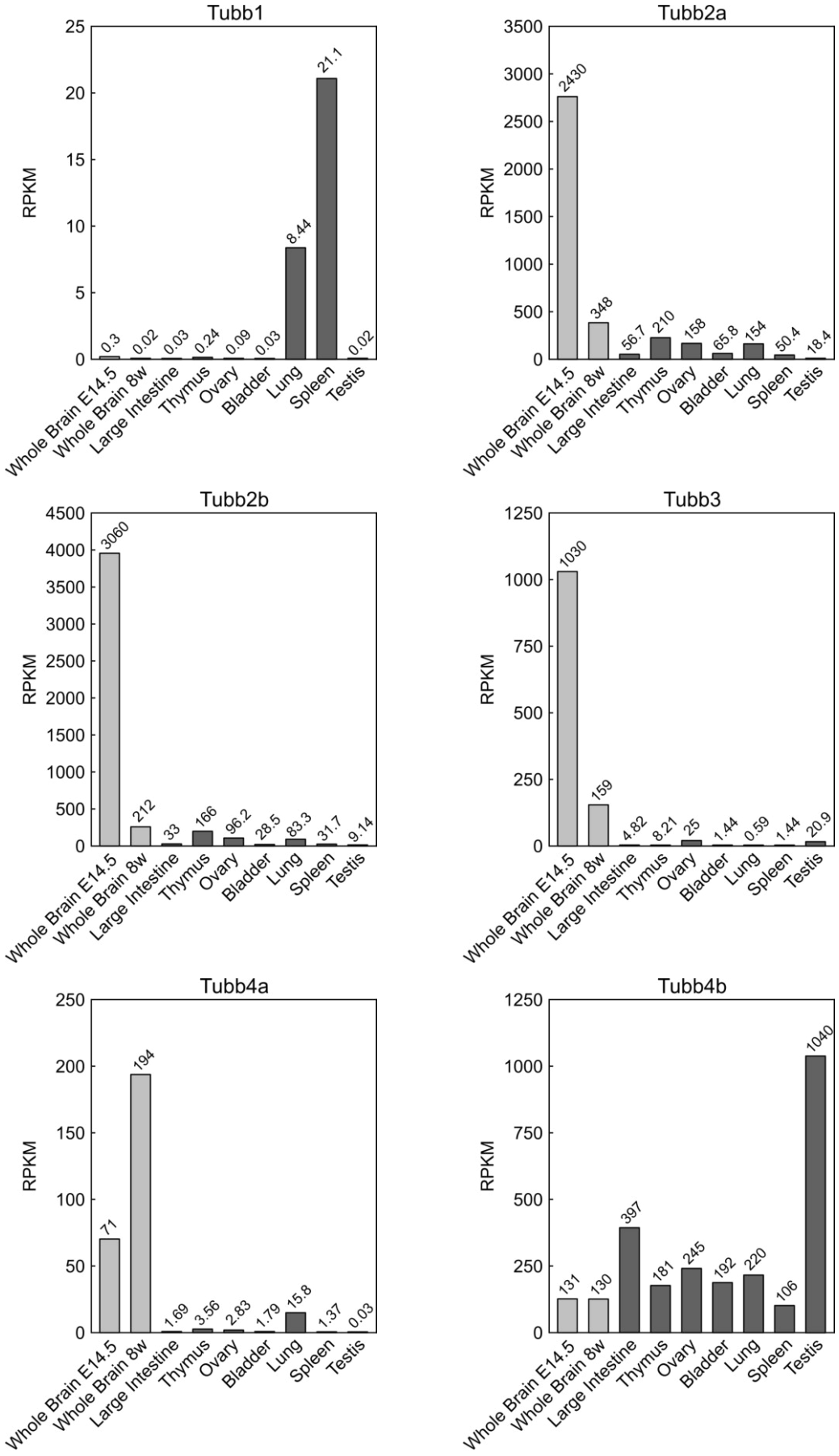

Figure 3.1. – *Continued on next page*

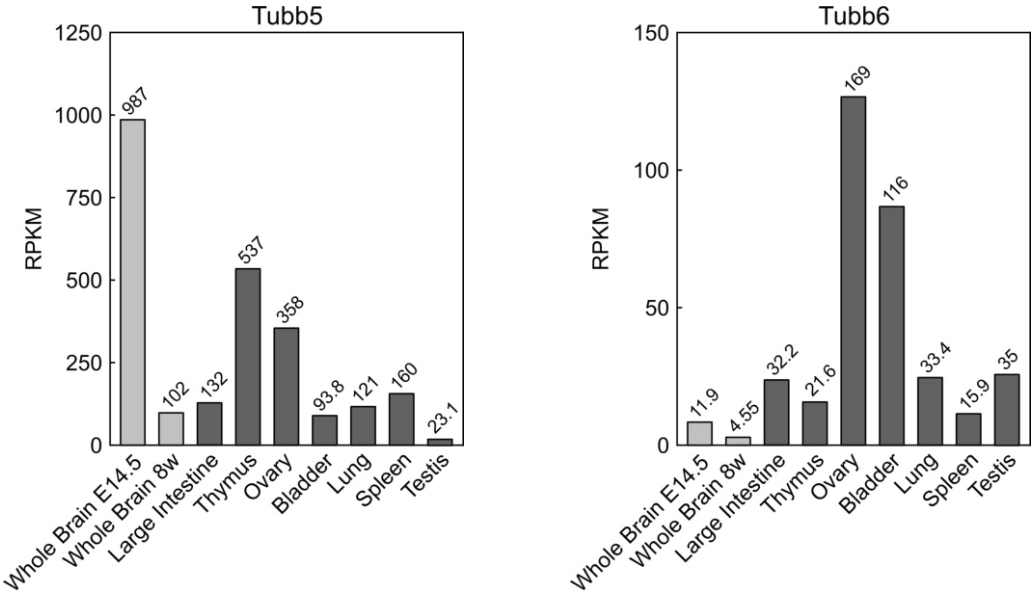

Figure 3.1. – mRNA expression levels of beta-tubulin isotypes in mouse tissues. mRNA data of Tubb1, Tubb2a, Tubb2b, Tubb3, Tubb4a, Tubb4b, Tubb5 and Tubb6 levels in mouse tissues. The columns of whole brain on embryonic day 14.5 (E14.5) and whole brain 8 weeks (8w) are marked in light gray, other tissues are depicted in dark gray and originate from adult (8 weeks) mice. The RPKM value of each tissue is written above the column. Data originate from the BioProject PRJNA66167, which is part of the mouse ENCODE (ENCyclopedia Of DNA Elements) project [Yue et al., 2014]. The shown data for whole brain 8 weeks are averaged values of "cerebellum adult", "cortex adult" and "frontal lobe adult". RPKM: reads per kilobase million.

3.2. Chemical long-term potentiation induction in acute hippocampal slices

The correlation of tubulin isotype composition in microtubules (MTs) and synaptic plasticity is mostly unknown. To investigate this connection, acute hippocampal slices were stimulated by chemical long-term potentiation (cLTP) induction via tetraethylammonium (TEA) (method in chapter 2.1) and Tubb3 protein levels were analyzed. Acute slices were incubated in artificial cerebrospinal fluid (ACSF) containing TEA for 10 minutes and then washed in ACSF without TEA. One group was just dipped (10 minutes), while the second and the third was washed for 10 minutes (20 minutes) and 20 minutes (30 minutes), respectively. Control slices were incubated in ACSF only. Slice lysates were analyzed by SDS-Page analysis, a representative western blot and quantification are shown in figure 3.2. Tubb3 signal intensities were normalized to the loading control γ-Adaptin and the control value was set to one. Acute slices showed a significant increase in Tubb3 protein signal

intensity 20 and 30 minutes after LTP induction, compared to the control sample. The γ-Adaptin signal intensity of stimulated slices itself did not significantly change compared to the control. This experiment indicated that tubulin isotype expression is connected to synaptic stimulation. Literature points to an association of synaptic plasticity to MT dynamics [Hoogenraad and Akhmanova, 2010, Dent et al., 2011], which led to the detailed investigation of Tubb3 expression levels and their effect on MT dynamics.

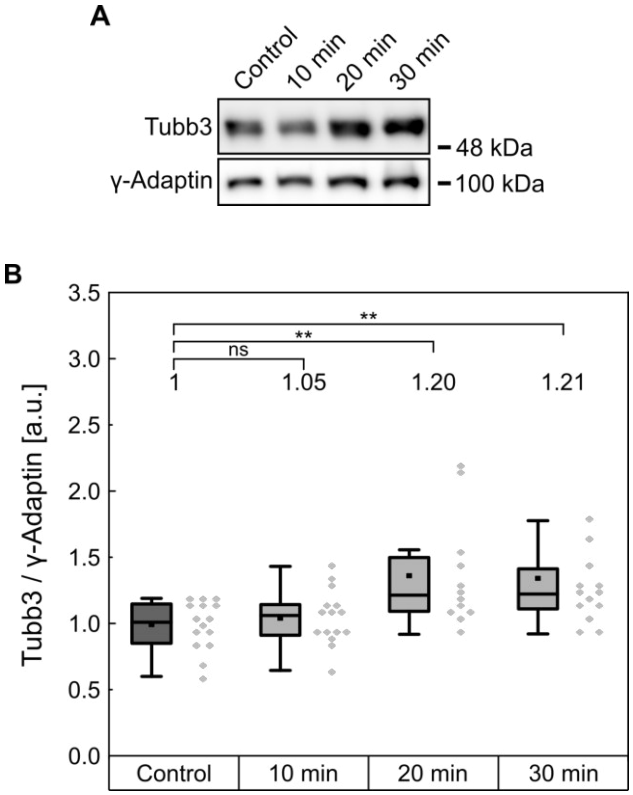

Figure 3.2. – Tubb3 levels after chemical LTP induction in acute hippocampal slices. (A): Representative western blot of Tubb3 protein levels derived from lysed acute hippocampal slices after treatment with TEA to induce chemical LTP. Control slices were treated with ACSF only. Sample slices were treated with TEA for 10 minutes and then washed in ACSF for 0 (10 minutes), 10 (20 minutes) or 20 (30 minutes) minutes. γ-Adaptin was used as loading control.

Continued on next page

Figure 3.2. – Tubb3 levels after chemical LTP induction in acute hippocampal slices. (B): Quantification of Tubb3 signal intensity normalized by γ-Adaptin based on three independent experiments. 10 minutes after treatment with TEA slices show no significant difference in Tubb3 signal intensity, 1.05 a.u. *(p = 1)*, compared to control slices (set to 1). 20 and 30 minutes after cLTP induction slices show a significant increase in Tubb3 signal intensity to 1.20 a.u. *(p = 0.009)* and 1.21 a.u. *(p = 0.006)*, respectively, compared to the control. Depicted are median values with 25th and 75th percentile. Whiskers indicate the range within 1.5 interquartile range (IQR). Black squares show the mean value. Each data point represents one slice (n = 16). For graphical representation of the distribution data are binned with bin size 0.15 [a.u.]. Statistics: Kruskal-Wallis one way ANOVA on ranks, followed by Student's t-test.

3.3. Knockdown of Tubb3 via engineered microRNA

3.3.1. Screening of microRNA sequences in Neuro-2A cells

To determine the effect of reduced *Tubb3* expression levels on MT dynamics, a knockdown approach via engineered microRNAs (miRNAs) was established. Engineered miRNAs inhibit the translation of corresponding messenger RNA (mRNA). Five designed miRNA sequences were tested by transfection into Neuro-2A (N2A) cells and SDS-PAGE analysis (methods see chapter 2.8, 2.6 and 2.11). Cells were lysed 24 hours after transfection. A representative western blot and quantification are shown in figure 3.3. Green fluorescent protein (GFP)-Tubb3 was co-transfected with each of the five miRNA sequences (miRNA-S1 - S5) or the control miRNA (miRNA-C), which is a scrambled sequence that should not bind to any mRNA. The exogenous Tubb3 was a fusion protein with GFP, so it was distinguishable from the endogenous Tubb3 signal based on the higher molecular weight. γ-Adaptin was used as loading control. In the quantification, Tubb3 intensity values were normalized to the γ-Adaptin signal intensity. For exogenous Tubb3, sequences one, two, four and five led to a significant reduction (33 %, 17 %, 27 % and 42 %, respectively) of Tubb3 levels compared to the control, which was set to one. Therefore, sequences one, two and four were further tested in neurons (Figure 3.5). The endogenous Tubb3 levels showed the same tendencies but were not significantly altered. The protein half-life of endogenously expressed Tubb3 might contribute to the different observations. To further investigate this, in following experiments the knockdown effect was investigated over five consecutive days.

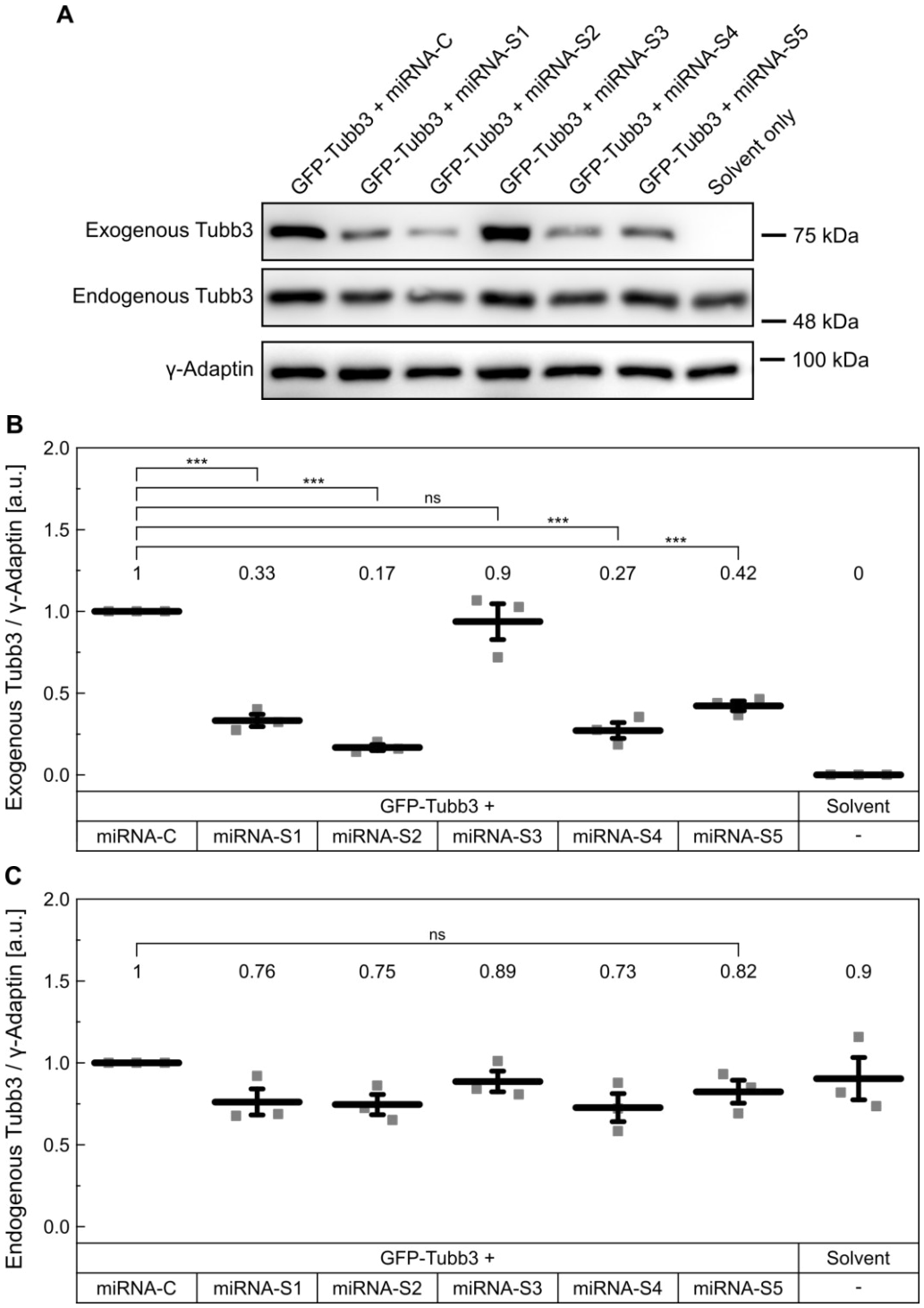

Figure 3.3. – Downregulation of Tubb3 protein expression through miRNA induced knockdown in N2A cells. (A): Representative western blots of exogenous Tubb3-GFP (at 75 kDa) and endogenous Tubb3 protein levels (at 50 kDa) derived from transfected N2A cells. γ-Adaptin was used as loading control. First lane: co-transfection of GFP-Tubb3 and control miRNA (miRNA-C). Lanes two to six: co-transfections of GFP-Tubb3 and one of the five miRNA knockdown sequences (miRNA-S1 - S5), respectively. Lane seven: transfection solvent without DNA.

Continued on next page

Figure 3.3. – Downregulation of Tubb3 protein expression through miRNA induced knockdown in N2A cells. (B): Quantification of exogenous Tubb3 signal intensities based on three independent experiments. After transfection with miRNA-S1, miRNA-S2, miRNA-S4 and miRNA-S5, Tubb3 levels are significantly decreased to 0.33 ± 0.04 a.u. *($p < 0.001$)*, 0.17 ± 0.02 a.u. *($p < 0.001$)*, 0.27 ± 0.05 a.u. *($p < 0.001$)* and 0.42 ± 0.03 a.u. *($p < 0.001$)*, respectively, compared to miRNA-C (set to 1). miRNA-S3 shows no significant difference, 0.9 ± 0.1 a.u. *($p = 0.87$)*, compared to miRNA-C. Statistics: one way ANOVA, followed by Dunnett's Method for multiple comparisons versus control group. Depicted: mean ± SEM. Each data point illustrates one western blot experiment (n = 3). **(C):** Quantification of endogenous Tubb3 signal intensities based on three independent experiments. Transfections with miRNA knockdown sequences 1 - 5 (miRNA-S1 - S5) show no significant decrease in Tubb3 signal intensities, 0.76 ± 0.08 a.u., 0.75 ± 0.06 a.u., 0.89 ± 0.06 a.u., 0.73 ± 0.09 a.u. and 0.82 ± 0.07 a.u., respectively, compared to miRNA-C (set to 1). Statistics: one way ANOVA *($p = 0.21$)*. Depicted: mean ± SEM. Each data point illustrates one western blot experiment (n = 3).

3.3.2. Validation of Tubb3 knockdown in secondary dendrites

To analyze the effects of the efficient miRNA sequences in neurons, hippocampal cultures were transfected at day in vitro (DIV) 9 using the calcium phosphate method. According to literature [Caron et al., 1985, Dutton and Barondes, 1969] the half-life of tubulin lies between two and four days, so the cells were fixed three days after transfection at DIV 12. Afterwards they were stained by immunocytochemistry and imaged with a confocal microscope. Figure 3.4 exemplifies the most common composition of applied antibodies and confocal imaging lasers. GFP was co-expressed with the miRNA in transfected cells and served as marker for transfected neurons. Tubb3 was immuno-stained via TUJ1 in combination with Cy3 and DNA was visualized with a DAPI staining. Detailed information about antibodies are listed in chapter 2.16. Figure 3.5 shows the results of miRNA regulated Tubb3 knockdown in neuronal dendrites. Cells were transfected with the control miRNA or miRNA sequences one, two and four. Figure 3.5 B shows enlargements of the dendritic segments marked by the pink boxes in A. The yellow boxes mark a region were the Tubb3 signal originates from a transfected cell and does not overlap with signals from other cells. To acquire comparable intensity values, control and knockdown images of the Tubb3 channel were imaged with the same microscope settings. The quantification showed a significant decrease in Tubb3 signal intensity after transfection with miRNA-S2 (73 %) and miRNA-S4 (67 %) compared to the control, which was set to one. Cells transfected with miRNA-S1 showed no significant difference compared to the control and, thus, this miRNA sequence was not further used.

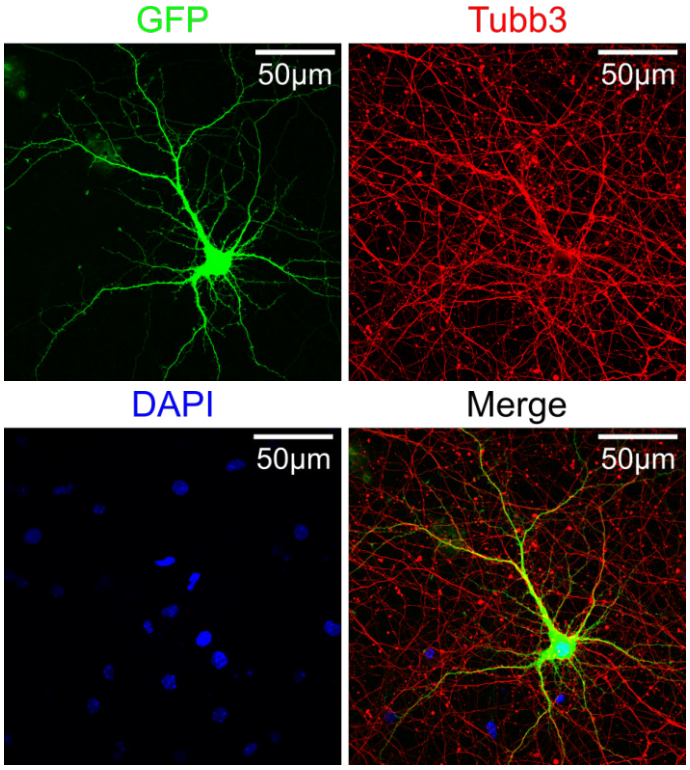

Figure 3.4. – Illustration of confocal imaging. Dissociated hippocampal neurons were transfected at DIV 9 and fixed at DIV 12. The miRNA vector contains a GFP sequence, which is additionally expressed. Via the GFP signal (green) transfected cells can be distinguished from un-transfected cells. The fixed culture was stained via immunocytochemistry. Here, the primary antibody TUJ1 against Tubb3 was combined with a Cy3 secondary antibody (red). Simultaneously with the secondary antibody incubation a DAPI staining was performed (blue) to visualize the nucleus. Antibodies are listed in chapter 2.16. Samples were imaged with an Olympus confocal microscope using UV (405 nm), blue (488 nm) and green (559 nm) lasers to detect DAPI, GFP, and Cy3, respectively. Scale bar, 50 µm.

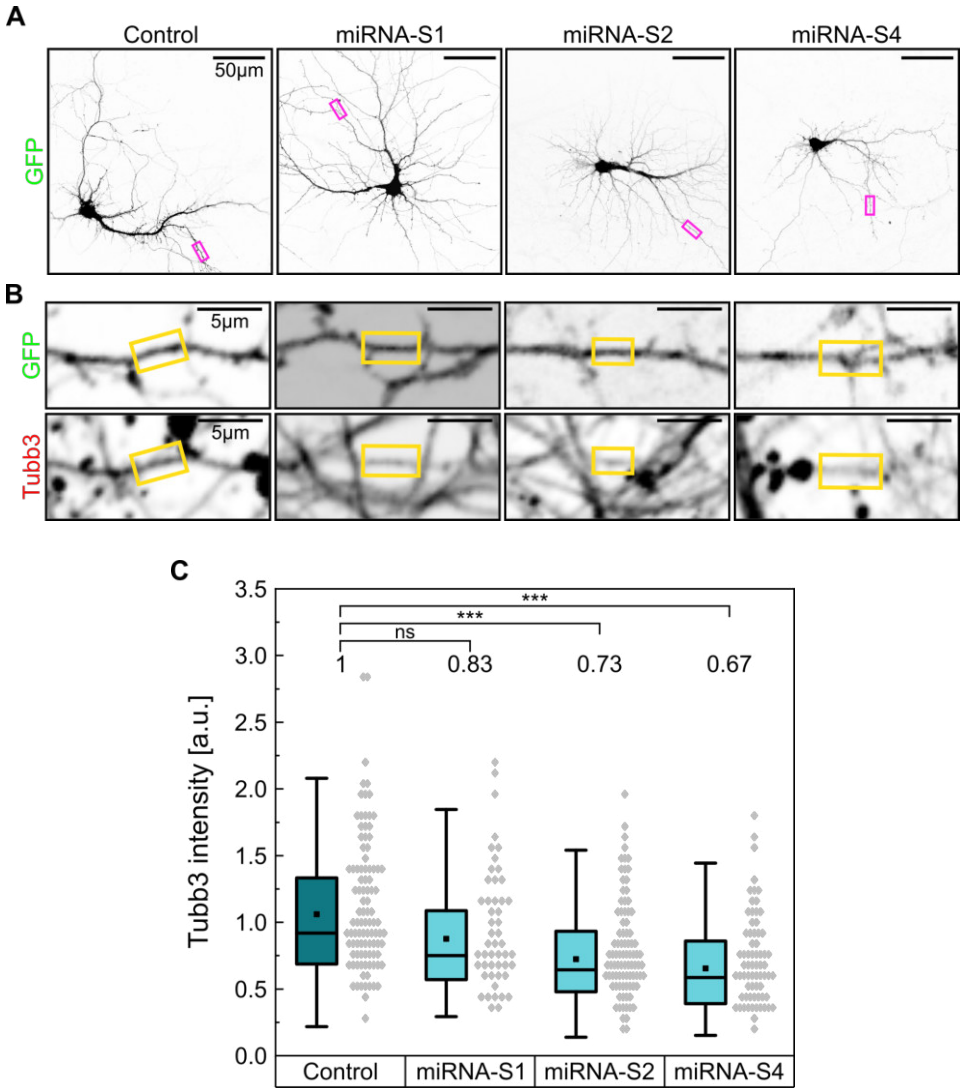

Figure 3.5. – Validation of Tubb3 knockdown in secondary dendrites. **(A):** Representative images of hippocampal neurons transfected with miRNA-C, miRNA-S1, miRNA-S2 or miRNA-S4. Scale bar, 50 µm. **(B):** Enlargements of dendritic segments in the pink boxes in (A). Tubb3 intensities were measured inside the yellow boxes of the Tubb3 image, where they do not overlap with Tubb3 signal of other cells. The GFP signal in the yellow box indicates that the Tubb3 signal originated from a transfected cell. Scale bar, 5 µm. **(C):** Quantification of Tubb3 intensity measurements in secondary dendrites based on three independent experiments. Cells transfected with miRNA-S2 and miRNA-S4 have significantly decreased Tubb3 intensity values, 0.73 a.u. *($p < 0.001$)* and 0.67 a.u. *($p < 0.001$)*, respectively, compared to cells transfected with the control miRNA (set to 1). miRNA-S1 shows no significant difference, 0.83 a.u. *($p = 0.074$)*, compared to the control. Depicted are median values with 25th and 75th percentile. Whiskers indicate the range within 1.5 IQR. Black squares show the mean value. Each data point represents one cell; control (n = 99), miRNA-S1 (n = 51), miRNA-S2 (n = 91), miRNA-S4 (n = 70). For graphical representation of the distribution, data are binned with bin size 0.08 [a.u.]. Statistics: Kruskal-Wallis one way ANOVA on ranks, followed by Dunn's Method for multiple comparisons against control group.

To validate tubulins assumed half-life value of three days a timeline experiment was conducted. Since miRNA-S4 showed the strongest downregulating effect on Tubb3 signal intensity, it was used to induce the knockdown. After the transfection of hippocampal neurons with the miRNA constructs, cells were fixed every 24 hours over five days. They were stained for Tubb3 as described before. Representative confocal images are shown in figure 3.6, again transfected cells were identified by GFP expression. Panel B1 and B2 show the enlargements of dendritic segments marked by the pink boxes in A1 and A2, respectively. The Tubb3 panel illustrates the decrease of Tubb3 signal intensity in dendrites over time. The quantification showed that the knockdown needed three days to develop a significant decrease (to 73 %) in Tubb3 intensity and was stable over day four and five (74 % and 75 %). The values of each day were normalized to the respective control, which was set to one.

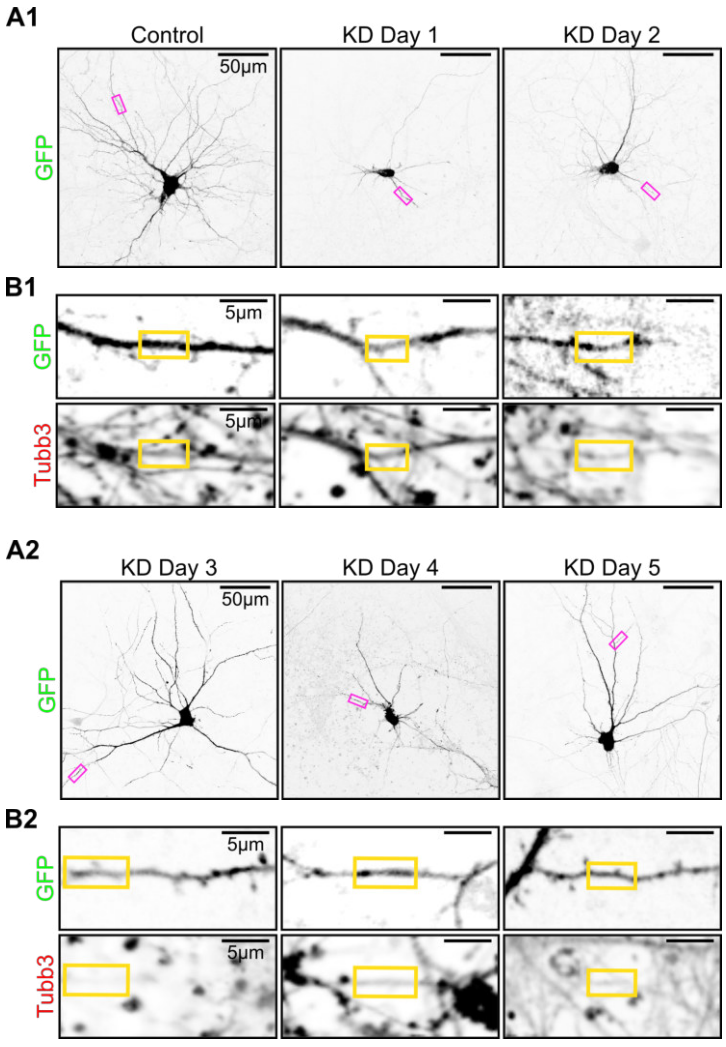

Figure 3.6. – *Continued on next page*

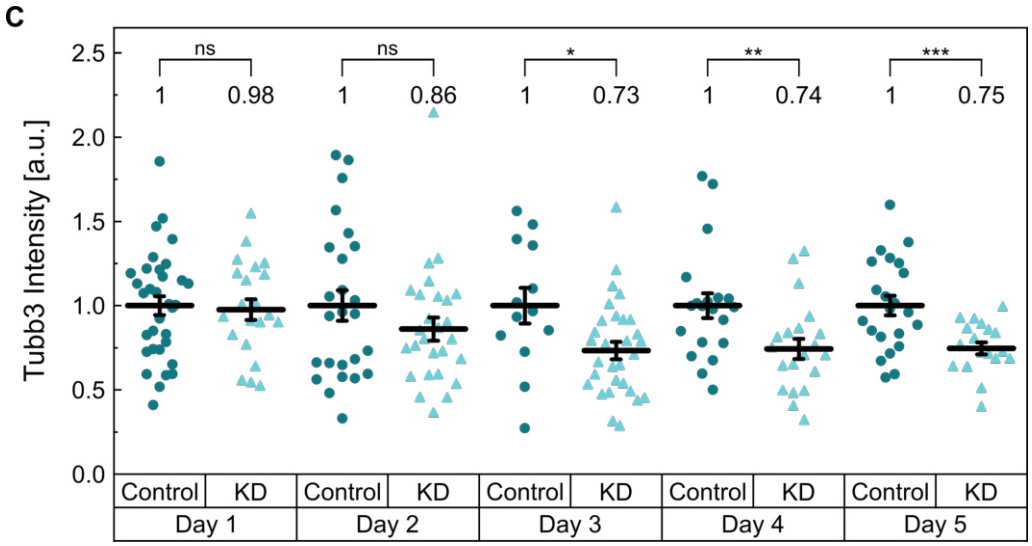

Figure 3.6. – Timeline experiment of Tubb3 knockdown in secondary dendrites. (A1 - 2): Representative images of hippocampal neurons transfected with control or knockdown miRNA at DIV 9. Cells were fixed and stained every 24 hours over five days. Scale bar, 50 µm. **(B1 - 2):** Enlargements of dendritic segments marked by the pink boxes in (A1 - 2). Tubb3 intensities were measured inside the yellow boxes of the Tubb3 image, where they do not overlap with Tubb3 signal of other cells. The GFP signal in the yellow box indicates that the Tubb3 signal originated from a transfected cell. Scale bar, 5 µm. **(C):** Quantification of Tubb3 intensity measurements in secondary dendrites. Values are normalized to the respective control. Cells fixed on day 1 and 2 show no significant difference in Tubb3 intensity, 0.98 ± 0.06 a.u. *($p = 0.782$)* and 0.86 ± 0.07 a.u. *($p = 0.379$)*, respectively, compared to their controls (set to 1). Cells that were fixed on day 3, 4 and 5 show a significant decrease in Tubb3 intensity values, 0.73 ± 0.05 a.u. *($p = 0.015$)*, 0.74 ± 0.06 a.u. *($p = 0.009$)* and 0.75 ± 0.04 a.u. *($p < 0.001$)*, respectively, compared to their respective controls (set to 1). Depicted: mean ± SEM. Statistics: day 1 and 3: Student's t-test; day 2 and 4: Mann-Whitney rank sum test; day 5: Welch's t-test. Each data point represents one cell; day 1: control (n = 33), KD (n = 21), day 2: control (n = 25), KD (n = 27), day 3: control (n = 13), KD (n = 30), day 4: control (n = 20), KD (n = 20), day 5: control (n = 22), KD (n = 18). The experiment was conducted once. KD: knockdown.

3.3.3. Validation of Tubb3 Knockdown in the cell soma

In this study the effect of Tubb3 downregulation on MT dynamics and MT dependent transport processes was analyzed. Since Tubb3 occurrence in dendrites itself might already be influenced by transport processes the Tubb3 knockdown validation was repeated with intensity measurements inside the soma of neurons, not overlapping with the nucleus. Again, hippocampal neurons were transfected with control and knockdown miRNA, representative images and quantification are shown in fig-

ure 3.7. Here, panel B shows enlargements of the cell somata marked by pink boxes in A. Tubb3 signal intensity was measured in DAPI negative areas indicated by the yellow boxes. miRNA-S2 and miRNA-S4 were tested regarding their knockdown effect, and it was confirmed, that miRNA-S4 showed the strongest reduction in Tubb3 signal intensity to 45% compared to 56% for miRNA-S2. Therefore, miRNA-S4 was used in all further experiments to induce the Tubb3 knockdown. Additionally, pan-beta-tubulin (panTubb) and pan-alpha-tubulin (panTuba) intensity levels were measured (Figure 3.8) (antibodies listed in 2.16). Both did not show a significant change in signal intensity, indicating that the loss of Tubb3 was compensated by other beta-tubulin isotypes.

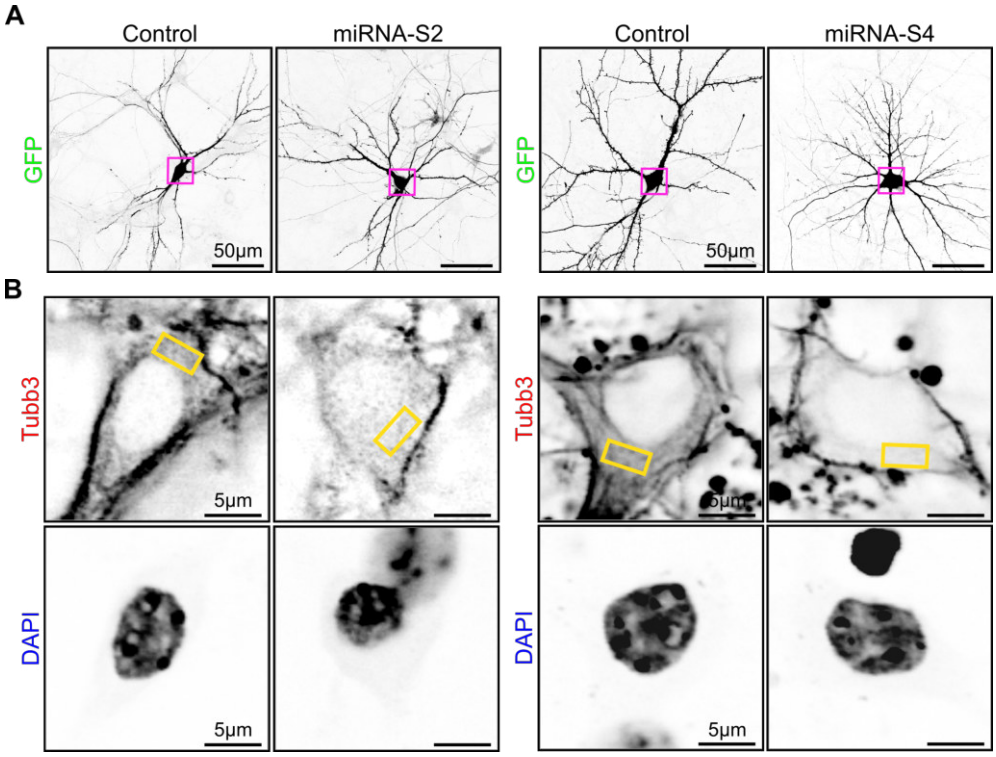

Figure 3.7. – *Continued on next page*

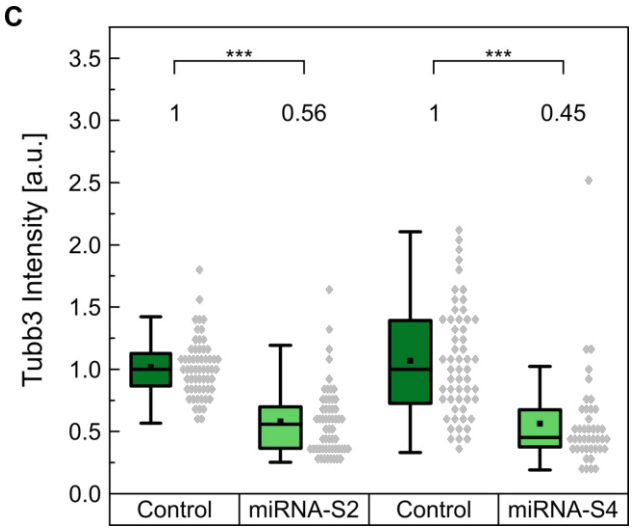

Figure 3.7. – Validation of Tubb3 knockdown in the soma. (A): Representative images of hippocampal neurons transfected with control miRNA, miRNA-S2 or miRNA-S4 at DIV 9 and fixed at DIV 12. Scale bar, 50 µm. **(B):** Enlargements of cell somata marked by the pink boxes in (A). Tubb3 intensities were measured inside the soma, indicated by the yellow boxes. To ensure that the analyzed region does not overlap with the cell nucleus, a DNA staining was used (DAPI). Scale bar, 5 µm. **(C):** Quantification of the intensity measurements in the soma based on three independent experiments. Cells transfected with miRNA-S2 and miRNA-S4 both show a significant decrease in Tubb3 intensity values, 0.56 a.u. *($p < 0.001$)* and 0.45 a.u. *($p < 0.001$)*, respectively, compared to their respective control (set to 1). Depicted are median values with 25th and 75th percentile. Whiskers indicate the range within 1.5 IQR. Black squares show the mean value. Each data point represents one cell; control (n = 59), miRNA-S2 (n = 57), control (n = 56), miRNA-S4 (n = 42). For graphical representation of the distribution, data are binned with bin size 0.08 [a.u.]. Statistics: Mann-Whitney rank sum test.

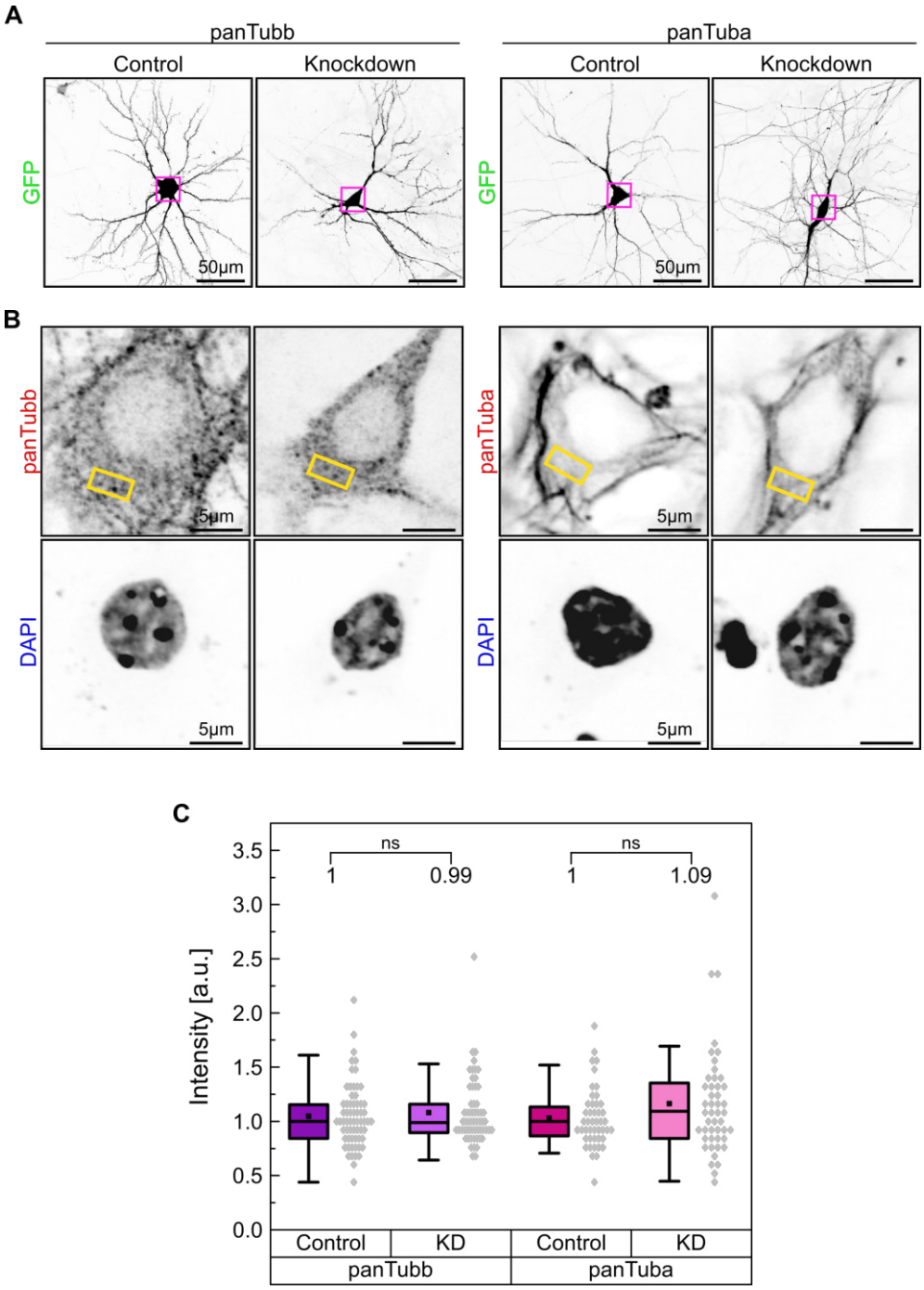

Figure 3.8. – General tubulin levels are not altered upon Tubb3 reduction. **(A):** Representative images of hippocampal neurons transfected with control miRNA or knockdown miRNA at DIV 9 and fixed at DIV 12. Scale bar, 50 µm. **(B):** Enlargements of cell somata marked by the pink boxes in (A). In the left panel panTubb and in the right panel panTuba intensities were measured inside the soma, indicated by the yellow boxes. To ensure that the analyzed region does not overlap with the cell nucleus, a DNA staining was used (DAPI). Scale bar, 5 µm.

Continued on next page

Figure 3.8. – General tubulin levels are not altered upon Tubb3 reduction. (C): Quantification of the intensity measurements in the soma based on three independent experiments. The intensity levels of panTubb and panTuba show no significant decrease after transfection with Tubb3 knockdown miRNA, 0.99 a.u. *(p = 0.629)* and 1.09 a.u. *(p = 0.274)*, respectively, compared to their respective control (set to 1). Depicted are median values with 25th and 75th percentile. Whiskers indicate the range within 1.5 IQR. Black squares show the mean value. Each data point represents one cell; panTubb: control (n = 64), KD (n = 60), panTuba: control (n = 46), KD (n = 47). For graphical representation of the distribution, data are binned with bin size 0.08 [a.u.]. Statistics: Mann-Whitney rank sum test. KD: Knockdown.

To review the results of the tubulin half-life, the timeline experiment data for the Tubb3 intensity values were reanalyzed inside the soma. As a reminder, cells were transfected and then fixed every 24 hours over five days. Representative images and results are shown in figure 3.9. Panel B1 and B2, which show the enlargements of the cell somata marked in A1 and A2, already indicate that the Tubb3 signal intensity in DAPI negative regions decreased over time (yellow boxes). The quantification showed a significant decrease in Tubb3 intensity for cells that were transfected with knockdown miRNA already on day two (79 %). On day three, four and five the Tubb3 signal intensity decreased further to 56 %, 54 % and 43 %, respectively. Since the knockdown effect on day three was much stronger than on day two and the timeline analysis in dendrites showed a significant decrease starting from day three, all following experiments were conducted with a three day incubation period between transfection and further treatment, unless stated otherwise.

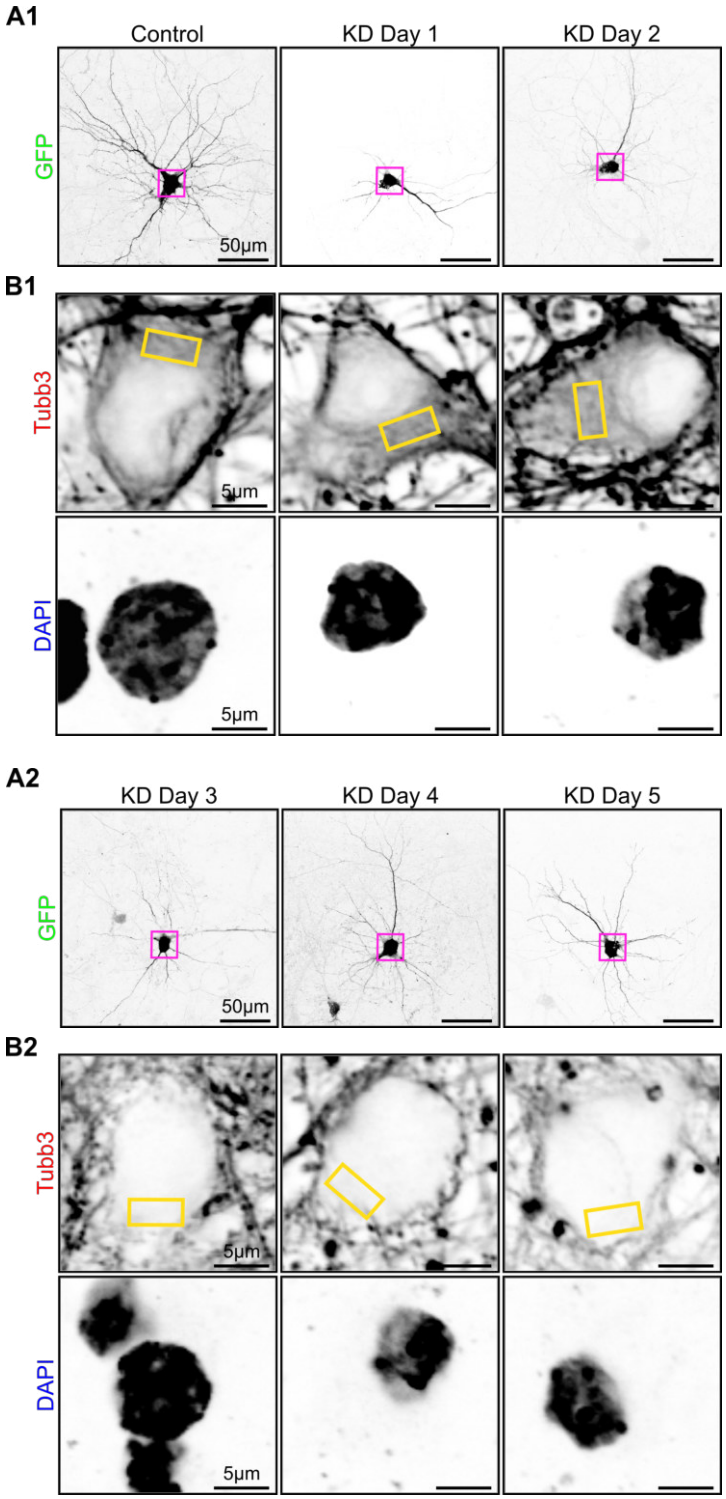

Figure 3.9. – *Continued on next page*

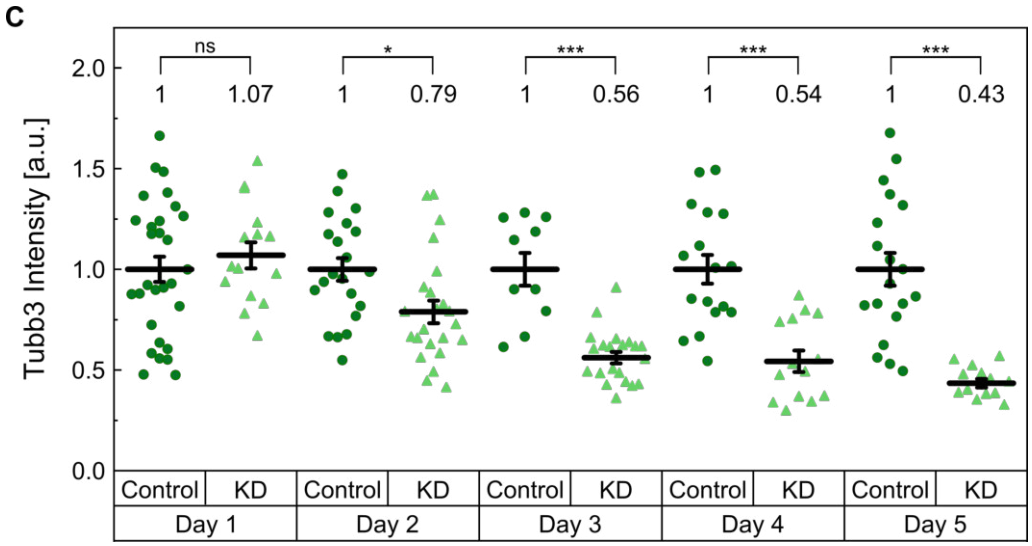

Figure 3.9. – Timeline experiment of Tubb3 knockdown in the soma. (A1 - 2): Representative images of hippocampal neurons transfected with control or knockdown miRNA at DIV 9. Cells were fixed and stained every 24 hours over 5 days (Day 1 - 5). Scale bar, 50 µm. **(B1 - 2):** Enlargements of the cell somata in the pink boxes in (A1 - 2). Tubb3 signal intensities were analyzed in DAPI negative regions as indicated by the yellow boxes. Scale bar, 5 µm. **(C):** Results of Tubb3 intensity measurements in the soma. Values were normalized to the respective control. Cells fixed on day 1 show no significant difference in Tubb3 intensity, 1.07 ± 0.06 a.u. *($p = 0.485$)* compared to the control (set to 1). Cells that were fixed on day 2, 3, 4 and 5 show a significant decrease in Tubb3 intensity, 0.79 ± 0.06 a.u. *($p = 0.012$)*, 0.56 ± 0.03 a.u. *($p < 0.001$)*, 0.54 ± 0.05 a.u. *($p < 0.001$)* and 0.43 ± 0.02 a.u. *($p < 0.001$)*, respectively, compared to their respective control (set to 1). Depicted: mean ± SEM. Statistics: day 1, 2 and 4: Student's t-test; day 3 and 5: Welch's t-test. Each data point represents one cell; day 1: control (n = 29), KD (n = 15), day 2: control (n = 21), KD (n = 23), day 3: control (n = 10), KD (n = 21), day 4: control (n = 17), KD (n = 14), day 5: control (n = 19), KD (n = 13). The experiment was conducted once. KD: knockdown.

3.4. Expression analysis of several beta-tubulin isotypes after Tubb3 downregulation

As shown before, it was likely, that the knockdown of Tubb3 was compensated by another beta-tubulin isotype. To investigate the effect of decreased Tubb3 levels on the expression of other isotypes, hippocampal cells were transfected with control and knockdown miRNA using Lipofectamine. After three days cells were fixed and stained with antibodies against Tubb1, Tubb2, Tubb3, Tubb4, Tubb5 and panTubb (details in 2.16). Representative images and results are shown in figure 3.10. Panel B1, B2 and B3 show the enlargements of the somata marked by the pink boxes in

A1, A2 and A3, respectively. The signal intensity was measured inside the soma in DAPI negative regions marked by the yellow boxes. The quantification confirmed the downregulation of Tubb3 signal intensity (28 %) compared to the control. Of the other tubulin isotypes, Tubb4 showed a significant increase in signal intensity (133 %) when transfected with Tubb3 knockdown miRNA compared to the control. All other analyzed beta-tubulin isotypes showed no significant difference in signal intensity compared to the control. This result indicated that observed phenotypes in following experiments not only originate from reduced Tubb3 levels, but also from increased Tubb4 expression.

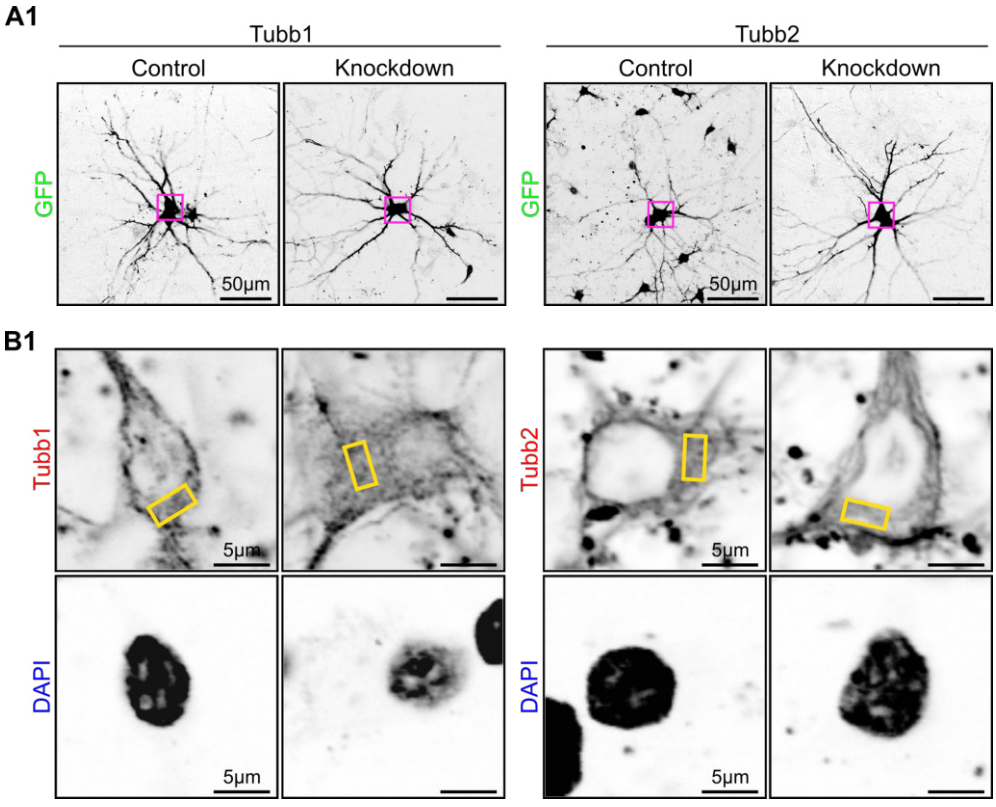

Figure 3.10. – *Continued on next page*

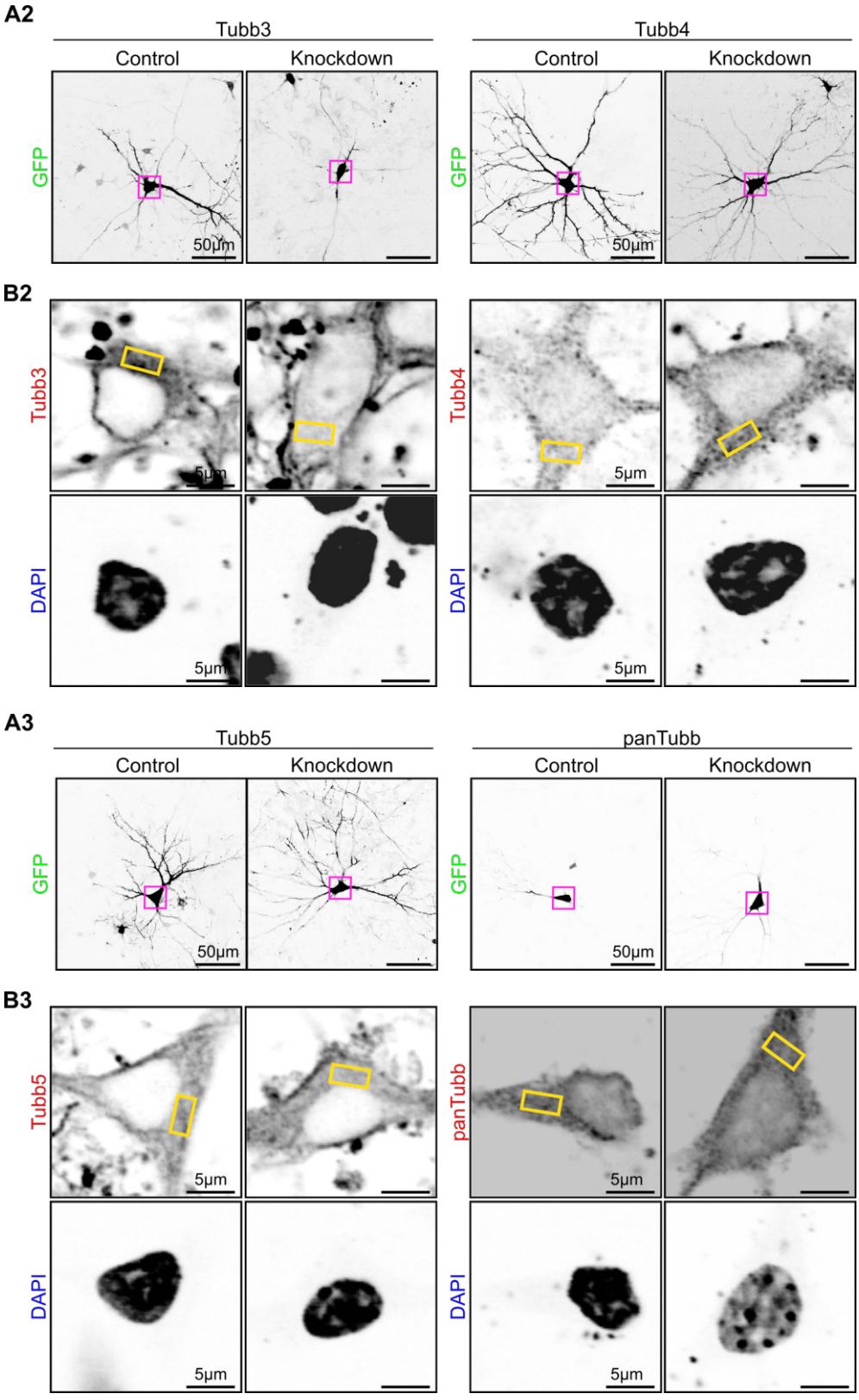

Figure 3.10. – *Continued on next page*

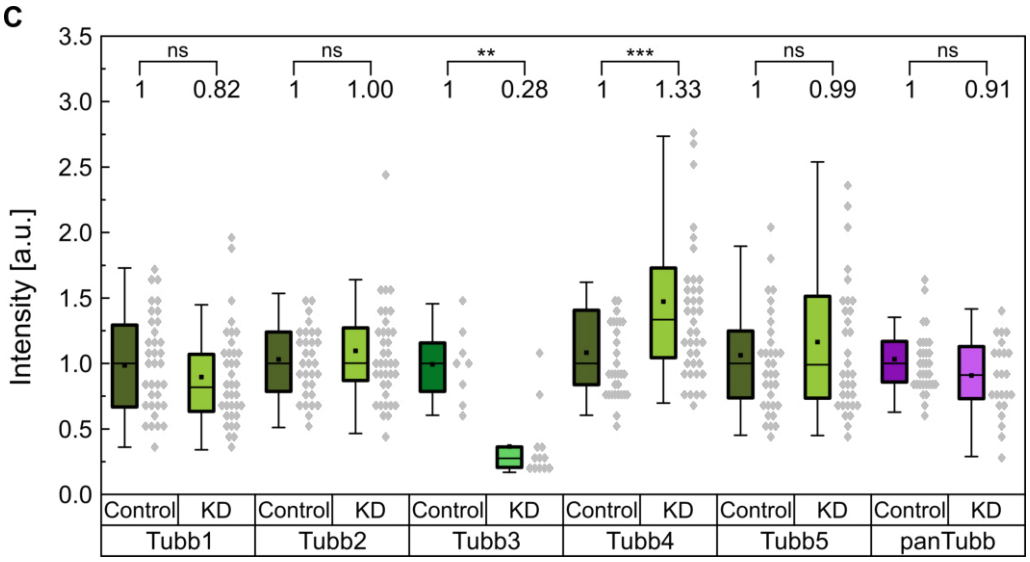

Figure 3.10. – Tubulin isotype signal intensities upon Tubb3 downregulation. (A1 - 3): Representative images of hippocampal neurons transfected with control or knockdown miRNA at DIV 9 and fixed at DIV 12. Scale bar, 50 µm. **(B1 - 3):** Enlargements of cell somata marked by the pink boxes in (A1 - 3). Tubulin isotype signal intensities were analyzed in DAPI negative regions as indicated by the yellow boxes. (A1): Tubb1 and Tubb2; (A2): Tubb3 and Tubb4; (A3): Tubb5 and panTubb; Scale bar, 5 µm. **(C):** Results of the tubulin isotype intensity measurements in the soma based on two independent experiments. Values were normalized to the respective control. Cells transfected with Tubb3 knockdown miRNA show a significant decrease in Tubb3 intensity to 0.28 a.u. *($p = 0.002$)* and a significant increase in Tubb4 intensity to 1.33 a.u. *($p < 0.001$)* compared to the respective control (set to 1). Tubb1, Tubb2, Tubb5 and panTubb show no significant difference in signal intensity, 0.82 a.u. *($p = 0.252$)*, 1.00 a.u. *($p = 0.64$)*, 0.99 a.u. *($p = 0.672$)* and 0.91 a.u. *($p = 0.089$)*, respectively, compared to their controls. Depicted are median values with 25th and 75th percentile. Whiskers indicate the range within 1.5 IQR. Black squares show the mean value. Each data point represents one cell; Tubb1: control (n = 35), KD (n = 36), Tubb2: control (n = 31), KD (n = 37), Tubb3: control (n = 8), KD (n = 12), Tubb4: control (n = 30), KD (n = 39), Tubb5: control (n = 33), KD (n = 33), panTubb: control (n = 32), KD (n = 33). For graphical representation of the distribution, data are binned with bin size 0.08 [a.u.]. Statistics: Mann-Whitney rank sum test, only for panTubb Student's t-test.

3.5. EB3 dynamics in neurons with reduced Tubb3 expression levels

The MT end-binding protein 3 (EB3) was used to investigate MT dynamics. It binds to the growing MT plus-end tip and here it was fused with a Tomato tag. The fusion protein mimics its endogenous counterpart and MT plus-end growth can be monitored in fluorescence live cell imaging. Neuronal hippocampal cultures were co-transfected with EB3-Tomato and the control or knockdown miRNA via Lipofectamine at DIV 9. Three days later they were imaged with a spinning disc confocal microscope (details in chapter 2.12). Figure 3.11 A shows representative frames of EB3 videos for the two conditions in dendrites and figure 3.11 B shows the tracing of representative comets over time. The videos were analyzed with ImageJ, by measuring the growth length, duration, and velocity with a self-written macro (described in chapter 2.13). In dendrites, cells transfected with the knockdown miRNA showed a significant increase in EB3 growth length compared to control cells. The duration of EB3 comet movements showed no significant difference between control and knockdown. The EB3 velocity was, as the growth length, significantly increased for Tubb3 knockdown cells compared to control cells. Figure 3.12 shows the EB3 analysis in axons. As for dendrites, figure 3.12 A shows representative frames of EB3 videos for the two conditions in axons and figure 3.12 B shows the tracing of representative comets over time. The growth length and duration of EB3 comets in axons showed no significant difference between knockdown and control. The EB3 velocity of cells transfected with the knockdown miRNA was significantly increased compared to control cells.

The significant differences in MT plus-end growth between cells with reduced Tubb3 expression and control cells in dendrites and axons confirm that isotype composition influences MT dynamics in living cells.

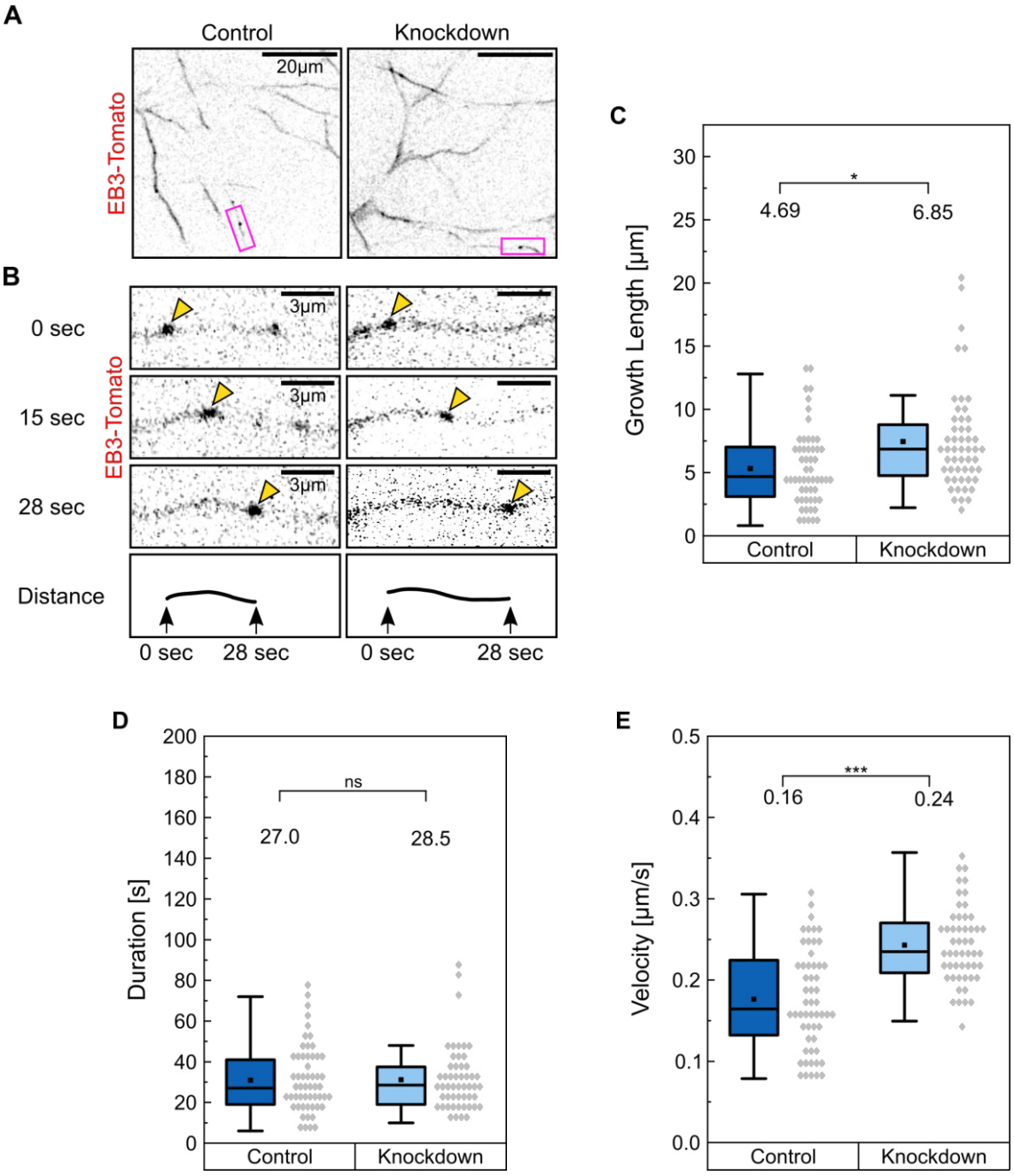

Figure 3.11. – Effects of reduced Tubb3 expression levels on EB3 dynamics in secondary dendrites. (A): Spinning disc confocal images of hippocampal neurons co-transfected with EB3-Tomato and the control or knockdown miRNA at DIV 9. Live cell imaging was conducted at DIV 12 with videos taken over three minutes and a frame rate of one per second. Shown are representative frames of the EB3 videos. Scale bar, 20 µm. **(B):** Enlargements of dendritic segments marked by the pink boxes in (A). EB3 comets were analyzed over time. Yellow arrowheads mark the movement of one representative comet for each condition over 28 seconds from top to bottom. The last panel visualizes the covered distance. Scale bar, 3 µm.

Continued on next page

Figure 3.11. – Effects of reduced Tubb3 expression levels on EB3 dynamics in secondary dendrites. (C - E): Quantification of EB3 comet movements based on three independent experiments. (C): Cells transfected with Tubb3 knockdown miRNA show a significant increase in EB3 growth length (6.85 µm), compared to the control (4.69 µm), *($p = 0.01$)*. (D): The duration of EB3 comet movements shows no significant difference between control (27 s) and knockdown (28.5 s), *($p = 0.799$)*. (E): Cells transfected with Tubb3 knockdown miRNA show a significant increase in EB3 velocity (0.24 µm/s), compared to the control (0.16 µm/s), *($p < 0.001$)*. Depicted are median values with 25th and 75th percentile. Whiskers indicate the range within 1.5 IQR. Black squares show the mean value. Each data point represents one EB3 comet; control (n = 55), knockdown (n = 52). For graphical representation of the distribution, data are binned with bin size: (C) 0.8 µm, (D) 5 s and (E) 0.015 µm/s. Statistics: Mann-Whitney rank sum test.

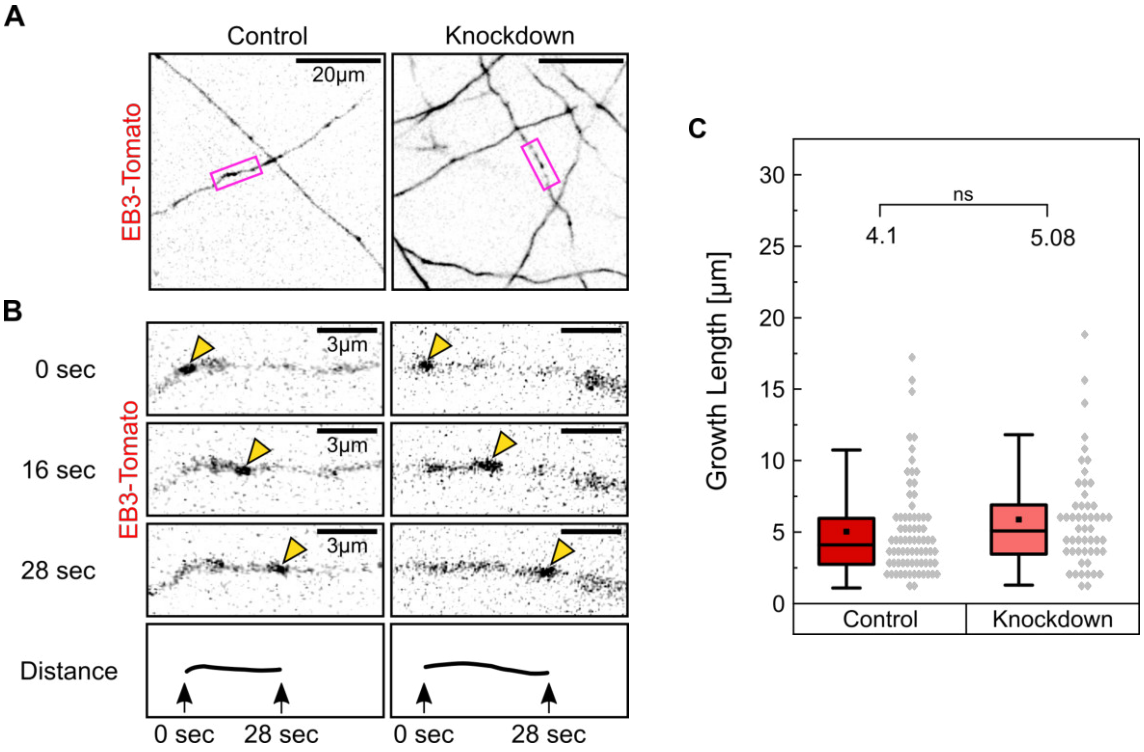

Figure 3.12. – *Continued on next page*

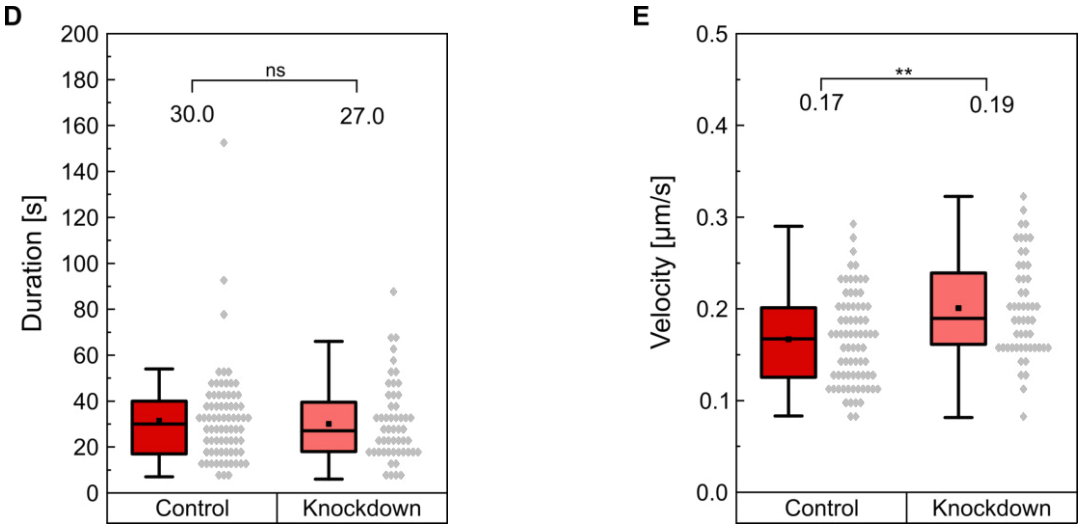

Figure 3.12. – Effects of reduced Tubb3 expression levels on EB3 dynamics in axons. (A): Spinning disc confocal images of hippocampal neurons co-transfected with EB3-Tomato and the control or knockdown miRNA at DIV 9. Live cell imaging was conducted at DIV 12 with videos taken over three minutes and a frame rate of one per second. Shown are representative frames of the EB3 videos. Scale bar, 20 µm. **(B):** Enlargements of axonal segments marked by the pink boxes in (A). EB3 comets were analyzed over time. Yellow arrowheads mark the movement of one representative comet for each condition over 28 seconds from top to bottom. The last panel visualizes the covered distance. Scale bar, 3 µm. **(C - E):** Quantification of EB3 comet movements based on three independent experiments. (C): Cells transfected with Tubb3 knockdown miRNA show no significant difference in growth length (5.08 µm), compared to the control (4.1 µm), *(p = 0.278)*. (D): The duration of EB3 comet movements shows no significant difference between control (30 s) and knockdown (27 s), *(p = 0.487)*. (E): Cells transfected with Tubb3 knockdown miRNA show a significant increase in EB3 velocity (0.19 µm/s), compared to the control (0.17 µm/s), *(p = 0.004)*. Depicted are median values with 25th and 75th percentile. Whiskers indicate the range within 1.5 IQR. Black squares show the mean value. Each data point represents one EB3 comet; control (n = 75), knockdown (n = 52). For graphical representation of the distribution, data are binned with bin size: (C) 0.8 µm, (D) 5 s and (E) 0.015 µm/s. Statistics: Mann-Whitney rank sum test.

3.6. KIF5C motor movement in neurons with reduced Tubb3 levels

After finding influences of Tubb3 expression levels on EB3 growth and, therefore, MT dynamics, the next step was to investigate transport processes by analyzing motor protein movement on MTs. Processive motor proteins are the main actors of directed transport and therefore of special importance in neuronal protein delivery into dendrites and axons. From the kinesin superfamily proteins (KIFs), kinesin-1, more precisely KIF5C, transports, amongst others, N-Cadherin and AMPA receptors and is thereby important for synaptic formation and plasticity [Lee, 2011, Hirokawa and Takemura, 2005]. A fusion protein of the KIF5C motor domain with a Tomato tag was used for visualization and the peroxisome assembly protein 26 (PEX26) to activate the motor by recruiting peroxisomes as artificial cargo. Neuronal hippocampal cultures were co-transfected with KIF5C-Tomato-PEX and either control miRNA or knockdown miRNA via calcium phosphate at DIV 9. Live cell imaging was conducted three days later. Figure 3.13 A shows representative frames of the transfection marker GFP (co-expressed with miRNA) for the two conditions in dendrites and figure 3.13 B shows the tracing of representative KIF5C motor movements over time. The quantification showed no significant differences in run length, duration, and velocity of KIF5C motor movement between control and knockdown cells. Figure 3.14 shows the KIF5C analysis in axons. Again, figure 3.14 A shows representative frames of the transfection marker GFP for the two conditions and figure 3.14 B shows the tracing of representative KIF5C motor movements in axons over time. The quantification showed no significant difference in motor run length between cells transfected with control and knockdown miRNA. The duration of KIF5C motor movement in cells transfected with the knockdown miRNA was significantly decreased compared to the control. Whereas, the motor velocity of cells transfected with the knockdown miRNA was significantly increased compared to the control.
Since significant differences in KIF5C motor protein movement between cells with reduced Tubb3 expression and control cells in axons were shown, the following experiment analyzed if the potential cargo N-Cadherin was influenced.

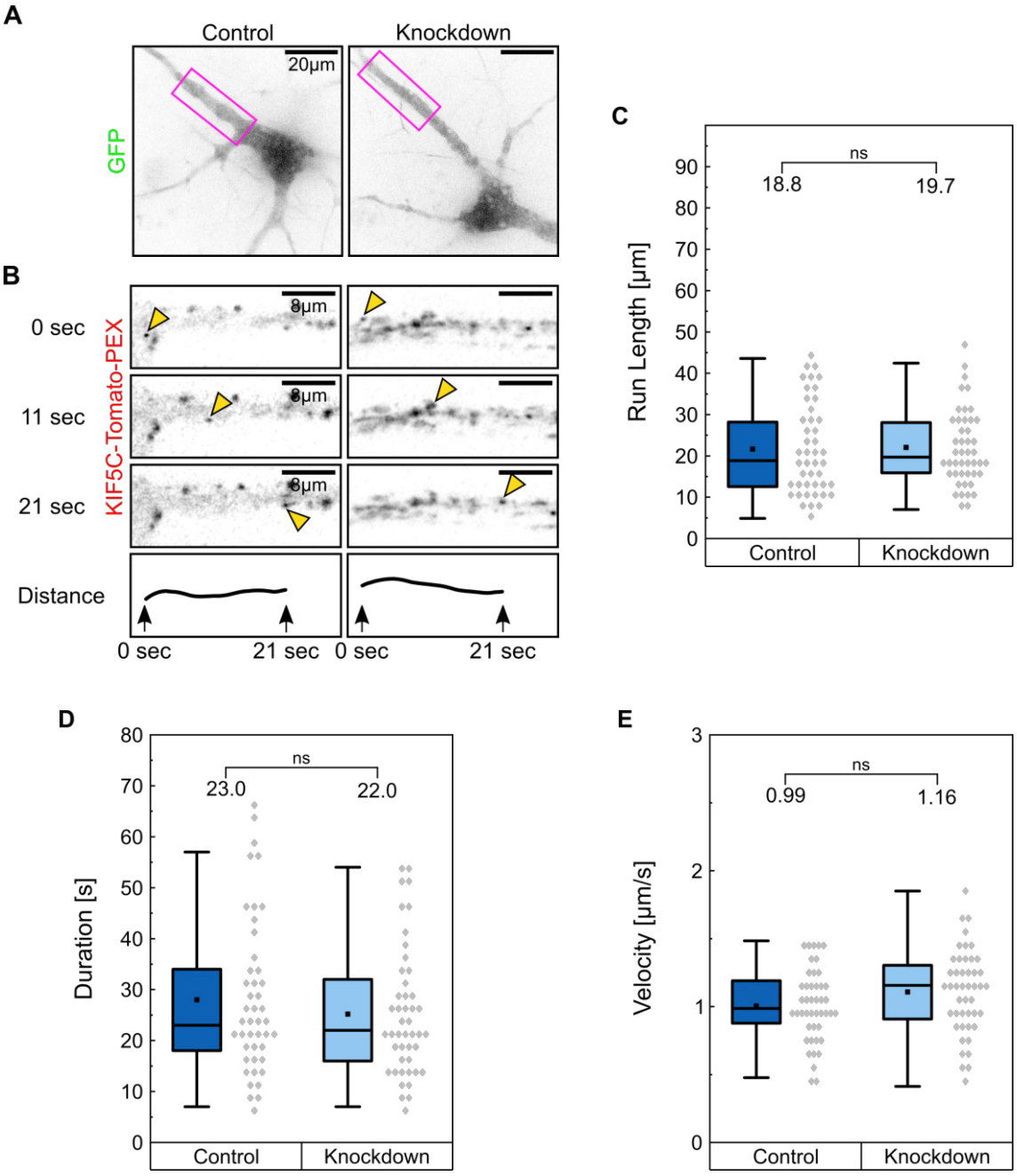

Figure 3.13. – Effects of Tubb3 downregulation on KIF5C motor protein movement in dendrites. (A): Spinning disc confocal images of hippocampal neurons co-transfected with KIF5C-Tomato-PEX and control or knockdown miRNA at DIV 9. Live cell imaging was conducted at DIV 12 with videos taken over three minutes and a frame rate of one per second. Representative frames of the transfection marker GFP are shown. Scale bar, 20 µm.
Continued on next page

Figure 3.13. – Effects of Tubb3 downregulation on KIF5C motor protein movement in dendrites. (B): Enlarged dendritic segments taken from KIF5C-Tomato-PEX frames of the area marked by the pink boxes in (A). Motor movements were analyzed over time. Yellow arrowheads mark the movement of one representative motor protein for each condition over 21 seconds from top to bottom. The lowest panel visualizes the covered distance. Scale bar, 8 µm. **(C - E):** Quantification of KIF5C motor protein movements based on three independent experiments. (C): Cells transfected with Tubb3 knockdown miRNA show no significant difference in run length (19.7 µm), compared to the control (18.8 µm), *(p = 0.587)*. (D): The duration of KIF5C motor movement also shows no significant difference between control (23 s) and knockdown (22 s) *(p = 0.507)*. (E): Cells transfected with Tubb3 knockdown miRNA show no significant difference in KIF5C motor protein velocity (1.16 µm/s), compared to the control (0.99 µm/s), *(p = 0.092)*. Depicted are median values with 25th and 75th percentile. Whiskers indicate the range within 1.5 IQR. Black squares show the mean value. Each data point represents one KIF5C motor protein; control (n = 45), knockdown (n = 46). For graphical representation of the distribution, data are binned with bin size: (C) 2.6 µm, (D) 2.5 s and (E) 0.1 µm/s. Statistics: Mann-Whitney rank sum test in (C) and (D), Student's t-test in (E).

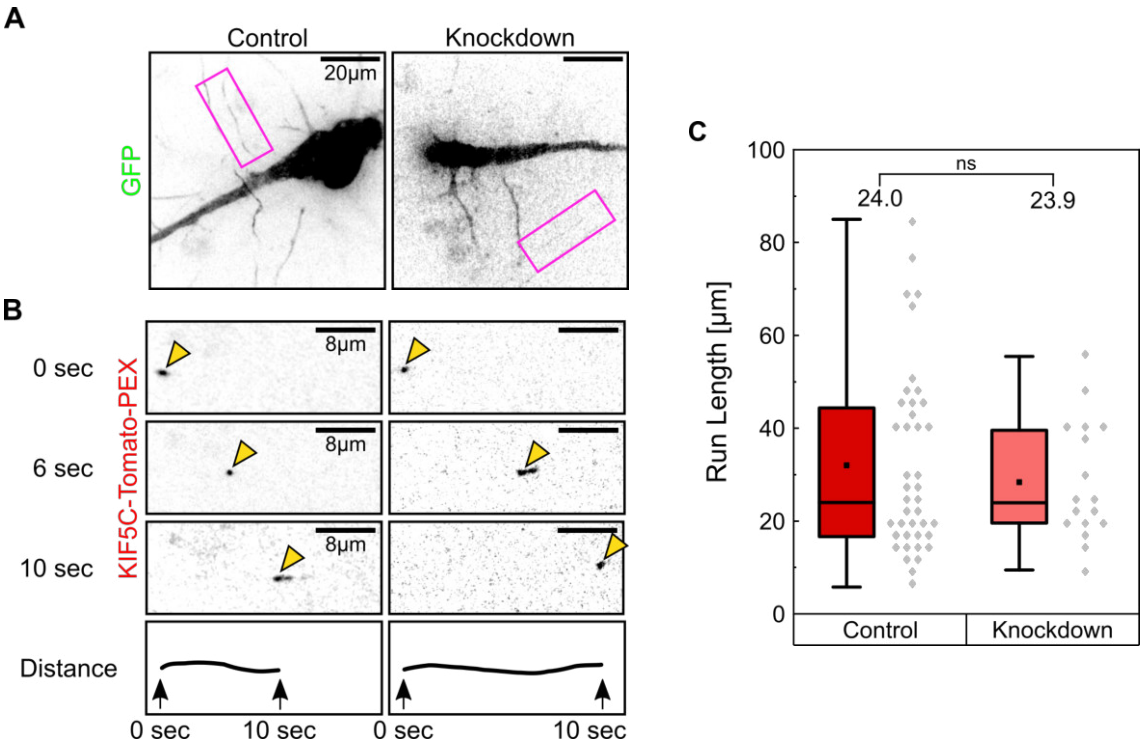

Figure 3.14. – *Continued on next page*

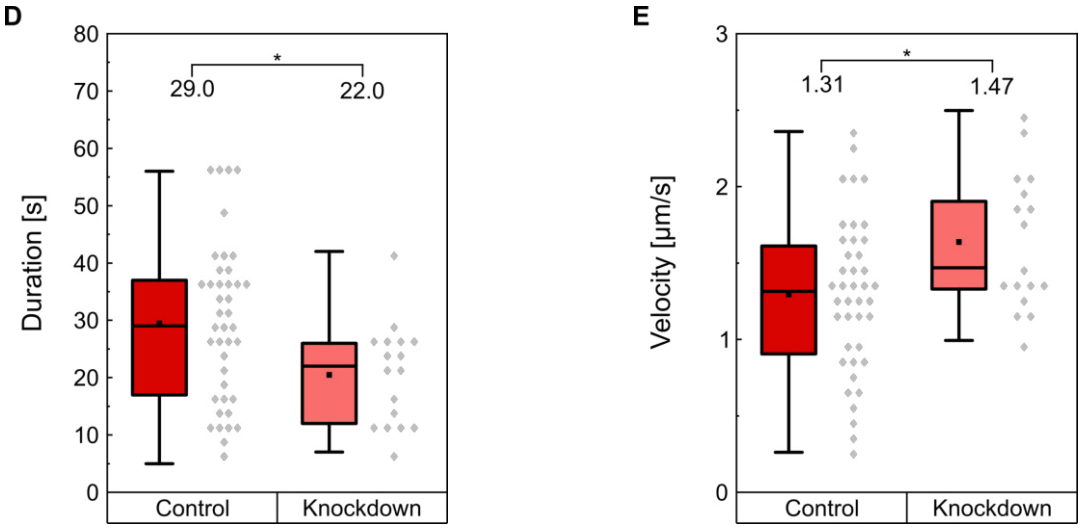

Figure 3.14. – Effects of Tubb3 downregulation on KIF5C motor protein movement in axons. (A): Spinning disc confocal images of hippocampal neurons co-transfected with KIF5C-Tomato-PEX and control or knockdown miRNA at DIV 9. Live cell imaging was conducted at DIV 12 with videos taken over three minutes and a frame rate of one per second. Representative frames of the transfection marker GFP are shown. Scale bar, 20 µm. **(B):** Enlarged axonal segments taken from KIF5C-Tomato-PEX frames of the area marked by the pink boxes in (A). Motor movements were analyzed over time. Yellow arrowheads mark the movement of one representative motor protein for each condition over 10 seconds from top to bottom. The lowest panel visualizes the covered distance. Scale bar, 8 µm. **(C - E):** Quantification of KIF5C motor protein movements based on three independent experiments. (C): Cells transfected with Tubb3 knockdown miRNA show no significant difference in run length (23.9 µm), compared to the control (24.0 µm), *($p = 0.838$)*. (D): The duration of KIF5C motor movement in cells transfected with knockdown miRNA (22 s) is significantly decreased compared to control cells (29 s), *($p = 0.017$)*. (E): Cells transfected with Tubb3 knockdown miRNA show a significant increase in KIF5C motor protein velocity (1.47 µm/s), compared to the control (1.31 µm/s), *($p = 0.018$)*. Depicted are median values with 25th and 75th percentile. Whiskers indicate the range within 1.5 IQR. Black squares show the mean value. Each data point represents one KIF5C motor protein; control (n = 41), knockdown (n = 17). For graphical representation of the distribution, data are binned with bin size: (C) 2.6 µm, (D) 2.5 s and (E) 0.1 µm/s. Statistics: Mann-Whitney rank sum test in (C), and Student's t-test in (D) and (E).

3.7. N-Cadherin transport in neurons with reduced Tubb3 levels

As a cargo that is transported by kinesin motor proteins [Lee, 2011], N-Cadherin movement was analyzed in neurons with reduced Tubb3 expression. N-Cadherin is a transmembrane protein and, amongst others, important for synapse formation and maturation [Hirano and Takeichi, 2012]. Here it was used as a red fluorescent protein (RFP) fusion protein, which mimicked the endogenous N-Cadherin transport. Neuronal hippocampal cultures were co-transfected with NCad-RFP and control or knockdown miRNA. Figure 3.15 A shows representative frames of the transfection marker GFP (co-expressed with miRNA) for the two conditions in dendrites and figure 3.15 B shows the tracing of representative N-Cadherin cargo movements over time. Cells transfected with the knockdown miRNA showed no significant difference in N-Cadherin run length compared to the control. The duration of cargo movement in cells transfected with the knockdown miRNA was significantly decreased compared to control cells. The velocity of N-Cadherin showed no significant difference between knockdown and control. Figure 3.16 shows the results of the axon analysis. The N-Cadherin run length showed no significant difference between control and knockdown. The cargo duration in cells transfected with the knockdown miRNA showed a significant decrease compared to the control and the N-Cadherin velocity of cells transfected with knockdown miRNA showed a significant increase compared to the control. The significant differences in N-Cadherin transport between cells with reduced Tubb3 expression and control cells led to the question if its distribution on the cell surface was also changed.

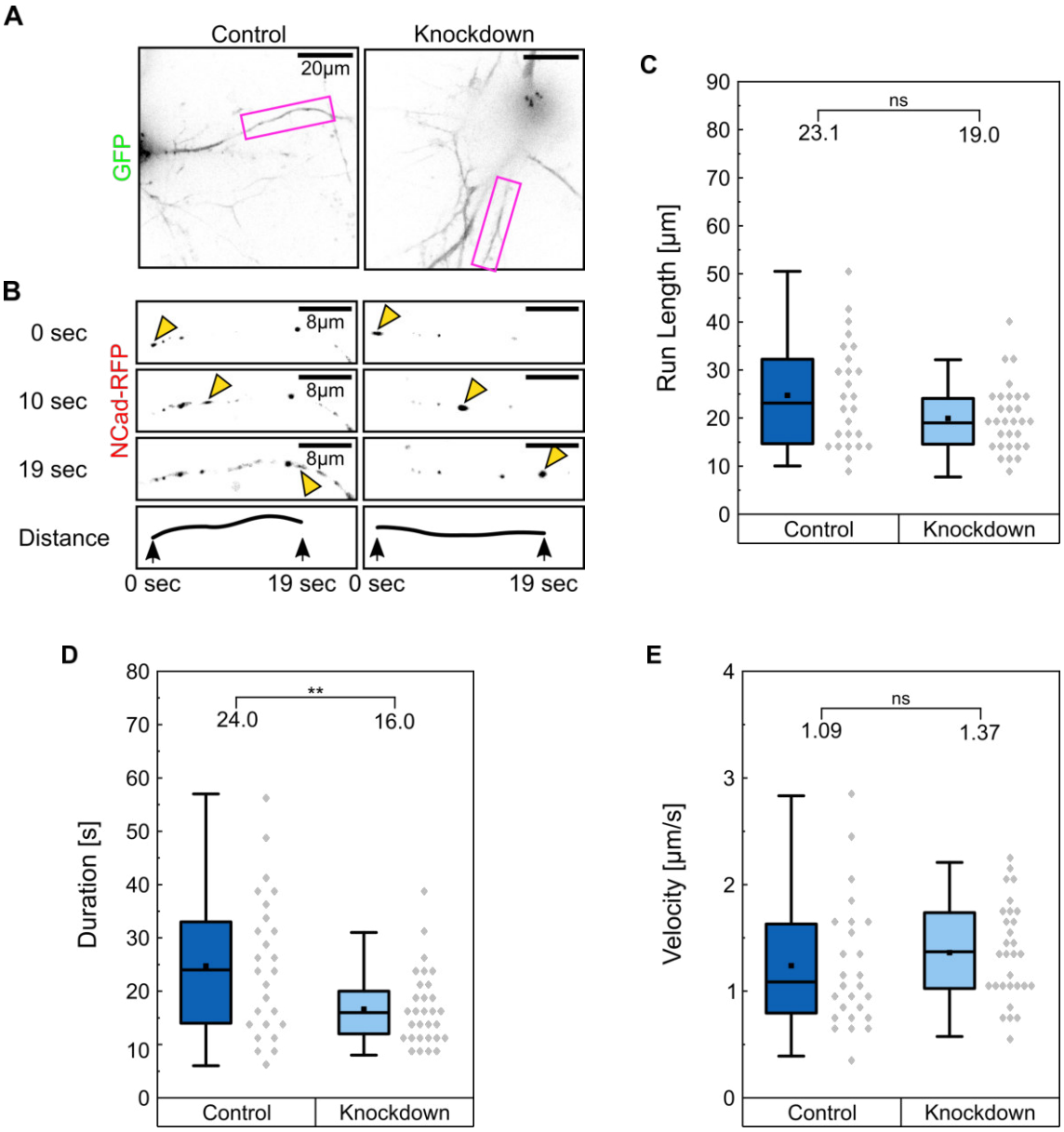

Figure 3.15. – Effects of Tubb3 downregulation on N-Cadherin transport in dendrites. (A): Spinning disc confocal images of hippocampal neurons co-transfected with NCad-RFP and control or knockdown miRNA at DIV 9. Live cell imaging was conducted at DIV 12 with videos taken over three minutes and a frame rate of one per second. Representative frames of the transfection marker GFP are shown. Scale bar, 20 µm. **(B):** Enlarged dendritic segments taken from NCad-RFP frames of the area marked by the pink boxes in (A). Cargo transport was analyzed over time. Yellow arrowheads mark the movement of one representative N-Cadherin cargo protein for each condition over 19 seconds from top to bottom. The lowest panel visualizes the covered distance. Scale bar, 8 µm. **(C - E):** Quantification of N-Cadherin movements based on three independent experiments. (C): Cells transfected with Tubb3 knockdown miRNA show no significant difference in run length (19.0 µm), compared to the control (23.1 µm), *($p = 0.062$).* (D): The cargo duration shows a significant difference between control (24 s) and knockdown (16 s), *($p = 0.008$).*

Continued on next page

Figure 3.15. – Effects of Tubb3 downregulation on N-Cadherin transport in dendrites. (E): Cells transfected with Tubb3 knockdown miRNA show no significant difference in N-Cadherin transport velocity (1.37 µm/s), compared to the control (1.09 µm/s), *($p = 0.209$)*. Depicted are median values with 25th and 75th percentile. Whiskers indicate the range within 1.5 IQR. Black squares show the mean value. Each data point represents one N-Cadherin cargo protein; control (n = 26), knockdown (n = 30). For graphical representation of the distribution, data are binned with bin size: (C) 2.6 µm, (D) 2.5 s and (E) 0.1 µm/s. Statistics: Welch's t-test in (C) and (D), Mann-Whitney rank sum test in (E).

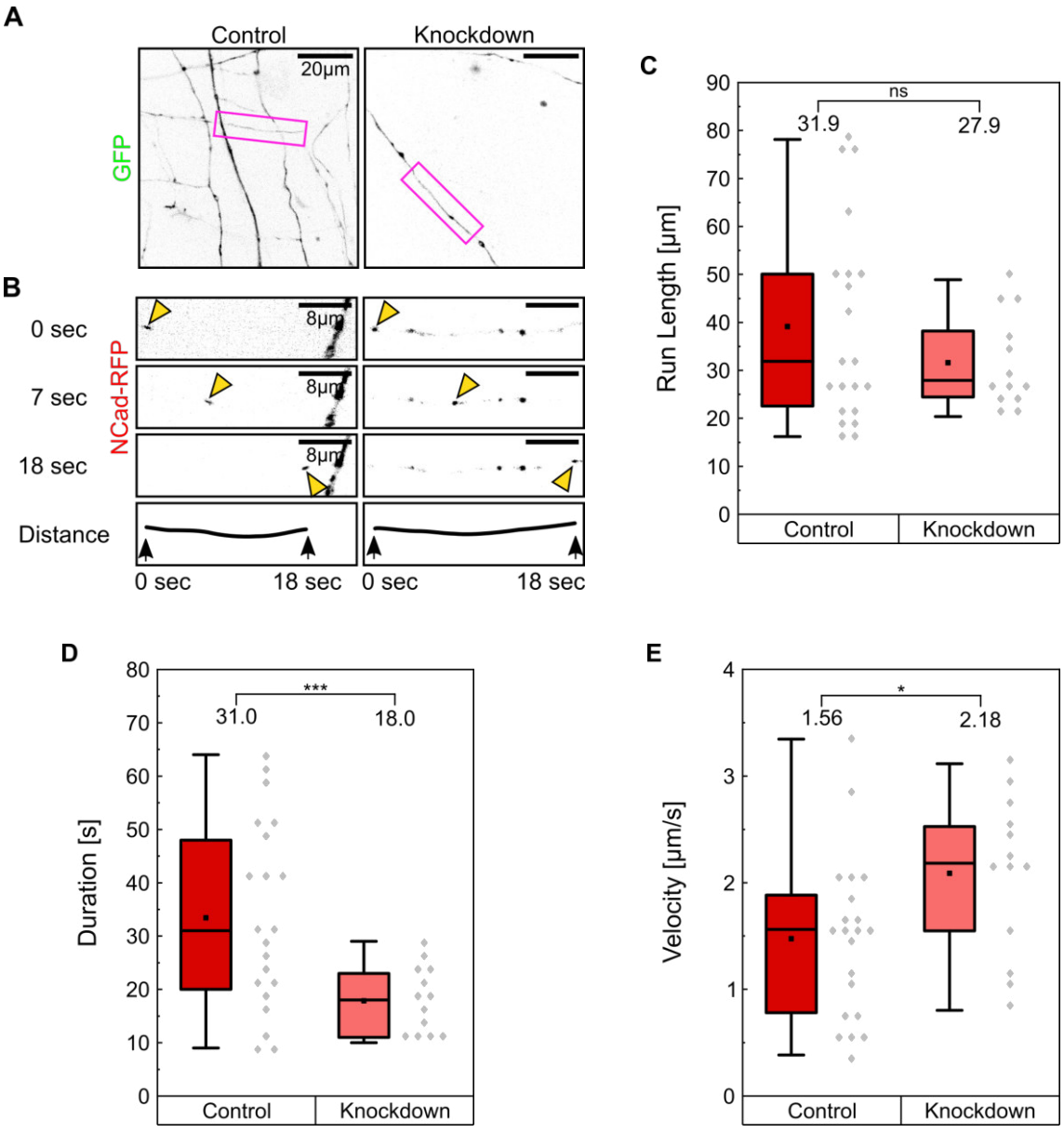

Figure 3.16. – *Continued on next page*

Figure 3.16. – Effects of Tubb3 downregulation on N-Cadherin transport in axons. (A): Spinning disc confocal images of hippocampal neurons co-transfected with NCad-RFP and control or knockdown miRNA at DIV 9. Live cell imaging was conducted at DIV 12 with videos taken over three minutes and a frame rate of one per second. Representative frames of the transfection marker GFP are shown. Scale bar, 20 µm. **(B):** Enlarged axonal segments taken from NCad-RFP frames of the area marked by the pink boxes in (A). Cargo transport was analyzed over time. Yellow arrowheads mark the movement of one representative N-Cadherin cargo protein for each condition over 18 seconds from top to bottom. The lowest panel visualizes the covered distance. Scale bar, 8 µm. **(C - E):** Quantification of N-Cadherin movements based on three independent experiments. (C): Cells transfected with Tubb3 knockdown miRNA show no significant difference in run length (27.9 µm), compared to the control (31.9 µm), *($p = 0.595$)*. (D): The duration of N-Cadherin movement shows a significant difference between control (31 s) and knockdown (18 s) cells, *($p < 0.001$)*. (E): Cells transfected with Tubb3 knockdown miRNA show a significant increase in N-Cadherin transport velocity (2.18 µm/s), compared to the control (1.56 µm/s), *($p = 0.028$)*. Depicted are median values with 25th and 75th percentile. Whiskers indicate the range within 1.5 IQR. Black squares show the mean value. Each data point represents one N-Cadherin cargo protein; control (n = 21), knockdown (n = 13). For graphical representation of the distribution, data are binned with bin size: (C) 2.6 µm, (D) 2.5 s and (E) 0.1 µm/s. Statistics: Mann-Whitney rank sum test in (C), Welch's t-test in (D) and Student's t-test in (E).

3.7.1. N-Cadherin surface intensity in axons

After finding significant differences in motor and cargo movement in axons with reduced Tubb3 expression, it was analyzed if this influences N-Cadherin distribution. Therefore, the N-Cadherin surface intensity in axons was measured. Neuronal hippocampal cultures were transfected with control and Tubb3 knockdown miRNA, three days later cells were fixed and immuno-stained for N-Cadherin and Ankyrin-G. Ankyrin-G is a marker of the axon initial segment and enables to identify the axons of transfected cells. Representative images and quantification are shown in figure 3.17. N-Cadherin surface intensity was measured for two distances from the soma, both areas were 30 µm long (pink boxes in A). Panel B shows the enlargements of the axonal segment with 30 µm distance to the soma and Panel C the ones with 150 µm distance. The axonal regions were determined based on the GFP expression and transferred into the N-Cadherin staining. N-Cadherin signal intensities were measured in these axonal regions outlined in yellow. The quantification showed no significant difference in N-Cadherin surface signal intensity for cells transfected with Tubb3 knockdown miRNA, compared to the control (set to one) for 30 and 150 µm distance.

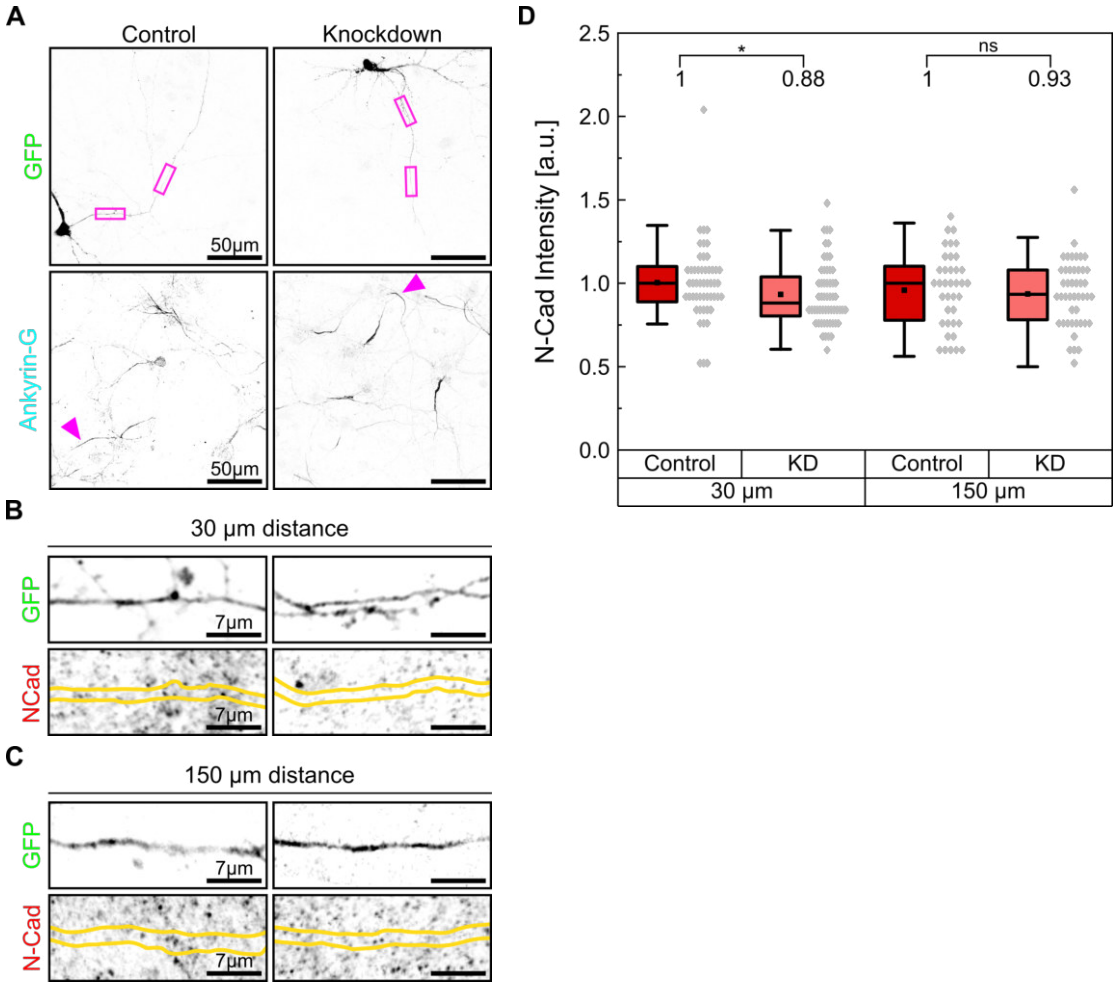

Figure 3.17. – **N-Cadherin surface intensity in axons. (A):** Representative images of hippocampal neurons transfected with control miRNA or knockdown miRNA at DIV 9. Cells were fixed at DIV 12 and immuno-stained for N-Cadherin and Ankyrin-G. Transfected neurons were identified via GFP expression and axons via an Ankyrin-G staining, which marks the axon initial segment. Axons of transfected cells are marked by pink arrowheads. N-Cadherin surface intensity was measured in two 30 µm long areas, one with a distance of 30 µm to the soma and the second with a distance of 150 µm (pink boxes). Scale bar, 50 µm. **(B):** Enlargements of axonal segments 30 µm away from the soma marked by pink boxes in (A). The axonal regions were determined based on the GFP expression and transferred into the N-Cadherin staining (NCad, yellow lines). N-Cadherin signal intensities were measured in these axonal regions outlined in yellow. Scale bar, 7 µm. **(C):** Enlargements of axonal segments 150 µm away from the soma marked by pink boxes in (A). The axonal regions were determined based on the GFP expression and transferred into the N-Cadherin staining (NCad, yellow lines). N-Cadherin signal intensities were measured in these axonal regions outlined in yellow. Scale bar, 7 µm.
Continued on next page

Figure 3.17. – N-Cadherin surface intensity in axons. (D): Quantification of N-Cadherin signal intensity measurements based on two independent experiments. At 30 µm distance from the soma cells transfected with the knockdown miRNA show no significant difference in N-Cadherin signal intensity, 0.93 a.u. *($p = 0.085$)* compared to the control (set to 1). At 150 µm distance from the soma cells transfected with the knockdown miRNA also show no significant difference in N-Cadherin signal intensity, 0.98 a.u. *($p = 0.628$)* compared to the control (set to 1). Depicted: mean ± SEM. Each data point represents one cell; control (n = 50), KD (n = 56). Statistics: Student's t-test.

4. Microtubule modeling

4.1. Basics

Due to the large number of possible tubulin isotypes in mammalian neurons and the limited access to isotype-specific antibodies, a computational simulation was developed to predict microtubule (MT) growth in silico. This chapter complements the experimental data of MT growth in dissociated hippocampal cultures with a biophysical model. Several kinds of MT models exist in literature [VanBuren et al., 2002, VanBuren et al., 2005, Gardner et al., 2011b, Castle et al., 2017, Hemmat et al., 2019], but none of them included different tubulin isotypes as building blocks of MTs. To simulate MT growth velocities, a two-dimensional computational Monte Carlo model was developed that incorporated three different tubulin dimer types as building blocks. The model was based on the 2D model published by VanBuren et al. [VanBuren et al., 2002] and extended by several dimer types. The aim of this simulation was to model the EB3 data presented in chapter 3.5 and was therefore focused on MT growth. MT catastrophe, shrinkage, rescue and GTP hydrolysis were neglected. The basis of the model was the MT-grid shown in figure 4.1. The 3D MT tube was flattened into a 2D protofilament sheet. Each rectangle represents one alpha- and beta-tubulin dimer, which build up the protofilaments marked by numbers 1 to 13. Periodic boundaries mirrored protofilament 1 next to protofilament 13 and vice versa, so that a continues grid was generated. Bonds between dimers along one protofilament were characterized by longitudinal bond energies. Bonds between dimers of neighboring protofilaments were characterized by lateral bond energies. Protofilament 1 and 13 were shifted by 1.5 dimers to represent the MT seam. Accordingly, each dimer had 0, 0.5, 1, 1.5 or 2 lateral neighbors.

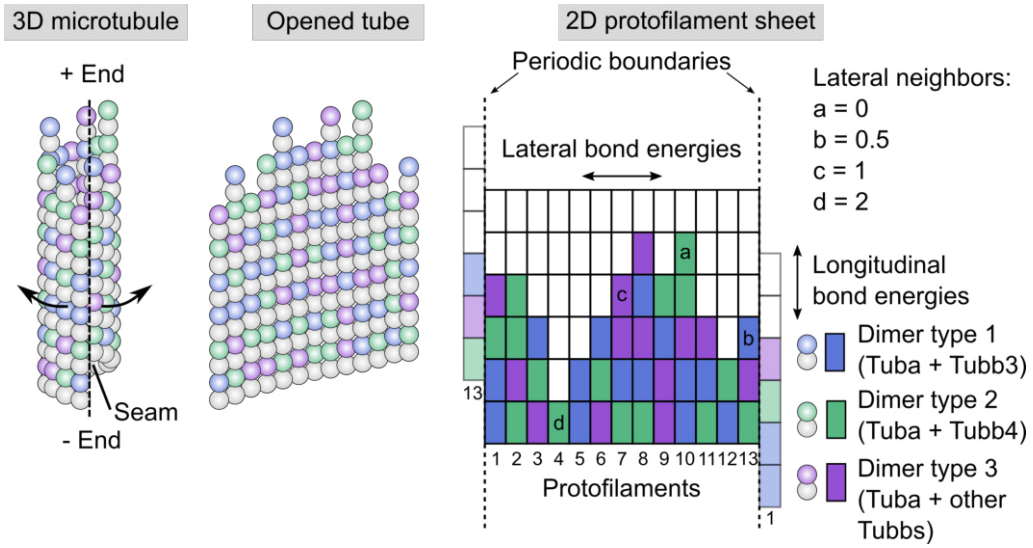

Figure 4.1. – Microtubule 2D grid. A 3D MT tube was flattened into a 2D protofilament sheet. Tubulin dimers of types 1, 2, and 3 are depicted as rectangles of blue, green and violet color, respectively. They longitudinally bind together to build up the protofilaments marked by numbers 1 to 13. Periodic boundaries mirror protofilament 1 next to protofilament 13 and vice versa, so that a continues grid is generated. Protofilaments 1 and 13 are shifted by 1.5 dimers to mimic the MT seam. Longitudinal energies bind dimers along one protofilament and lateral energies bind dimers of neighboring protofilaments. Dimers a, b, c, and d represent dimers with a different number of lateral neighbors. Illustrating 0.5 and 1.5 lateral neighbors in one example was not possible, so the case of 1.5 lateral neighbors was not shown.

During the growing phase of a MT, dimers stochastically bound to or dissociated from the protofilament tips. If more dimers were bound than were dissociated, the MT increased in length. Binding and unbinding were characterized by the bimolecular on-rate constant $k_{on}(M^{-1}s^{-1})$, and the unimolecular off-rate constant $k_{off}(s^{-1})$. They were related by the equilibrium constant of polymerization $K(M^{-1})$ [VanBuren et al., 2002]:

$$K = \frac{k_{on}}{k_{off}}. \tag{4.1}$$

The bimolecular on-rate constant was multiplied with the tubulin concentration to give a pseudo first order on-rate constant $k_{on}(s^{-1})$. The standard Gibbs free energy change was described by:

$$\Delta G = -RT\ ln(K), \tag{4.2}$$

with R being the universal gas constant and T the absolute temperature in kelvin. It was assumed, that every dimer that binds to a protofilament, forms one longitudinal bond, changing the free energy by ΔG_{long}. The energy changes for dimer immobilization and conformational change were included into ΔG_{long} to simplify the parameter set. For each lateral neighbor, the energy ΔG_{lat} was added, leading to a change in the free energy upon dimer binding of:

$$\Delta G = \Delta G_{long} + x\ \Delta G_{lat}, \tag{4.3}$$

with x being the number of lateral neighbors. Therefore, with a given k_{on} and combining equations 4.1, 4.2 and 4.3, k_{off} was calculated as:

$$k_{off} = \frac{k_{on}}{\exp(-\frac{\Delta G_{long} + x\ \Delta G_{lat}}{RT})}. \tag{4.4}$$

Most MT models in literature consider only one dimer type as building block for MTs. To model the growth velocities of MT plus-ends with reduced Tubb3 and increased Tubb4 amounts, three different dimer types as building blocks were implemented. To hypothesize about similarities and differences in longitudinal and lateral energies, the sequences of mouse beta-tubulin isotypes were analyzed. Alignments are shown in figure 4.2. Sequence regions associated with lateral dimer binding [Meurer-Grob et al., 2001] were marked with red boxes and regions involved in longitudinal binding [Meurer-Grob et al., 2001] with blue boxes. Differences in the amino acid sequences between isotypes were colored. They showed that the longitudinal binding sites did not differ between isotypes, whereas the amino acid sequence associated with the lateral binding sites did differ between isotypes. Therefore, for calculations in a cell free environment, equal longitudinal energies and on rate constants, but different lateral energies and off rate constants were assumed for different isotypes.

Figure 4.2. – Mouse beta-tubulin isotype amino acid sequence alignment. Alignment of beta-tubulin isotype amino acid sequences performed with the software MegAlign (DNASTAR, version 15.3.0) using the MUSCLE algorithm. The ruler marks the amino acid positions. Differences in the isotype sequences from the consensus are marked with boxes colored according to their biochemical characteristics indicated by the legend. Regions involved in lateral binding of dimers are marked in red and regions associated with longitudinal binding are marked in blue. Adapted from [Hausrat et al., 2020].

4.2. Simulation procedure

The first step of the simulation procedure was to formulate a list of possible events. A diagram of the program code is shown in figure 4.3. To each protofilament end a dimer of type one, two or three, reflecting individual combinations of tubulin isotypes, could bind. To consider the sterical hindrance of already existing lateral neighbors at the possible binding site, an on-rate penalty of 2 ($k_{on}/2$) was introduced for one lateral neighbor and a penalty of 10 ($k_{on}/10$) for two lateral neighbors [Gardner et al., 2011b]. Additionally, each dimer of the grid could unbind. As shown in equation 4.4 the number of lateral neighbors determined the quantity of bound lateral energy and influenced k_{off}. If a dimer dissociated from a position inside the grid, all upper dimers of this protofilament also dissociated and the lateral energies of the respective dimer and all the above dimers were summed up. This made the unbinding of a dimer more than a few layers deep a very rare event. To enable dissociation from the beginning of the simulation, protofilaments were given a start-length of 70 or 10 dimers each. Dimer types were chosen within a Monte Carlo simulation randomly to yield a uniform distribution of dimers. In the second step the execution time $t\,(s)$ for each event in the list was calculated according to literature [VanBuren et al., 2002]:

$$t_i = \frac{-\ln(N_i)}{k_i}, \tag{4.5}$$

with i being the index of the possible event, N being a uniformly distributed random number between 0 and 1, and k being the rate constant (s^{-1}) of the event. The third step was to implement the event with the shortest execution time and add this time to the total elapsed time. Then steps one to three were repeated as often as defined by the user. In order to model velocities, as observed experimentally, steps one to three were repeated 5000 times. Simulation parameters were k_{on}, ΔG_{long}, $\Delta G_{lat}1$, $\Delta G_{lat}2$, $\Delta G_{lat}3$ and the tubulin dimer concentrations $C1$, $C2$ and $C3$. The final output was the time of growth and the length of the protofilaments, from which the growth velocity of the MT tip could be calculated by:

$$\text{velocity} = \frac{\text{mean length of protofilaments}}{\text{total elapsed time}}. \tag{4.6}$$

The complete source code of the program is given in appendix A.2.

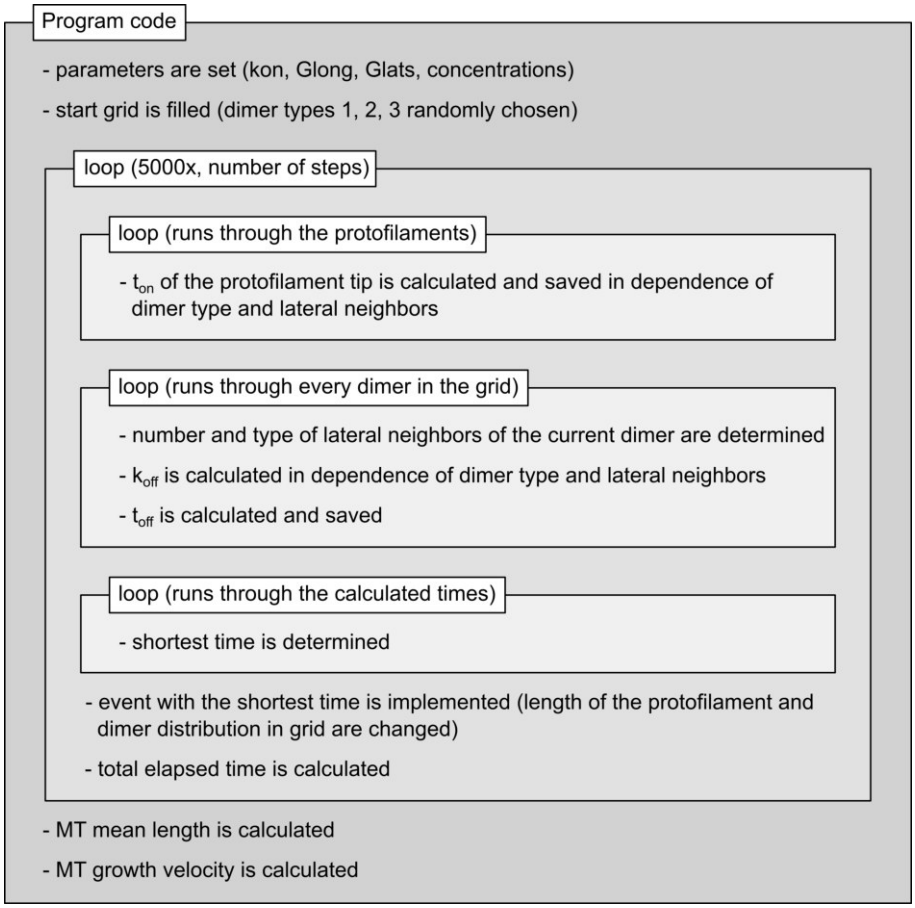

Figure 4.3. – Simulation code diagram.

4.3. Parameter determination on the basis of a cell free environment

Tubulin heterodimers consist of one alpha-tubulin and one beta-tubulin. The present study was focused on beta-tubulin isotypes, therefore alpha-tubulin isotypes were not differentiated. To determine the parameters, the model was adjusted to match experimental EB3 imaging data. Accordingly, dimer type 1 was defined to represent Tubb3-containing dimers and dimer type 2 to represent Tubb4-containing dimers. Since free energy changes are additive, dimer type 3 was defined to represent all other beta-tubulin isotype-containing dimers (Figure 4.1). In literature, values for k_{on} and ΔG_{long} range from $1\,\mu M^{-1}\mathrm{s}^{-1}$ to $8.9\,\mu M^{-1}\mathrm{s}^{-1}$ [Gardner et al., 2011b] and from $-5.8\,RT$ to $-18\,RT$ [Hemmat et al., 2019], respectively. Values published by Castle et al. [Castle et al., 2017] were used to determine further parameters in a cell free environment, because the *in vitro* values of $6\,\mu M^{-1}\mathrm{s}^{-1}$ for k_{on} and $-7.2\,RT$ for ΔG_{long} were enhancements of the same 2D model that was

used as a basis in this study [VanBuren et al., 2002]. Their publication additionally included a parameter set for dynamic instability *in vivo*, which was utilized for the modeling in a cellular environment. To determine the lateral energy values of ΔG_{lat}(Tubb3) and ΔG_{lat}(Tubb4) in a cell free environment, *in vitro* velocity values from the publication of Vemu et al. [Vemu et al., 2017] were extracted using the WebPlotDigitizer version 4.3. They included MT plus end growth rates purified from mouse brain tissue (containing all natural isotypes), tsA201 cells (containing Tuba1b, Tubb1, Tubb4b) and recombinant single-isotype human tubulin (containing Tuba1a, Tubb3). At $6\,\mu M$ tubulin concentration, brain derived MTs grew with $0.008\,\mu m/s$, Tubb1/Tubb4b containing MTs with $0.0146\,\mu m/s$ and Tubb3 containing MTs with $0.0102\,\mu m/s$ [Vemu et al., 2017]. To simplify the parameters, the published velocity for Tubb1/Tubb4b dimers was used in the model for Tubb4 dimers. Since the MTs in these cell free environment experiments with Tubb3 and Tubb4 were build out of one dimer type, the program was used as if only one dimer type existed. This means that the program was executed with the same ΔG_{lat} for all dimer types and concentrations $C1 = C2 = C3 = 2\,\mu M$ to have a total concentration of $6\,\mu M$. To determine the corresponding lateral energy values for ΔG_{lat}(Tubb3) and ΔG_{lat}(Tubb4) the program was executed with several ΔG_{lat} values ranging from -2.4 to $-8\,RT$ in 0.2 steps and the resulting velocities were plotted in figure 4.4 A. The program was executed 10 times and each of the plots was fitted with the function: velocity $= A - B/(\exp(C\,\Delta G_{lat} + D))$. With the calculated fit parameter A, B, C, D and the published velocities (Tubb3: $0.0102\,\mu m/s$, Tubb1/Tubb4b: $0.0146\,\mu m/s$), the corresponding lateral energies were calculated by:

$$\Delta G_{lat} = \frac{\ln\left(\frac{B}{A-\text{velocity}}\right) - C}{C}. \tag{4.7}$$

The results for ΔG_{lat}(Tubb3) and ΔG_{lat}(Tubb4) are shown in figure 4.4 B. The lateral energy of Tubb3 ($-3.67\,RT$) was significantly higher than the lateral energy of Tubb4 ($-3.79\,RT$). This difference in lateral energies originated purely from the different isotypes building up the MTs, since the experiments in a cell free environment did not contain any further proteins as MTBPs or PTMs inducing proteins that could influence the tubulin assembly. Since in neuronal cells, MTs contain all beta-tubulin isotypes, additionally to the lateral energies of Tubb3 and Tubb4 the combined lateral energy value of the other beta-tubulin isotypes was calculated. For that the program was executed with the same k_{on} and ΔG_{long} as before, but the tubulin concentrations were adjusted. The RNA expression data shown before (chapter 3.1) suggest an isotype percentage of Tubb3 $\hat{=}$ 14%, Tubb4 $\hat{=}$ 28% and

rest (Tubb1, Tubb2, Tubb5, Tubb6) $\hat{=}$ 58% in adult mouse brain tissue. With a total tubulin concentration of $6\,\mu M$ that gave concentrations of C(Tubb3) = $0.84\,\mu M$, C(Tubb4) = $1.68\,\mu M$, C(otherTubbs) = $3.48\,\mu M$. ΔG_{lat}(Tubb3) and ΔG_{lat}(Tubb4) were set to the before calculated values of $-3.67\,RT$ and $-3.79\,RT$, respectively. ΔG_{lat}(otherTubbs) was ranging from -3.4 to $-8\,RT$ in 0.2 steps. The program was executed 10 times and each data set was fitted with: velocity = $A - B/(\exp(C\,\Delta G_{lat} + D))$ (Figure 4.4 C). The dotted gray line indicates the *in vitro* velocity of MT plus ends containing tubulin purified from mouse brain tissue (brain, $0.008\,\mu m/s$) published in [Vemu et al., 2017]. The lateral energy value of the other beta-tubulin isotypes was calculated the same way as before for Tubb3 and Tubb4. The results are shown in figure 4.4 D. ΔG_{lat}(other Tubbs) ($-3.51\,RT$) was significantly higher than ΔG_{lat}(Tubb3) and ΔG_{lat}(Tubb4). With these parameters the velocities of brain MTs were simulated in a cell free environment for the control and the Tubb3 knockdown condition. The MT growth program was executed with the cell free parameters of $k_{on} = 6\,\mu M^{-1}s^{-1}$, $\Delta G_{long} = -7.2\,RT$, ΔG_{lat}(Tubb3) = $-3.67\,RT$, ΔG_{lat}(Tubb4) = $-3.79\,RT$ and ΔG_{lat}(otherTubbs) = $-3.51\,RT$. For the control condition concentrations were as before C(Tubb3) = $0.84\,\mu M$, C(Tubb4) = $1.68\,\mu M$, C(otherTubbs) = $3.48\,\mu M$. For the Tubb3 knockdown condition, individual dimer concentrations were determined using the experimental results from this study. Following Tubb3 knockdown, Tubb3 expression levels were reduced to 43 %, representing an average value of different experiments in this study and Tubb4 expression levels were increased to 133 %. Based on this, concentrations of individual Tubbs were calculated to C(Tubb3) = $0.36\,\mu M$, C(Tubb4) = $2.23\,\mu M$, C(otherTubbs) = $3.41\,\mu M$. For each condition 100 velocities were calculated and plotted in figure 4.4 E. The velocity of the control condition was significantly lower than the velocity of the knockdown condition, which matched the experimental results. But the experimental MT plus-end growth rates acquired by EB3 imaging were much faster than these calculated velocities. This originates from the fact that experiments were conducted in living cells containing co-factors as MTBPs and PTMs which influence MT growth. To account for these factors, model parameters and growth velocities were calculated also on the basis of a cellular environment.

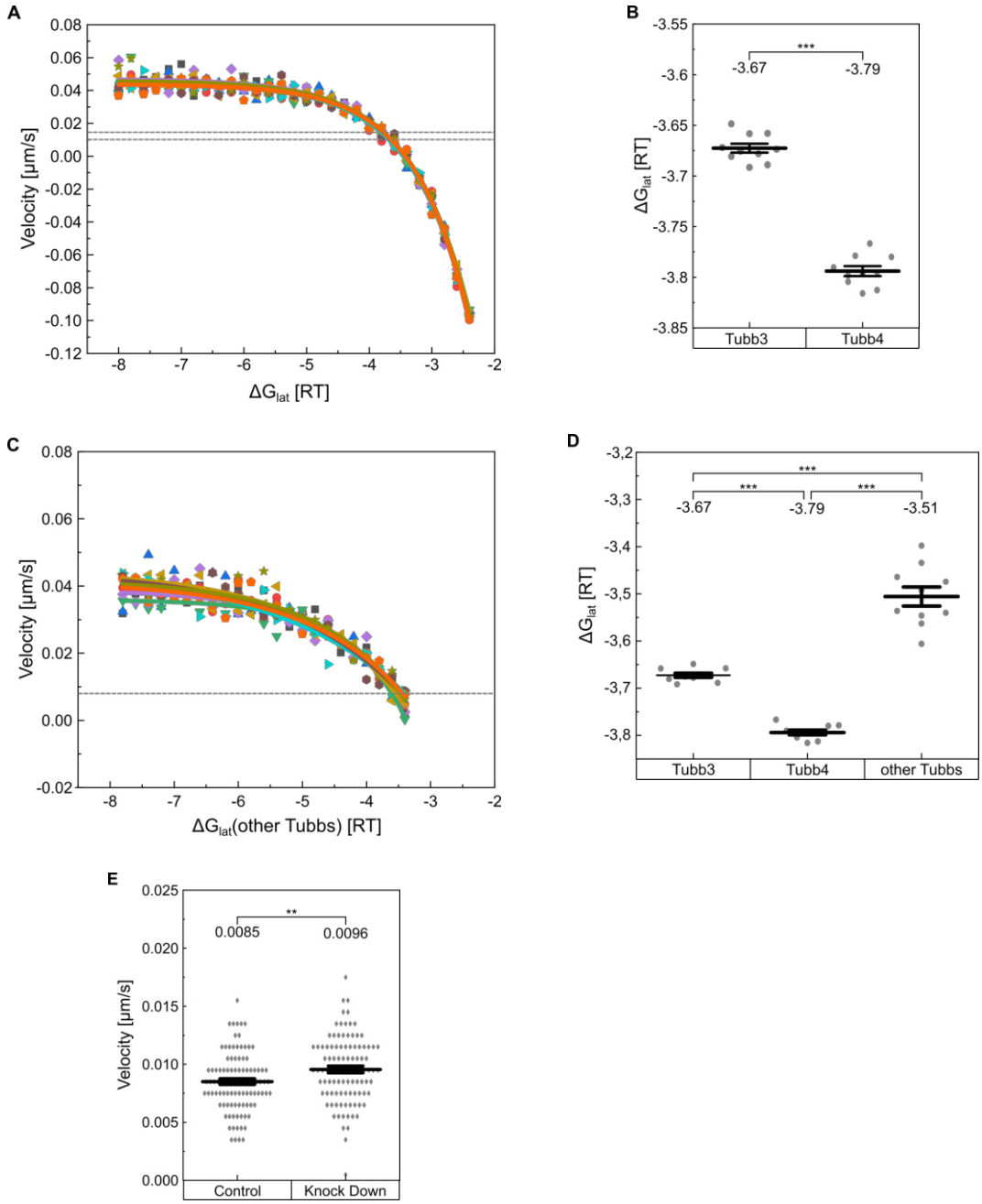

FIGURE 4.4. – Parameter determination on the basis of a cell free environment and velocity calculations. (A): The MT growth program was executed with the cell free parameters of $k_{on} = 6\,\mu M^{-1}s^{-1}$, $\Delta G_{long} = -7.2\,RT$, $C1 = C2 = C3 = 2\,\mu M$ and ΔG_{lat} ranging from -2.4 to $-8\,RT$ in 0.2 steps. The program was executed 10 times and each data set was fitted with: velocity $= A - B/(\exp(C\,\Delta G_{lat} + D))$. The dotted gray lines indicate the *in vitro* velocities of MT plus-ends containing tubulin purified from tsA201 cells (Tubb4, $0.0146\,\mu m/s$) or recombinant single-isotype human tubulin (Tubb3, $0.0102\,\mu m/s$) published in [Vemu et al., 2017]. **(B):** Lateral energy values were calculated with the fit parameter from (A) and the published *in vitro* velocities (Tubb3: $0.0102\,\mu m/s$, Tubb4: $0.0146\,\mu m/s$). ΔG_{lat}(Tubb3) ($-3.673 \pm 0.005\,RT$) and ΔG_{lat}(Tubb4) ($-3.794 \pm 0.005\,RT$) are significantly different *($p < 0.001$).*

Continued on next page

Figure 4.4. – Parameter determination on the basis of a cell free environment and velocity calculations. (C): The MT growth program was executed with the cell free parameters of $k_{on} = 6\,\mu M^{-1}s^{-1}$ and $\Delta G_{long} = -7.2\,RT$. The concentrations of the tubulin isotypes were set to the physiological values of $C1 = 0.84\,\mu M$, $C2 = 1.68\,\mu M$, and $C3 = 3.48\,\mu M$. ΔG_{lat}(Tubb3) and ΔG_{lat}(Tubb4) were set to the before calculated values of $-3.67\,RT$ and $-3.79\,RT$, respectively. ΔG_{lat}(otherTubbs) was ranging from -3.4 to $-8\,RT$ in 0.2 steps. The program was executed 10 times and each data set was fitted with: velocity $= A - B/(\exp(C\,\Delta G_{lat} + D))$. The dotted gray line indicates the *in vitro* velocity of MT plus-ends containing tubulin purified from mouse brain tissue (brain, $0.008\,\mu m/s$) published in [Vemu et al., 2017]. **(D):** The lateral energy value of the other Tubbs was calculated with the fit parameter from (A) and the published *in vitro* velocity (brain: $0.008\,\mu m/s$). ΔG_{lat}(other Tubbs) ($-3.51 \pm 0.02\,RT$) is significantly higher than ΔG_{lat}(Tubb3) and ΔG_{lat}(Tubb4) *($p < 0.001$).* **(E):** The MT growth program was executed with the cell free parameters of $k_{on} = 6\,\mu M^{-1}s^{-1}$, $\Delta G_{long} = -7.2\,kRT$, ΔG_{lat}(Tubb3) $= -3.67\,RT$, ΔG_{lat}(Tubb4) $= -3.79\,RT$ and ΔG_{lat}(otherTubbs) $= -3.51\,RT$. For the control condition concentrations were C(Tubb3) $= 0.84\,\mu M$, C(Tubb4) $= 1.68\,\mu M$, C(otherTubbs) $= 3.48\,\mu M$ and for the Tubb3 knockdown condition C(Tubb3) $= 0.36\,\mu M$, C(Tubb4) $= 2.23\,\mu M$, C(otherTubbs) $= 3.41\,\mu M$. For each condition 100 velocities were calculated. The velocity of the control condition ($0.0085 \pm 0.0003\,\mu m/s$) is significantly lower than the velocity of the knockdown condition ($0.0096 \pm 0.0003\,\mu m/s$) *($p < 0.006$).* Depicted: mean± SEM. For graphical representation of the distribution, data in (E) are binned with bin size $0.001\,\mu m/s$. Statistics: Student's t-test.

4.4. Velocity modeling with energy values determined on the basis of a cellular environment

For a cell free environment, it was assumed that longitudinal energy values did not differ between tubulin isotypes. In a cellular environment this assumption could not be maintained because MTBPs can influence lateral bonds between dimers as well as longitudinal bonds. So, parameters were expanded by ΔG_{long}(Tubb3), ΔG_{long}(Tubb4), and ΔG_{long}(other Tubbs). This made the energy determination more complex and necessitated the use of experimental results from the control and the Tubb3 knockdown condition. With the aim to predict longitudinal and lateral energies of Tubb3 and Tubb4 (ΔG_{long}(Tubb3), ΔG_{lat}(Tubb3), ΔG_{long}(Tubb4), ΔG_{lat}(Tubb4)), published *in vivo* values for the on-rate constant $k_{on} = 30\,\mu M^{-1}s^{-1}$ and the total tubulin concentration C(total) $= 7\,\mu M$ were adapted from a study by Castle and colleagues [Castle et al., 2017]. Longitudinal and lateral energy val-

ues for type 3 dimers (ΔG_{long}(other Tubbs) = $-7\,RT$ and ΔG_{lat}(other Tubbs) = $-4\,RT$) were estimated based on references [VanBuren et al., 2002, VanBuren et al., 2005, Gardner et al., 2011a, Castle et al., 2017]. As mentioned above, it was estimated that Tubb3 represents 14 %, Tubb4 28 % and the remaining Tubbs 58 % of soluble tubulin in the neuronal cytoplasm. Using these values and a tubulin concentration of 7 µM, individual tubulin dimer concentrations were calculated for control conditions (C(Tubb3) = $0.98\,\mu M$, C(Tubb4) = $1.96\,\mu M$ and C(otherTubbs) = $4.06\,\mu M$). As before for the knockdown condition, the Tubb3 concentration was set to 43 % of control levels and the Tubb4 concentration to 133 %. Based on this, molarities of individual Tubbs were calculated (C(Tubb3) = $0.42\,\mu M$, C(Tubb4) = $2.61\,\mu M$ and C(otherTubbs) = $3.97\,\mu M$). To determine longitudinal and lateral energies of Tubb3- and Tubb4-containing dimers, the program was executed with longitudinal energies ranging from -3 RT to -9 RT in 0.5 RT steps and lateral energies ranging from -1 RT to the respective longitudinal value. This procedure was justified, since longitudinal energies have to be smaller than lateral energies to polymerize stable MTs [Nogales et al., 1999]. For each energy parameter set (ΔG_{long}(Tubb3), ΔG_{lat}(Tubb3), ΔG_{long}(Tubb4), ΔG_{lat}(Tubb4)), MT growth velocities were calculated under control or Tubb3 knockdown conditions, respectively. Since plotting 5-dimensional data was not feasible, results were collected and processed using Excel (Microsoft), as described below. To display the results, energy values for Tubb3 and Tubb4 were plotted separately in contour graphs (Figure 4.5). To plot Tubb3 energies, Tubb4 energy values were fixed to final result values (ΔG_{long}(Tubb4) = $-7.5\,RT$ and ΔG_{lat}(Tubb4) = $-6\,RT$). Likewise, the same procedure was applied to plot Tubb4 energies (ΔG_{long}(Tubb3) = $-5\,RT$ and ΔG_{lat}(Tubb3) = $-3\,RT$). Gray contour lines were displayed to mark experimental velocities (control: $0.167\,\mu m/s$; Tubb3 knockdown: $0.201\,\mu m/s$).

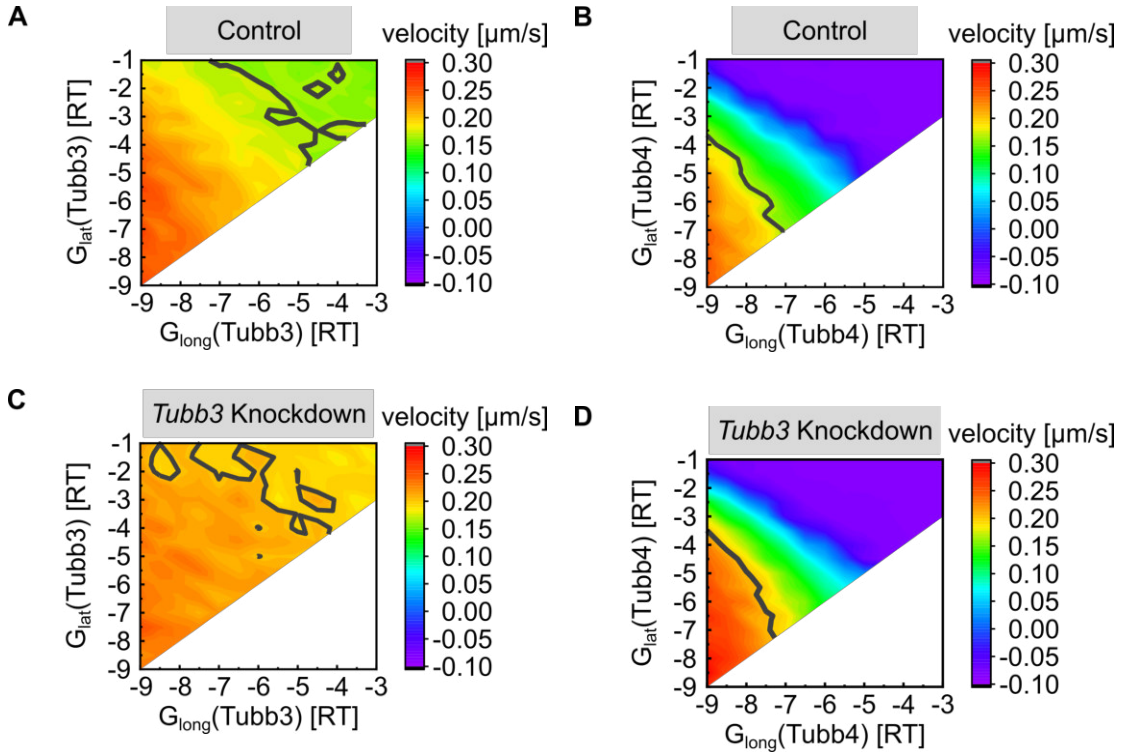

Figure 4.5. – Contour graphs of longitudinal and lateral energy values of Tubb3 and Tubb4 dimers. (A-D): Contour graphs of longitudinal and lateral energy values of Tubb3 and Tubb4 dimers. Velocity values are color coded as indicated to the right. Gray contour lines mark experimentally measured velocities (control: 0.167 µm/s; Tubb3 knockdown: 0.201 µm/s). In stable MTs, longitudinal energies are smaller than lateral energies [Nogales et al., 1999], so no velocity values were calculated for the parameter sets at the bottom right (white areas). **(A)** Tubb3 energy values under control conditions. **(B)** Tubb4 energy values under control conditions. **(C)** Tubb3 energy values under Tubb3 knockdown condition. **(D)** Tubb4 energy values under Tubb3 knockdown condition.

From the original results, parameter sets that generated velocities in the range of $0.167 \pm 0.006\,\mu m/s$ for the scrambled control and $0.201 \pm 0.008\,\mu m/s$ for the Tubb3 knockdown were selected. Parameter sets that coincided for control and knockdown conditions were filtered, resulting in 88 parameter sets that fulfilled the requirements. To narrow the number of possible parameters down, the program was executed again with the filtered parameter sets, this time calculating 100 velocities with control concentrations and 100 velocities with knockdown concentration. Because the standard error of mean velocity values produced from 100 calculations was $0.002\,\mu m/s$, energy parameter sets that generated velocities in the range of $0.167 \pm 0.002\,\mu m/s$ for the control condition and $0.201 \pm 0.002\,\mu m/s$ for the knockdown condition were selected. This procedure resulted in four parameter sets that fulfilled the requirements (Table 4.1).

Table 4.1. – Energy parameter settings after refinement.

ΔG_{long}(Tubb3) $[RT]$	ΔG_{lat}(Tubb3) $[RT]$	ΔG_{long}(Tubb4) $[RT]$	ΔG_{lat}(Tubb4) $[RT]$	velocity control $[\mu m/s]$	velocity knockdown $[\mu m/s]$
-5	-3	-7.5	-6	0.167	0.200
-4	-3	-7.5	-6.5	0.169	0.201
-7	-1	-5	-8	0.166	0.203
-6	-1.5	-6	-7.5	0.166	0.201

To refine the system, the program was executed with 400 runs, calculating MT growth velocities under control and Tubb3 knockdown conditions, respectively. This led to an accuracy in the standard error of the mean (SEM) in the range of 0.001 $\mu m/s$. Under these conditions, the parameter setting $\Delta G_{long}(\text{Tubb3}) = -5\,RT$, $\Delta G_{lat}(\text{Tubb3}) = -3\,RT$, $\Delta G_{long}(\text{Tubb4}) = -7.5\,RT$, and $\Delta G_{lat}(\text{Tubb4}) = -6\,RT$ mimicked experimental EB3 imaging results (Figure 4.6), leading to the complete parameter set shown in table 4.2.

Table 4.2. – Parameter values resulting from the parameter determination process.

Parameter	Control	Tubb3 knockdown
k_{on}	$30\,\mu M^{-1}s^{-1}$	
ΔG_{long}(other Tubbs)	$-7\,RT$	
ΔG_{lat}(other Tubbs)	$-4\,RT$	
ΔG_{long}(Tubb3)	$-5\,RT$	
ΔG_{lat}(Tubb3)	$-3\,RT$	
ΔG_{long}(Tubb4)	$-7.5\,RT$	
ΔG_{lat}(Tubb4)	$-6\,RT$	
C(Tubb3)	$0.98\,\mu M$	$0.42\,\mu M$
C(Tubb4)	$1.96\,\mu M$	$2.61\,\mu M$
C(rest)	$4.06\,\mu M$	$3.97\,\mu M$

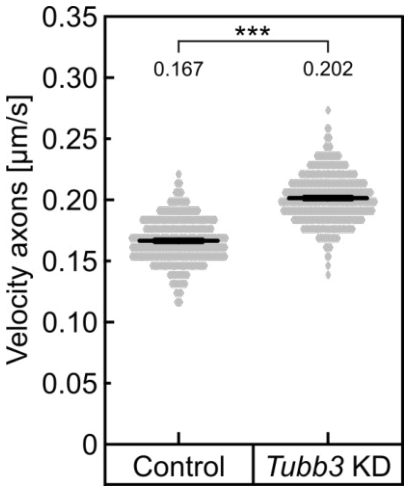

Figure 4.6. – Parameter determination on the basis of a cellular environment. The program was executed with control and Tubb3 knockdown conditions (400 runs, each) using the parameter values listed in table 4.2. Results equal the experimental data of EB3 MT growth experiments. The MT growth velocity of the Tubb3 knockdown condition ($0.202 \pm 0.001\,\mu m/s$) is significantly higher compared to the control ($0.167 \pm 0.001\,\mu m/s$) *($p<0.001$)*. Depicted: mean ± SEM. For graphical representation of the distribution, data are binned with bin size $0.0075\,\mu m/s$. Statistics: Student's t-test.

4.5. Modelling microtubule growth in silico

After the determination of suitable energy parameters simulating the EB3 experiment, these settings (Table 4.2) were used to assess the number of individual dimer types incorporated into growing MTs. The program was applied with 100 runs per condition and the actual numbers of dimer types were normalized to the total amount of dimers (Figure 4.7). Under control conditions, 4.3 % turned out to be Tubb3-containing dimers, 41.4 % Tubb4-containing dimers and 54.3 % dimers containing other Tubbs. In contrast, under conditions modelling Tubb3 knockdown, a 50 % reduction in Tubb3-containing dimers (2.1 %) was obtained, as expected. In parallel, Tubb4-containing dimers turned out to be increased to 48.3 %, while dimers-containing other Tubbs accounted for 49.7 %. These results confirmed former experimental data suggesting that reduced Tubb3 levels can be compensated by increased Tubb4.

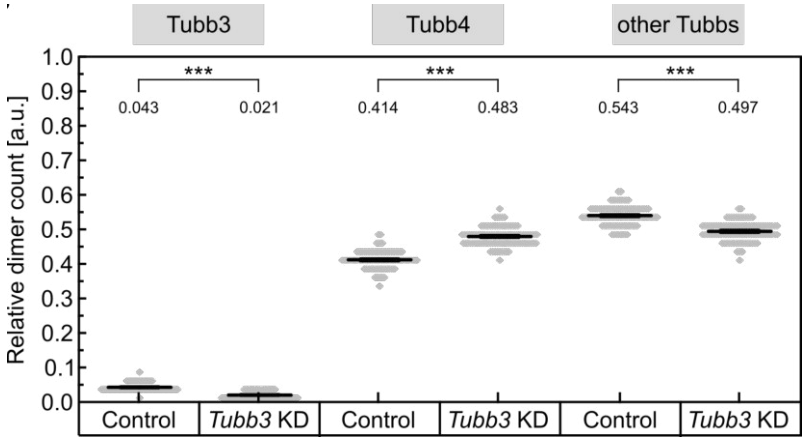

Figure 4.7. – Count of dimer types incorporated into the MT. The program was executed for control and Tubb3 knockdown conditions, as indicated (100 runs each). The number of Tubb3-containing dimers, Tubb4-containing and remaining Tubb isotype-containing dimers were counted and normalized by the total dimer count under control or Tubb3 KD conditions, respectively. The number of Tubb3 containing dimers after Tubb3 knockdown ($0.021 \pm 0.001\,a.u.$) is significantly lower compared to the control ($0.043 \pm 0.001\,a.u.$) *($p<0.001$)*. The number of Tubb4 containing dimers for the Tubb3 knockdown condition ($0.483 \pm 0.002\,a.u.$) is significantly increased compared to the control ($0.414 \pm 0.002\,a.u.$) *($p<0.001$)*. The number of other Tubbs containing dimers is significantly lower for the Tubb3 knockdown condition ($0.497 \pm 0.002\,a.u.$) compared to the control ($0.543 \pm 0.002\,a.u.$) *($p<0.001$)*. Depicted: mean ± SEM. For graphical representation of the distribution, data are binned with bin size $0.025\,a.u.$. Statistics: Student's t-test.

Next, the model was used to simulate MT growth velocities with varying combinations of Tubb expression levels (Figure 4.8). First, the opposite scenario to the Tubb3 knockdown was modeled (scenario I: high Tubb3, low Tubb4, equal other Tubbs). 400 runs of the program predicted that scenario I led to a significant decrease in the growth velocities of MTs, compared to control condition. Likewise, scenario II (equal Tubb3, low Tubb4, more other Tubbs, 400 runs) predicted a significant decrease in MT growth velocities. Consistent with this view, rising Tubb4 levels in turn were predicted to speed up MT growth in scenario III (equal Tubb3, high Tubb4, equal other Tubbs). Interestingly, this seemed to be different for Tubb3. While low Tubb3 sped up MT growth both experimentally and in the computational model (Figure 4.6), high Tubb3 was predicted to also accelerate MT growth (high Tubb3, equal Tubb4, equal other Tubbs). In summary, it can be concluded that the expression levels of individual tubulin isotypes translate into individual functions with respect to the dynamics of MTs. Due to the large number of alpha- and beta-tubulin isotypes and the many dimer combinations, computational modeling may be suitable to identify critical players.

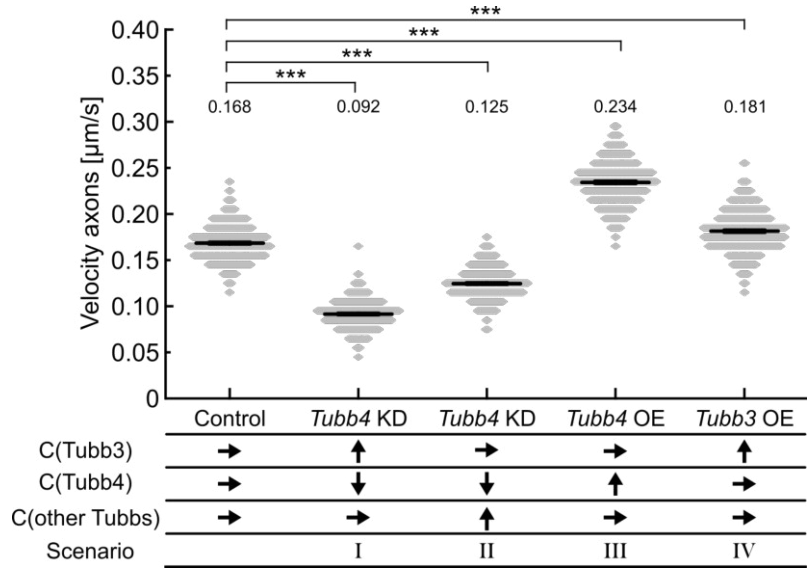

Figure 4.8. – Application of the computational model. The program was executed for different conditions, as indicated (400 runs, each), compared to the control condition. Scenario I was modeled with concentrations of $C(\text{Tubb3}) = 2.1\,\mu M$, $C(\text{Tubb4}) = 0.84\,\mu M$, and $C(\text{otherTubbs}) = 4.06\,\mu M$. Changes compared to control concentrations are indicated by black arrows. Scenario II was modeled with concentrations of $C(\text{Tubb3}) = 0.98\,\mu M$, $C(\text{Tubb4}) = 0.84\,\mu M$, and $C(\text{otherTubbs}) = 5.18\,\mu M$. Scenario III was modeled with concentrations of $C(\text{Tubb3}) = 0.98\,\mu M$, $C(\text{Tubb4}) = 2.64\,\mu M$, and $C(\text{otherTubbs}) = 4.06\,\mu M$. Scenario IV was modeled with concentrations of $C(\text{Tubb3}) = 2.1\,\mu M$, $C(\text{Tubb4}) = 1.96\,\mu M$, and $C(\text{otherTubbs}) = 4.06\,\mu M$. Altered parameters are indicated by vertical or horizontal black arrows, respectively. The velocity of scenario I ($0.092 \pm 0.001\,\mu m/s$) is significantly lower than the control value ($0.168 \pm 0.001\,\mu m/s$) *($p<0.001$)*. The MT growth velocity of scenario II ($0.125 \pm 0.001\ \ m/s$) is significantly lower than the control velocity *($p<0.001$)*. The velocities of scenario III ($0.234 \pm 0.002\,\mu m/s$) and scenario IV ($0.181 \pm 0.002\,\mu m/s$) are significantly higher than the control value *($p<0.001$)*. Depicted: mean ± SEM. For graphical representation, data are binned with bin size $0.010\,\mu m/s$. Statistics: One way ANOVA, followed by Dunnett's method for multiple comparisons against control.

4.6. Analysis of exogenous Tubb3 expression

To verify the prediction of the MT growth model for the plus-end growth rates in case of a Tubb3 overexpression, a DNA3-Tubb3 construct (chapter 2.3) was used to exogenously express Tubb3 in cells. Since fusion tags like GFP prevented the Tubb3 protein from being incorporated into MTs (Figure 4.9), a construct without any further tag was used. Human embryonic kidney (HEK) cells were transfected with this construct to proof that Tubb3 was expressed and incorporated into MTs. Figure 4.10 A shows a western blot of lysed HEK cells that were transfected with DNA3-

Tubb3 in comparison to un-transfected cells. It illustrates the Tubb3 expression after transfection, whereas un-transfected HEK cells barely expressed endogenous Tubb3. GAPDH was used as loading control. Confocal images of transfected HEK cells showed that Tubb3 was incorporated into MTs (Figure 4.10 B). DNA3-Tubb3 was co-transfected with GFP to identify transfected cells. 24 hours later cells were fixed and immuno-stained for Tubb3, panTuba and DAPI. The staining revealed Tubb3 expression in GFP positive cells and the filamentous structure proved the incorporation into MTs. Figure 4.11 shows the results of exogenous Tubb3 expression in neuronal hippocampal cultures. Cells were co-transfected with, either DNA3 and the control miRNA (Control), or DNA3 and the knockdown miRNA (Knockdown), or DNA3-Tubb3 and the control miRNA (Exogen. Tubb3). Panel B shows the enlargements of somata marked by pink boxes in A. As before, the Tubb3 signal intensity was measured inside the soma in DAPI negative regions marked by yellow boxes. The reduction of Tubb3 intensity after transfection with knockdown miRNA (50 %), compared to the control (set to one), worked reliably. But the signal intensity after exogenous Tubb3 expression (125 %) only showed a tendency towards higher intensity, not a significant difference, compared to the control.

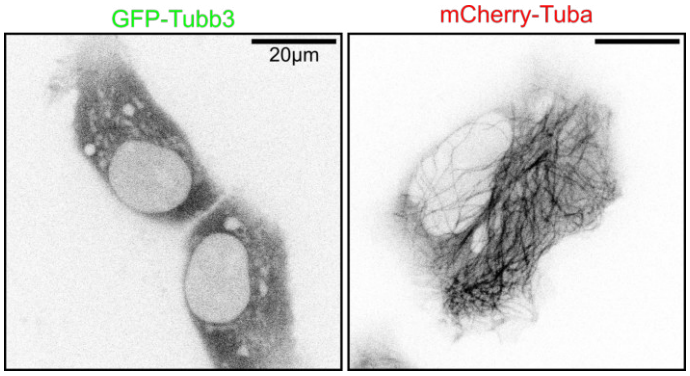

Figure 4.9. – Exogenous GFP-Tubb3 and mCherry-Tuba expression in HEK cells. Representative spinning disc confocal images of HEK cells transfected with GFP-Tubb3 or mCherry-Tuba. 24 hours later cells were imaged. The diffuse distribution of GFP-Tubb3 illustrates the expression of the construct, but it was not incorporated into MTs. As comparison mCherry-Tuba shows a clear filamentous structure and was therefore incorporated. Scale bar, 20 µm.

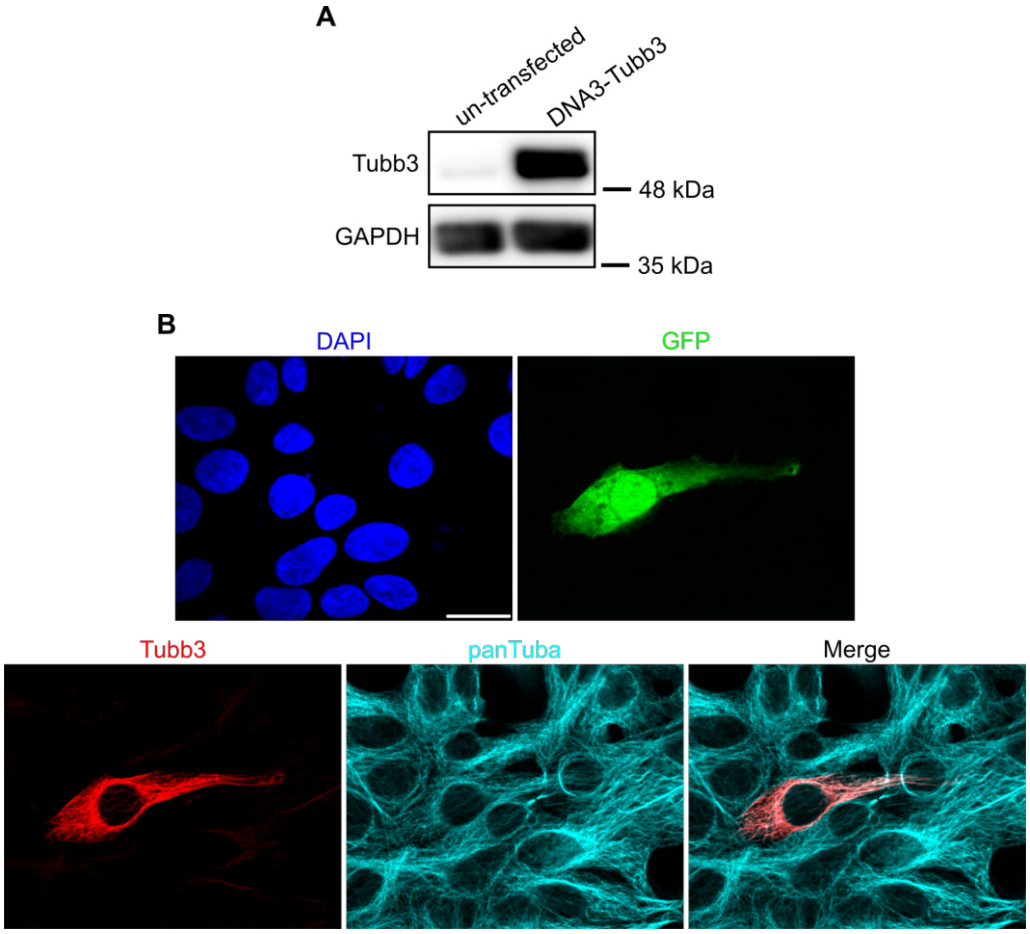

Figure 4.10. – Exogenous Tubb3 expression in HEK cells. (A): Western blot of lysed HEK cells that were un-transfected or transfected with DNA3-Tubb3. After transfection, expression of Tubb3 was detectable. GAPDH was used as loading control. **(B):** Representative confocal images of HEK cells co-transfected with DNA3-Tubb3 and GFP. 24 hours later cells were fixed and immuno-stained for Tubb3, panTuba and DAPI. Transfected cells could be identified via GFP expression. The staining illustrates the co-localization of Tubb3 with endogenous tubulin (panTuba) in filamentous structures and indicates thereby the incorporation of exogenous Tubb3 into MTs. Scale bar, 20 µm.

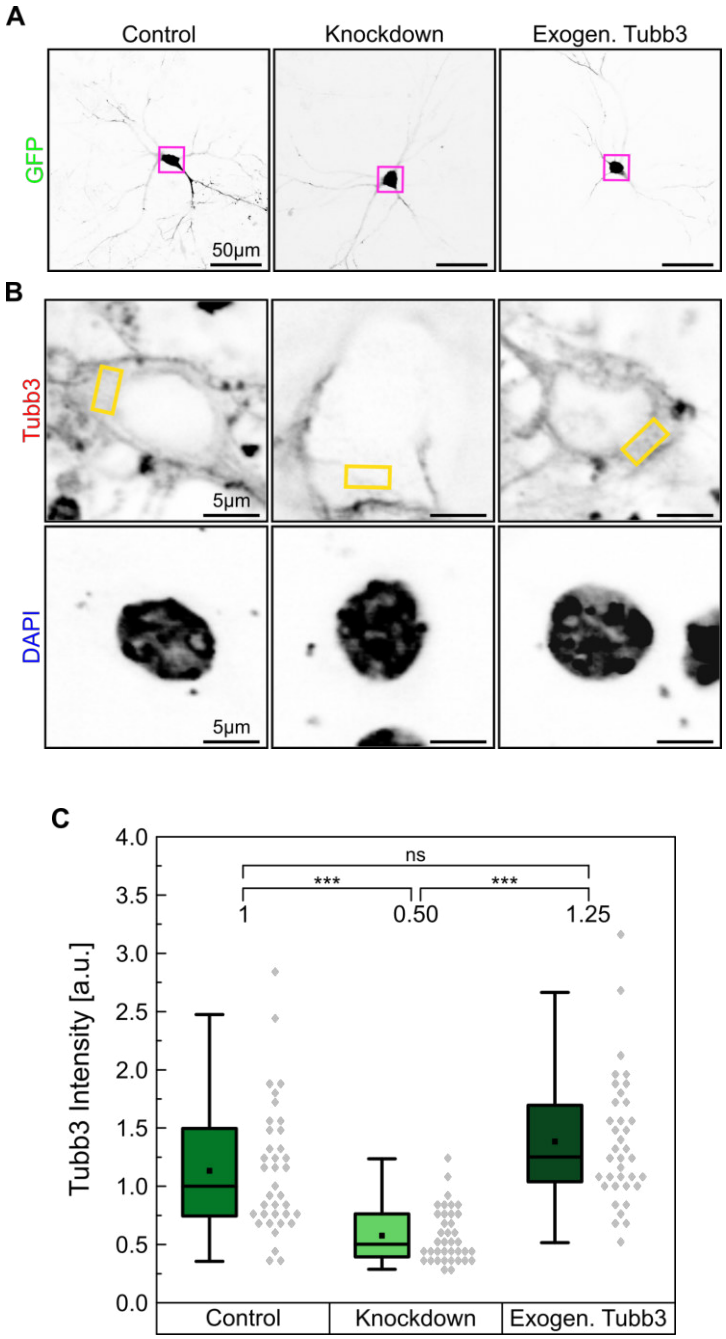

Figure 4.11. – Validation of exogenous Tubb3 expression in neurons. (A): Representative images of hippocampal neurons transfected with control miRNA, knockdown miRNA or control miRNA plus DNA3-Tubb3 (Exogen. Tubb3) at DIV 9 and fixed at DIV 12. Scale bar, 50 µm. **(B):** Enlargements of the cell somata in the pink boxes in (A). Tubb3 signal intensities were analyzed in DAPI negative regions as indicated by the yellow boxes. Scale bar, 5 µm.
Continued on next page

Figure 4.11. – Validation of exogenous Tubb3 expression in neurons. (C): Quantification of Tubb3 signal intensity measurements based on two independent experiments. Cells transfected with the knockdown miRNA show a significant decrease in Tubb3 signal intensity, 0.5 a.u. *($p < 0.001$)* compared to the control (set to 1). Cells transfected with the control miRNA plus DNA3-Tubb3 (Exogen. Tubb3) show no significant difference in Tubb3 signal intensity, 1.25 a.u. *($p = 0.135$)*, compared to the control. Knockdown and exogenous Tubb3 expression display a significant difference in Tubb3 signal intensity *($p < 0.001$)*. Depicted are median values with 25th and 75th percentile. Whiskers indicate the range within 1.5 IQR. Black squares show the mean value. Each data point represents one cell; control (n = 37), knockdown (n = 38), exogen. Tubb3 (n = 37). For graphical representation of the distribution, data are binned with bin size 0.08 [a.u.]. Statistics: Kruskal-Wallis one way ANOVA on ranks, followed by Dunn's Method for multiple comparisons of groups. Exogen.: exogenous.

Although the intensity measurements did not show a significant increase in Tubb3 intensity after Tubb3 overexpression compared to the control, EB3 measurements were executed to analyze the MT plus-end growth rate in axons. As in chapter 3.5 a MT end-binding protein 3 (EB3)-Tomato fusion construct was used to visualize the growing MT plus-end. To have the same comparison as for the modeling results, the experimental results of the Tubb3 knockdown in axons of chapter 3.5 are shown again. Neuronal hippocampal cultures were co-transfected with EB3-Tomato and the control miRNA, knockdown miRNA, or control miRNA plus DNA3-Tubb3 (Exogen. Tubb3) via Lipofectamine at DIV 9. Three days later they were imaged with a spinning disc confocal microscope. Figure 4.12 A shows representative frames of EB3 videos for the three conditions in axons and figure 4.12 B shows the tracing of representative comets over time. The videos were analyzed with ImageJ, by measuring the growth length, duration, and velocity. Shown are only the velocity results. Cells transfected with the knockdown miRNA showed a significant increase in EB3 velocity compared to the control. And, although transfection with the control miRNA and DNA3-Tubb3 (Exogen. Tubb3) showed no increase in Tubb3 signal intensity, these cells also revealed a significant increase in EB3 velocity compared to the control. This matches the prediction of the MT growth model for the overexpression with more Tubb3. Therefore, one can use the results of the model to conclude that after exogenous Tubb3 expression only the Tubb3 amount increases but other isotypes do not change.

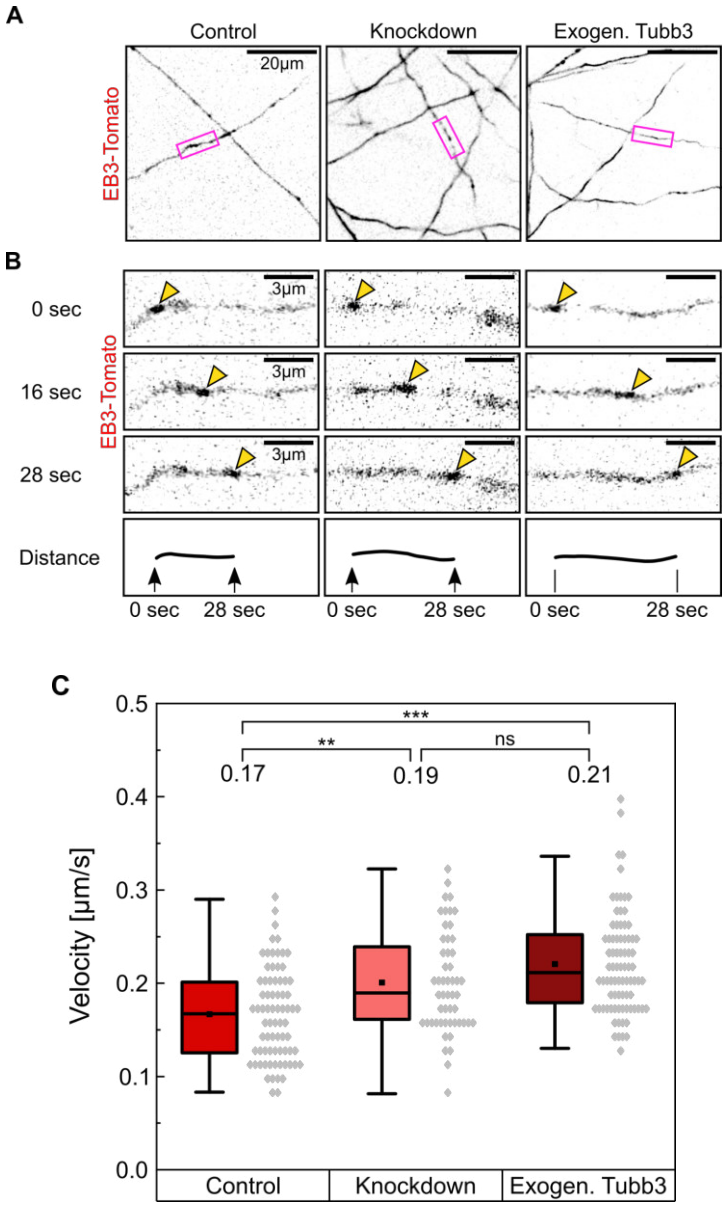

Figure 4.12. – Effects of altered Tubb3 expression levels on EB3 dynamics in axons. (A): Spinning disc confocal images of hippocampal neurons co-transfected with EB3-Tomato and the control miRNA, knockdown miRNA or control miRNA plus DNA3-Tubb3 (Exogen. Tubb3) at DIV 9. Live cell imaging was conducted at DIV 12 with videos taken over three minutes and a frame rate of one per second. Shown are representative frames of the EB3 videos. Scale bar, 20 µm. **(B):** Enlargements of axonal segments marked by the pink boxes in (A). EB3 comets were analyzed over time. Yellow arrowheads mark the movement of one representative comet for each condition over 28 seconds from top to bottom. The last panel visualizes the covered distance. Scale bar, 3 µm. **(C):** Cells transfected with Tubb3 knockdown miRNA show a significant increase in EB3 velocity (0.19 µm/s), compared to the control (0.17 µm/s), *($p = 0.004$)*. Cells transfected with the control miRNA plus DNA3-Tubb3 (Exogen. Tubb3) also show a significant increase in velocity (0.21 µm/s), compared to the control *($p < 0.001$)*. Knockdown and exogenous Tubb3 expression show no significant difference in EB3 velocity *($p = 0.134$)*.

Continued on next page

Figure 4.12. – Effects of altered Tubb3 expression levels on EB3 dynamics in axons. Depicted are median values with 25th and 75th percentile. Whiskers indicate the range within 1.5 IQR. Black squares show the mean value. Each data point represents one EB3 comet; control (n = 75), knockdown (n = 52), exogen. Tubb3 (n = 82). For graphical representation of the distribution, data are binned with bin size 0.015 µm/s. Statistics: Kruskal-Wallis one way ANOVA on ranks plus Dunn's method for multiple pairwise comparisons. Exogen.: exogenous.

5. Discussion

5.1. Induction of Chemical long-term potentiation in acute hippocampal slices

So far, little is known about the effect of synaptic stimulation on microtubule (MT) isotype composition. The induction of chemical long-term potentiation (cLTP) via tetraethylammonium (TEA) in acute hippocampal slices showed an increased Tubb3 signal intensity in SDS-Page analysis, which provided evidence that the tubulin isotype expression reacts to chemical stimuli and is most likely changed upon LTP induction. The question arose if the total tubulin concentration (all isotypes) was increased after stimulation, instead it could be shown by our lab that not all beta tubulin isotype signal intensities increase upon stimulation (data not shown). Kanterewicz et al. showed an increase in active ERK1 and ERK2 after TEA treatment of hippocampal slices, confirming the necessity of the ERK pathway in the induction of synaptic plasticity [Kanterewicz et al., 2000]. An increase in the activity of casein kinase II, which catalyzes the phosphorylation of a large number of protein substrates, was shown in hippocampal slices after cLTP induction via TEA by Charriaut-Marlangue et al. [Charriaut-Marlangue et al., 1991]. These results confirmed the ability of TEA induced cLTP to alter protein expression levels important for synaptic plasticity and other functions. The influence of cLTP on cytoskeletal elements was revealed by Briz et al. by showing an increased actin polymerization in rat hippocampal slices after TEA treatment [Briz et al., 2015]. The increase of distinct tubulin isotypes after cLTP induction coincides with the trend in literature and clarifies that the beta-tubulin isotype composition is influenced by synaptic stimulation. Therefore, it could act as a regulator in synaptic plasticity. To connect the beta-tubulin isotype expression with specific MT functions, effects of altered beta-tubulin isotype expression on MT growth and transport were analyzed via a Tubb3 knockdown.

5.2. Knockdown of Tubb3 via engineered microRNA and expression analysis of several beta-tubulin isotypes

It was shown that the downregulation of Tubb3 via microRNA (miRNA) led to a reduction of Tubb3 intensity measured in fluorescent confocal images. In secondary dendrites Tubb3 intensity was reduced to 67 % and in the cell soma to 45 %. The differences in knockdown efficiency in different cell compartments indicated that the distribution of tubulin isotypes throughout the cell was somehow regulated, possibly by transport processes. Timeline experiments showed that the knockdown reaches a plateau after three days incubation time, in accordance with the literature tubulin half-life value that lies between two and four days [Caron et al., 1985, Dutton and Barondes, 1969]. It was also shown that general beta-tubulin and alpha-tubulin intensity values did not change after Tubb3 downregulation, which gave rise to the question which other tubulin isotypes were affected by the downregulation of Tubb3. After an extensive tubulin antibody evaluation published in [Hausrat et al., 2020], the analysis of Tubb1, Tubb2, Tubb4 and Tubb5 intensity levels revealed an increase in Tubb4 intensity to 133 %, whereas other isotypes stayed unaltered. Why exactly Tubb4 was upregulated can only be speculated. The analysis of amino acid sequence homology of Tubb3 compared to Tubb2, Tubb4, and Tubb5 showed a similar similarity of 92 or 93 %, only Tubb1 was less similar (79 %) [Hausrat et al., 2020]. A hint towards Tubb4 could be, that Tubb4a was the only isotype which expression was upregulated from embryonic to adult tissue (see chapter 3.1.) Studies with Tubb3 knockout mice also showed equivalent total beta-tubulin levels compared to control mice. But the lack of Tubb3 protein was compensated by 10 to 20 % upregulation of most of the other beta-tubulin isotypes [Latremoliere et al., 2018] and not a specific one. A developing mouse with a complete lack of Tubb3 represents a different scenario than a neuronal cell in culture with a temporal controlled knockdown of Tubb3 to 45 % after neuritogenesis. However, both showed a compensation for the reduced Tubb3 protein expression levels, which indicated that cells can regulate their tubulin content very strictly. Alpha- and beta-tubulin build a dimer, which means that reducing beta-tubulin in general would lead to a decreased dimer amount and with that probably to reduced MT growth and disturbed MT function. Since MTs are very important components of cells it is logical that they react to a deficit in Tubb3 with a compensation, here with an increase in Tubb4. It was shown that in some cases isotypes were interchangeable and in others they were not [Luduena, 1993]. Therefore, the question arose if different amounts of beta-tubulin isotypes in

MTs have an effect on MT dynamics and their function as tracks in cargo transport. This will be discussed in the following paragraphs.

5.3. EB3 dynamics in neurons with reduced Tubb3 expression levels

MT plus-end growth rates were analyzed by visualizing them with an end-binding protein (EB3) - Tomato fusion construct. The reduction of Tubb3 revealed an increased MT growth length in dendrites, which led to an increased growth velocity of MT plus-ends. In axons, also an increased growth velocity of MT plus-ends with downregulated Tubb3 compared to control MTs could be shown. Literature displays varying results for the influence of tubulin isotypes on MT dynamics. Here, one must carefully pay attention to purification technique, source of tubulin and solution mixtures. For example, Vemu et al. showed that plus-end growth rates of MTs with decreased Tubb3 amount were higher, when mixed together with Tubb1 and Tubb4 [Vemu et al., 2017]. Whereas Panda et al. showed that plus-end growth of MTs with reduced Tubb3 amount was lower, when mixed with Tubb2 [Panda et al., 1994]. Both results were based on *in vitro* experiments with purified isotypes. The highest expressed isotype in brain is Tubb2 [Banerjee et al., 1992], therefore, the expected result of the cell culture experiments was reduced MT growth velocity after Tubb3 downregulation, however, the opposite was observed. But one must keep in mind, that the reduction of Tubb3 led to an increase in Tubb4, which might explain why the observed velocity in the experiments increased and not decreased. Also, the experiments were conducted in cell culture with all naturally available microtubule binding proteins (MTBPs) that influence MT assembly. Banerjee et al. showed that, with available tau or MAP2, bovine brain MTs depleted of Tubb3 assemble faster than regular MTs *in vitro* [Banerjee et al., 1990]. Also, MTs with available tau assembled faster than the ones with available MAP2. This showed that not only the isotype composition, but also the presence of distinct MTBPs influences MT growth velocity.

5.4. Kinesin-1 and N-Cadherin movement in neurons with reduced Tubb3 expression levels

After showing influences of tubulin isotype composition on MT growth the question arose if transport processes would also be affected. Motor movement and cargo transport were analyzed using KIF5C-Tomato and N-Cadherin-RFP fusion proteins. It was shown that the velocity of the motor movement and cargo transport in axons with reduced Tubb3 amount was increased compared to the control sample. So far, not much is known about the relationship between isotype composition and motor movement on MTs. Sirajuddin et al. showed a dependency between motor velocity and different isotypes with modified C-terminal tails and post-translational modifications (PTMs) in a single molecule assay [Sirajuddin et al., 2014]. Since kinesin-1 motors bind to beta-tubulin, changing the beta-tubulin isotype composition and with that the corresponding PTMs should be able to influence motor velocity. Another question was, why changes in axons were observed, but not in dendrites. It is known that MTPBs and PTMs distribution is different in axons and dendrites [Song and Brady, 2015]. That the changes in MT plus-end growth rate were differently strong in axons and dendrites gave evidence that isotype distribution from the soma to the neurites is also variable. As N-Cadherin is a cargo transported by kinesin motors [Lee, 2011], it was logical to observe the same effects for N-Cadherin transport as for KIF5C movement. Since N-Cadherin expression can influence the composition of synaptic molecules [Nikitczuk et al., 2014] and synaptic function [Pielarski et al., 2013], a N-Cadherin surface staining was conducted to analyze if the changed transport in axons upon Tubb3 downregulation had an influence on N-Cadherin distribution. This showed no differences in N-Cadherin surface intensity in axons with reduced Tubb3 amount compared to the control. Xu et al. could show that Tubb3 downregulation led to an increase in gamma-Aminobutyric acid-A receptor ($GABA_A$-R) surface expression [Xu et al., 2017], what indicated that Tubb3 expression can influence the surface expression of a synaptic protein. Also a conditional KIF5A knockout led to reduced cell surface expression of $GABA_A$-Rs [Nakajima et al., 2012], connecting a kinesin-1 motor protein to surface expression. This discrepancy might originate in the fact that $GABA_A$-Rs are mainly existent in dendrites and the cell body, whereas here the surface intensity in axons was analyzed. Additionally, N-Cadherin is a transmembrane protein, not a receptor and might therefore underlie different regulating pathways.

5.5. Microtubule growth modeling

Beside experiments, mathematical models and simulations became an important tool to analyze biological research hypotheses. Since tubulin isotype composition in MTs was the main variable analyzed in this thesis, a biophysical model of MT growth in dependence of beta-tubulin isotype composition, was included. To determine a parameter set for computing MT growth velocities, the model was designed using the acquired EB3 plus-end growth rates. In literature [VanBuren et al., 2002, Gardner et al., 2011b, Castle et al., 2017] models were based on a single dimer type as building blocks for MTs, here a model with three individual dimer types was introduced. From a sequence analysis of beta-tubulin isotypes it became clear, that the parameter which differs between isotypes in a cell free environment should be the lateral binding energy. Lateral energy values of Tubb3, Tubb4, and other Tubbs containing dimers calculated with *in vitro* velocities published by Vemu et al. [Vemu et al., 2017], were significantly different. Applying changes in tubulin concentrations representing the Tubb3 knockdown scenario led to an increase in MT growth velocity. This increase matched the *in vitro* results published by Vemu et al. and the cellular EB3 experiments conducted in this thesis. Since velocities in a cellular environment were much higher than *in vitro*, the model had to be adjusted accordingly. The difference between a cell free and a cellular environment were the PTMs and MTBPs that affect MT assembly. A first test (data not shown) revealed that variations in the lateral energies of the isotypes did not suffice to generate velocity differences between control and knockdown, as seen experimentally. This made sense since it was very likely for MTBPs to affect lateral bonds between dimers as well as longitudinal bonds. This expanded the modeling complexity from three (ΔG_{lat}(Tubb3), ΔG_{lat}(Tubb4), ΔG_{lat}(other Tubbs)) unknown energy parameters to six (ΔG_{long}(Tubb3), ΔG_{lat}(Tubb3), ΔG_{long}(Tubb4), ΔG_{lat}(Tubb4), ΔG_{long}(other Tubbs), ΔG_{lat}(other Tubbs)). Computational limits made it necessary to reduce the complexity of this problem which was accounted for by adapting values for ΔG_{long}(other Tubbs) and ΔG_{lat}(other Tubbs) from literature ([Castle et al., 2017]). This assumption reduced the strength of the resulting absolute energy values, but the relative comparison of energy values was not compromised by that. Meaning, that the absolute energy values for Tubb3 and Tubb4 containing dimers depended on the chosen starting energy values for the other Tubbs. This was a limitation of the cellular parameter determination but made it possible to calculate final velocity results. To gain the final parameter set listed in table 4.2, experimental EB3 growth velocities of the control and the Tubb3 knockdown condition were used, so the parameters reflected the energies needed to produce the

experimentally observed change in velocity upon Tubb3 knockdown. Tubb3 energies were weaker than the ones of Tubb4 or the other Tubbs, whereas the energy values of Tubb4 were stronger than the ones of the other Tubbs. This suggested that changes in Tubb4 concentration have a stronger effect on MT growth than Tubb3 changes. Compared to lateral energy values obtained from a cell free environment where differences in lateral energies were rather small ($\Delta G_{lat}(\text{Tubb3}) = -3.67\,RT$, $\Delta G_{lat}(\text{Tubb4}) = -3.79\,RT$) the differences between energies obtained in a cellular environment were much bigger ($\Delta G_{long}(\text{Tubb3}) = -5\,RT$, $\Delta G_{lat}(\text{Tubb3}) = -3\,RT$, $\Delta G_{long}(\text{Tubb4}) = -7.5\,RT$, and $\Delta G_{lat}(\text{Tubb4}) = -6\,RT$). This finding indicated that, although pure tubulin isotypes led to different MT growth velocities, PTMs and MTBPs influence tubulin isotypes in a varying manner, play a vital role in MT assembly and must be included in the model to gain correct results. Subsequently the model was used to make predictions about future experiments which are discussed in the following paragraphs.

A first application of the MT growth model, the count of dimer types inside the MT showed that the dimer types were not incorporated in the same percentage as they were available. The Tubb3 concentrations fed into the program were 14 % for the control and 6 % for the knockdown condition. The dimer count gave 4.3 % of the incorporated dimers being Tubb3 for the control and 2.1 % for the knockdown. Both were reduced by the same ratio upon Tubb3 knockdown, but the total percentage of Tubb3 inside the MT was lower than in the solution. This possibly originated from the relatively weak energy bonds of Tubb3, which increased the unbinding of Tubb3 containing dimers from the growing MT tip. In contrast to that, Tubb4 was much more incorporated into MTs than expected. The Tubb4 concentration given to the program were 28 % for the control and 37.3 % for the Tubb3 knockdown condition. The dimer count of incorporated dimers gave 41.4 % for the control and 48.3 % for the knockdown, which can be explained by the strong energy bonds of Tubb4 containing dimers. The number of incorporated Tubb4 dimers also increased upon Tubb3 downregulation, but not as much as in the solution. In total, these results suggest that tubulin dimers do not have to be incorporated into the MT in the same ratio as they are available in the cytosolic solution, probably due to their different characteristics and interactions with MTBPs.

The second application was to model MT growth velocities for different tubulin isotype concentration scenarios. The overexpression of Tubb3 (scenario IV) showed an increased velocity compared to the control. This was unexpected since the downregulation of Tubb3 also led to an increased velocity compared to the control. But again, one must keep in mind that with the downregulation of Tubb3 came an

upregulation of Tubb4. This suggested that the increased velocity of the Tubb3 knockdown originated from an upregulated Tubb4 expression. And indeed, modeling of the MT plus-end growth velocity with increased Tubb3 and decreased Tubb4 concentrations (scenario I) showed a lower velocity than the control. This indicates that changes in Tubb4 concentration have a stronger effect on the MT growth velocity than changes in Tubb3 concentration. But nonetheless, a Tubb3 increase alone also changed the MT growth velocity. Since this was a simplified MT model using assumptions for some biological parameters, it was possible that modeled results might deviate from the biological truth. Nonetheless they give important insights into processes at the protein level, raise new questions and point to the right experimental direction. The more information about isotype compositions in cellular MTs becomes available the more precise biophysical models can become and with that the predictions they make.

5.6. Exogenous Tubb3 expression

To verify the prediction of the MT growth model about the MT plus-end growth velocity for Tubb3 overexpression, neurons were transfected with a Tubb3 construct. Unfortunately, Tubb3 intensity measurements only showed a tendency to higher intensities after Tubb3 overexpression compared to the control, not a significant difference. But EB3 experiments showed an increased growth velocity after transfection with the Tubb3 construct compared to the control in axons and dendrites, which indicated a change in the MT composition. This confirmed the prediction of the MT growth model of increased growth velocity in the case that Tubb3 was overexpressed, and other isotype concentrations were unaltered. This makes it very likely that the Tubb3 overexpression did work but is somehow not detectable by the intensity measurement method. In general, an increased Tubb3 expression was associated with increased malignancy in several tumor tissues. Also in neuronal tumors the increased expression of Tubb3 was associated with tumor maturational phenomena [Katsetos et al., 2003]. Overexpression of beta-tubulin in yeast cells was lethal and led to an arrested cell cycle, increased chromosome loss, lack of MTs and beta-tubulin accumulation into a novel structure [Burke et al., 1989]. These findings indicate that overexpressed Tubb3, or general beta-tubulin, might be harmful to cells, especially by influencing the cell cycle. However, differentiated neurons do not proliferate and might not be affected by this. In neurons a correlation between Tubb3 expression and epileptic seizures was revealed by finding increased Tubb3 levels in rat hippocampi of two chronic epilepsy models [Xu et al., 2017]. Tubb3

knockdown had an anti-epileptic effect, whereas Tubb3 overexpression contributed to seizure development. Epileptic seizures result from an imbalance of excitatory and inhibitory neurotransmission, with the latter mainly being mediated via $GABA_A$-Rs. Xu et al. also showed that Tubb3 overexpression led to reduced cell surface expression of the $GABA_A$-R and decreased mean amplitude of the miniature inhibitory postsynaptic potentials (mIPSCs), which means that Tubb3 may be involved in trafficking of $GABA_A$-Rs from the intracellular pool to the surface [Xu et al., 2017]. This matches the earlier finding, that Tubb3 downregulation influences N-Cadherin transport. It also leads back to the very first experiment where it was shown that chemical induced LTP led to increased Tubb3 levels in acute hippocampal slices. Although Hanse et al. showed that TEA induced LTP is not related to alterations in $GABA_A$ergic inhibition [Hanse and Gustafsson, 1994], it is an indicator how Tubb3 expression could influence synaptic plasticity.

6. Conclusion and Outlook

This study showed a connection between synaptic stimulation, tubulin isotype composition and MT function. The topics of tubulin isotypes, their expression patterns, and functions are expanding and especially interesting in neuroscience because of the high variety of tubulin isotypes in brain tissue. Also, it was shown that mutations in tubulin genes which result in disease phenotypes can lead to reduced Tubb3 expression [Tischfield et al., 2010]. The results of this thesis confirm that the expression pattern of beta-tubulin isotypes influences MT growth, motor driven transport, and that cells respond to external interference in isotype expression. This points to an elaborate regulatory system which is important for the cell to maintain functional efficiency and adapt to external stimuli in the process of synaptic plasticity. Additional to the experimental results the MT growth model gave insights into the effects of isotype concentrations on MT growth and demonstrated the power and usefulness of mathematical simulations to understand biological systems.

This study also demonstrated the complexity of MT research. Although the role of tubulin isotypes is more and more understood, a lot of open questions remain. Next steps could be to generate additional knockdown and overexpression constructs to analyze the functionality of other tubulin isotypes. Also, activity related questions are of interest, for example if cLTP could induce a MT growth or motor transport phenotype in cell culture. Together with the SDS-Page analysis of isotype expression after cLTP induction, this could shed a light on isotype functionality. Additionally to cell culture experiments, mouse behavior experiments could be conducted with following isotype composition analysis of the hippocampus region. Furthermore, super resolution microscopy analysis would be an efficient tool to investigate isotype patterns within the MTs. In general, future research should provide more detailed information about isotype distribution and functionality since this is clearly an important regulator of cellular processes.

In addition to extended experiments the MT model holds a great potential for expansions. At the moment it is focused on MT growth and velocity. MT shrinkage could be included by determining the energy difference between GTP-tubulin (growth)

and GDP-tubulin (shrinkage) states. Switching between these two states (catastrophy, rescue) could be characterized by a hydrolysis constant. Also, more or different isotypes could be included to model further growth scenarios. When all natural isotypes and MT dynamic parameters are included, the model could be used to discuss phenotypes related to tubulin isotype expression, like cortical development in mice [Saillour et al., 2014], rat epileptic tissue [Xu et al., 2017], and cancer cell lines [Katsetos et al., 2003]. An important step forward would also be to improve the parameter determination process for the cellular environment by either reducing the needed computation time or by finding another calculation method.

Altogether, the combination of biological experiments with physical models is becoming an increasingly important approach to investigate complex scientific questions.

7. Acknowledgments

With this project a special time for me is ending, during which I learned a lot, faced challenges, and have grown professionally and personally. Many thanks to my supervisor Matthias Kneussel for welcoming me to his group and enabling me to perform my PhD thesis in his lab. Also, I thank my second supervisor Michael Rübhausen for making this interdisciplinary work possible and to sustain my connection to physics. A big thank you goes to Torben Hausrat for the day-to-day supervision, teaching of new techniques, always providing help and advice when needed, listening to Christmas music all December long, and giving me the perseverance to finish this project. A special thank you goes to Petra Breiden for all the answered questions, the inspiring scientific and personal conversations, and spreading her good mood. Also, I want to thank all members of the Molecular Neurogenetics Institute, especially Mona Roesler, Franco Lombino, Kira Brune, Lea Cochius, and Pascal Segura for their companionship, constant support, and all the fun times inside and out of the lab. Also, Yvonne Pechmann and Edda Thies for their technical support. All of you made the institute feel like a second home. I also want to thank the PhD students of the FOR2419 research group. With that I also thank the DFG for funding my project.

Additionally, I want to thank my personal friends for enriching my life during this often challenging time. Especially Jessica Suhr, Andrea Wilke, Mischa Lohse, and Filip Podjaski gave me strength and moral support. Also, the girls from Caecilia and the members of the herd made this a special time. Finally, I want to thank my family for always supporting me. Especially my parents, who supported my studies, not only financially, but always gave me the freedom and strength to pursue my goals. Finally, I thank my brother and sister-in-law for the special understanding during the writing phase, you gave me a lot of motivation.

List of Figures

List of Tables

List of abbreviations

Tubb3	Mouse tubulin beta 3 class III gene
BSA	Bovine serum albumin
cAMP	Cyclic adenosine monophosphate
CFU	Colony forming units
CMV	Cytomegalovirus
CREB	cAMP response element binding protein
DMEM	Dulbecco's modified eagle medium
DNA	Deoxyribonucleic acid
dNTP	Deoxyribonucleotide triphosphate
E. coli	Escherichia coli
ECL	Enhanced chemiluminescence
EDTA	Ethylenediaminetetraacetic acid
GFP	Green fluorescent protein
HBSS	Hank's balanced salt solution
HBS	HEPES buffered saline
HEPES	4-(2-hydroxyethyl)-1-piperazineethanesulfonic acid
kDa	Kilodalton
LB	Lysogeny broth
miRNA	Micro RNA
mRNA	Messenger RNA
MT	Microtubule
No	Number
PBS	Phosphate-buffered saline
PCR	Polymerase chain reaction
pre-miRNA	Precursor miRNA
pri-miRNA	Primary miRNA
PVDF	Polyvinyldene difluoride
RISC	RNA-induced silencing complex
RNA	Ribonucleic acid
RT	Room temperature

SDS-PAGE	Sodium dodecyl sulfate-polyacrylamide gel electrophoresis
SDS	Sodium dodecyl sulfate
SEM	Standard error of the mean
shRNA	Short hairpin RNA
SOC	Super optimal broth with catabolite repression
TBST	Tris-buffered saline Tween 20
TEMED	Tetramethylethylenediamine
Tubb3	Mouse tubulin beta 3 class III protein

Bibliography

[Akhmanova and Hammer, 2010] Akhmanova, A. and Hammer, J. A. (2010). Linking molecular motors to membrane cargo. *Current Opinion in Cell Biology*, 22(4):479–487.

[Akhmanova and Hoogenraad, 2015] Akhmanova, A. and Hoogenraad, C. C. (2015). Microtubule minus-end-targeting proteins. *Current Biology*, 25(4):R162–R171.

[Akhmanova and Steinmetz, 2015] Akhmanova, A. and Steinmetz, M. O. (2015). Control of microtubule organization and dynamics: Two ends in the limelight. *Nature Reviews Molecular Cell Biology*, 16(12):711–726.

[Alushin et al., 2014] Alushin, G. M., Lander, G. C., Kellogg, E. H., Zhang, R., Baker, D., and Nogales, E. (2014). High-Resolution microtubule structures reveal the structural transitions in $\alpha\beta$-tubulin upon GTP hydrolysis. *Cell*, 157(5):1117–1129.

[Audebert et al., 1994] Audebert, S., Koulakoff, a., Berwald-Netter, Y., Gros, F., Denoulet, P., and Eddé, B. (1994). Developmental regulation of polyglutamylated alpha- and beta-tubulin in mouse brain neurons. *Journal of cell science*, 107 (Pt 8:2313–22.

[Aumeier et al., 2016] Aumeier, C., Schaedel, L., Gaillard, J., John, K., Blanchoin, L., and Théry, M. (2016). Self-repair promotes microtubule rescue. *Nature Cell Biology*, 18(10):1054–1064.

[Banerjee et al., 1990] Banerjee, A., Roach, M. C., Trcka, P., and Luduena, R. F. (1990). Increased microtubule assembly in bovine brain tubulin lacking the type III isotype of β-tubulin. *Journal of Biological Chemistry*, 265(3):1794–1799.

[Banerjee et al., 1992] Banerjee, A., Roach, M. C., Trcka, P., and Luduena, R. F. (1992). Preparation of a monoclonal antibody specific for the class IV isotype of β-tubulin. Purification and assembly of $\alpha\beta$(II), $\alpha\beta$(III), and $\alpha\beta$(IV) tubulin dimers from bovine brain. *Journal of Biological Chemistry*, 267(8):5625–5630.

[Barlan and Gelfand, 2017] Barlan, K. and Gelfand, V. I. (2017). Microtubule-based transport and the distribution, tethering, and organization of organelles. *Cold Spring Harbor Perspectives in Biology*, 9(5):1–12.

[Bear et al., 2016] Bear, M. F., Connors, B. W., and Paradiso, M. A. (2016). *Neuroscience: Exploring the Brain*.

[Bonnet et al., 2001] Bonnet, C., Boucher, D., Lazereg, S., Pedrotti, B., Islam, K., Denoulet, P., and Larcher, J. C. (2001). Differential Binding Regulation of Microtubule-associated Proteins MAP1A, MAP1B, and MAP2 by Tubulin Polyglutamylation. *Journal of Biological Chemistry*, 276(16):12839–12848.

[Boucher et al., 1994] Boucher, D., Larcher, J. C., Gros, F., and Denoulet, P. (1994). Polyglutamylation of tubulin as a progressive regulator of in vitro interactions between the microtubule-associated protein tau and tubulin. *Biochemistry*, 33(41):12471–12477.

[Breuss et al., 2012] Breuss, M., Heng, J. I. T., Poirier, K., Tian, G., Jaglin, X. H., Qu, Z., Braun, A., Gstrein, T., Ngo, L., Haas, M., Bahi-Buisson, N., Moutard, M. L., Passemard, S., Verloes, A., Gressens, P., Xie, Y., Robson, K. J., Rani, D. S., Thangaraj, K., Clausen, T., Chelly, J., Cowan, N. J., and Keays, D. A. (2012). Mutations in the β-Tubulin Gene TUBB5 Cause Microcephaly with Structural Brain Abnormalities. *Cell Reports*, 2(6):1554–1562.

[Briz et al., 2015] Briz, V., Zhu, G., Wang, Y., Liu, Y., Avetisyan, M., Bi, X., and Baudry, M. (2015). Activity-dependent rapid local RhoA synthesis is required for hippocampal synaptic plasticity. *Journal of Neuroscience*, 35(5):2269–2282.

[Brouhard and Rice, 2018] Brouhard, G. J. and Rice, L. M. (2018). Microtubule dynamics: An interplay of biochemistry and mechanics. *Nature Reviews Molecular Cell Biology*, 19(7):451–463.

[Buey et al., 2006] Buey, R. M., Fernando Díaz, J., and Andreu, J. M. (2006). The nucleotide switch of tubulin and microtubule assembly: A polymerization-driven structural change. *Biochemistry*, 45(19):5933–5938.

[Burgoyne et al., 1988] Burgoyne, R. D., Cambray-Deakin, M. A., Lewis, S. A., Sarkar, S., and Cowan, N. J. (1988). Differential distribution of beta-tubulin isotypes in cerebellum. *The EMBO Journal*, 7(8):2311–2319.

[Burke et al., 1989] Burke, D., Gasdaska, P., and Hartwell, L. (1989). Dominant effects of tubulin overexpression in Saccharomyces cerevisiae. *Molecular and Cellular Biology*, 9(3):1049–1059.

[Caron et al., 1985] Caron, J. M., Jones, A. L., and Kirschner, M. W. (1985). Autoregulation of tubulin synthesis in hepatocytes and fibroblasts. *Journal of Cell Biology*, 101(5):1763–1772.

[Cassimeris, 2002] Cassimeris, L. (2002). The oncoprotein 18/stathmin family of microtubule destabilizers. *Current Opinion in Cell Biology*, 14(1):18–24.

[Castle et al., 2017] Castle, B. T., McCubbin, S., Prahl, L. S., Bernens, J. N., Sept, D., and Odde, D. J. (2017). Mechanisms of kinetic stabilization by the drugs paclitaxel and vinblastine. *Molecular Biology of the Cell*, 28(9):1238–1257.

[Chaaban and Brouhard, 2017] Chaaban, S. and Brouhard, G. J. (2017). A microtubule bestiary: Structural diversity in tubulin polymers. *Molecular Biology of the Cell*, 28(22):2924–2931.

[Chakraborti et al., 2016] Chakraborti, S., Natarajan, K., Curiel, J., Janke, C., and Liu, J. (2016). The emerging role of the tubulin code: From the tubulin molecule to neuronal function and disease. *Cytoskeleton*, 73(10):521–550.

[Charriaut-Marlangue et al., 1991] Charriaut-Marlangue, C., Otani, S., Creuzet, C., Ben-Ari, Y., and Loeb, J. (1991). Rapid activation of hippocampal casein kinase II during long-term potentiation. *Proceedings of the National Academy of Sciences of the United States of America*, 88(22):10232–10236.

[Chrétien et al., 1995] Chrétien, D., Fuller, S. D., and Karsenti, E. (1995). Structure of growing microtubule ends: Two-dimensional sheets close into tubes at variable rates. *Journal of Cell Biology*, 129(5):1311–1328.

[Chrétien and Wade, 1991] Chrétien, D. and Wade, R. H. (1991). New data on the microtubule surface lattice. *Biology of the Cell*, 71:161–174.

[Chu et al., 2011] Chu, C. W., Hou, F., Zhang, J., Phu, L., Loktev, A. V., Kirkpatrick, D. S., Jackson, P. K., Zhao, Y., and Zou, H. (2011). A novel acetylation of β-tubulin by San modulates microtubule polymerization via down-regulating tubulin incorporation. *Molecular Biology of the Cell*, 22(4):448–456.

[Dallai et al., 2005] Dallai, R., Lupetti, P., Osella, G., and Afzelius, B. A. (2005). Giant sperm cells with accessory macrotubules in a neuropteran insect. *Tissue and Cell*, 37(5):359–366.

[Dehmelt and Halpain, 2005] Dehmelt, L. and Halpain, S. (2005). The MAP2/Tau family of microtubule-associated proteins. *Genome Biology*, 6(1):1–10.

[Deng et al., 2017] Deng, X., Fink, G., Bharat, T. A., He, S., Kureisaite-Ciziene, D., and Löwe, J. (2017). Four-stranded mini microtubules formed by Prosthecobacter BtubAB show dynamic instability. *Proceedings of the National Academy of Sciences of the United States of America*, 114(29):E5950–E5958.

[Dent et al., 2011] Dent, E. W., Merriam, E. B., and Hu, X. (2011). The dynamic cytoskeleton: Backbone of dendritic spine plasticity. *Current Opinion in Neurobiology*, 21(1):175–181.

[Dixit et al., 2008] Dixit, R., Ross, J. L., Goldman, Y. E., and Holzbaur, E. L. F. (2008). Differential Regulation of Dynein and Kinesin Motor Proteins by Tau. *Science*, 319(5866):1086–1089.

[Dompierre et al., 2007] Dompierre, J. P., Godin, J. D., Charrin, B. C., Cordelieres, F. P., King, S. J., Humbert, S., and Saudou, F. (2007). Histone Deacetylase 6 Inhibition Compensates for the Transport Deficit in Huntington's Disease by Increasing Tubulin Acetylation. *Journal of Neuroscience*, 27(13):3571–3583.

[Dunn et al., 2008] Dunn, S., Morisson, E. E., Liverpool, T. B., Molina-París, C., Cross, R. A., Alonso, M. C., and Peckham, M. (2008). Differential trafficking of Kif5c on tyrosinated and detyrosinated microtubules in live cells. *Journal of Cell Science*, 121(7):1085–1095.

[Dutton and Barondes, 1969] Dutton, G. R. and Barondes, S. (1969). Microtubular Protein: Synthesis and Metabolism in Developing Brain. *Science*, 166:1637–1638.

[Gadadhar et al., 2017] Gadadhar, S., Bodakuntla, S., Natarajan, K., and Janke, C. (2017). The tubulin code at a glance. *Journal of Cell Science*, 130(8):1347–1353.

[Gardner et al., 2011a] Gardner, M. K., Charlebois, B. D., Jánosi, I. M., Howard, J., Hunt, A. J., and Odde, D. J. (2011a). Rapid microtubule self-assembly kinetics with supplements. *Cell*, 146(4):582–592.

[Gardner et al., 2011b] Gardner, M. K., Charlebois, B. D., J??nosi, I. M., Howard, J., Hunt, A. J., and Odde, D. J. (2011b). Rapid microtubule self-assembly kinetics. *Cell*, 146(4):582–592.

[Gennerich and Vale, 2009] Gennerich, A. and Vale, R. D. (2009). Walking the walk: how kinesin and dynein coordinate their steps. *Current Opinion in Cell Biology*, 21(1):59–67.

[Goodson and Jonasson, 2018] Goodson, H. V. and Jonasson, E. M. (2018). Microtubules and Microtubule-Associated Proteins. *Cold Spring Harbor perspectives in biology*.

[Guesdon et al., 2016] Guesdon, A., Bazile, F., Buey, R. M., Mohan, R., Monier, S., García, R. R., Angevin, M., Heichette, C., Wieneke, R., Tampé, R., Duchesne, L., Akhmanova, A., Steinmetz, M. O., and Chrétien, D. (2016). EB1 interacts with outwardly curved and straight regions of the microtubule lattice. *Nature Cell Biology*, 18(10):1102–1108.

[Guo et al., 2010] Guo, J., Walss-Bass, C., and Ludueña, R. F. (2010). The beta isotypes of tubulin in neuronal differentiation. *Cytoskeleton*, 67(7):431–441.

[Gupta et al., 2013] Gupta, K. K., Li, C., Duan, A., Alberico, E. O., Kim, O. V., Alber, M. S., and Goodson, H. V. (2013). Mechanism for the catastrophe-promoting activity of the microtubule destabilizer Op18/stathmin. *Proceedings of the National Academy of Sciences of the United States of America*, 110(51):20449–20454.

[Hanse and Gustafsson, 1994] Hanse, E. and Gustafsson, B. (1994). TEA elicits two distinct potentiations of synaptic transmission in the CA1 region of the hippocampal slice. *Journal of Neuroscience*, 14(8):5028–5034.

[Hausrat et al., 2020] Hausrat, T. J., Radwitz, J., Lombino, F. L., Breiden, P., and Kneussel, M. (2020). Alpha- and beta-tubulin isotypes are differentially expressed during brain development. *Developmental Neurobiology*, (October 2019):1–18.

[Heisler et al., 2014] Heisler, F. F., Lee, H. K., Gromova, K. V., Pechmann, Y., Schurek, B., Ruschkies, L., Schroeder, M., Schweizer, M., and Kneussel, M. (2014). GRIP1 interlinks N-cadherin and AMPA receptors at vesicles to promote combined cargo transport into dendrites. *Proceedings of the National Academy of Sciences of the United States of America*, 111(13):5030–5.

[Hemmat et al., 2019] Hemmat, M., Castle, B. T., Sachs, J. N., and Odde, D. J. (2019). Multiscale Computational Modeling of Tubulin-Tubulin Lateral Interaction. *Biophysical Journal*, 117(7):1234–1249.

[Hirano and Takeichi, 2012] Hirano, S. and Takeichi, M. (2012). Cadherins in Brain Morphogenesis and Wiring. *Physiological Reviews*, 92(2):597–634.

[Hirokawa et al., 2010] Hirokawa, N., Niwa, S., and Tanaka, Y. (2010). Molecular motors in neurons: Transport mechanisms and roles in brain function, development, and disease. *Neuron*, 68(4):610–638.

[Hirokawa and Takemura, 2005] Hirokawa, N. and Takemura, R. (2005). Molecular motors and mechanisms of directional transport in neurons. *Nature reviews. Neuroscience*, 6(3):201–214.

[Hoogenraad and Akhmanova, 2010] Hoogenraad, C. C. and Akhmanova, A. (2010). Dendritic spine plasticity: New regulatory roles of dynamic microtubules. *Neuroscientist*, 16(6):650–661.

[Howes et al., 2017] Howes, S. C., Geyer, E. A., LaFrance, B., Zhang, R., Kellogg, E. H., Westermann, S., Rice, L. M., and Nogales, E. (2017). Structural differences between yeast and mammalian microtubules revealed by cryo-EM. *Journal of Cell Biology*, 216(9):2669–2677.

[Janke and Magiera, 2020] Janke, C. and Magiera, M. M. (2020). The tubulin code and its role in controlling microtubule properties and functions. *Nature Reviews Molecular Cell Biology*.

[Jánosi et al., 1998] Jánosi, I. M., Chrétien, D., and Flyvbjerg, H. (1998). Modeling elastic properties of microtubule tips and walls. *European Biophysics Journal*, 27(5):501–513.

[Kanterewicz et al., 2000] Kanterewicz, B. I., Urban, N. N., McMahon, D. B., Norman, E. D., Giffen, L. J., Favata, M. F., Scherle, P. A., Trzăskos, J. M., Barrionuevo, G., and Klann, E. (2000). The extracellular signal-regulated kinase cascade is required for NMDA receptor-independent LTP in area CA1 but not area CA3 of the hippocampus. *Journal of Neuroscience*, 20(9):3057–3066.

[Katsetos et al., 2003] Katsetos, C. D., Legido, A., Perentes, E., and Mörk, S. J. (2003). Class III beta-tubulin isotype: a key cytoskeletal protein at the crossroads of developmental neurobiology and tumor neuropathology. *Journal of child neurology*, 18(12):851–66; discussion 867.

[Kneussel et al., 2014] Kneussel, M., Triller, A., and Choquet, D. (2014). SnapShot: Receptor dynamics at plastic synapses. *Cell*, 157(7):1738–1738.e1.

[Kollman et al., 2011] Kollman, J. M., Merdes, A., Mourey, L., and Agard, D. A. (2011). Microtubule nucleation by γ-tubulin complexes. *Nature Reviews Molecular Cell Biology*, 12(11):709–721.

[Komarova et al., 2002] Komarova, Y. A., Vorobjev, I. A., and Borisy, G. G. (2002). Life cycle of MTs : persistent growth in the cell interior , asymmetric transition frequencies and effects of the cell boundary. *Journal of Cell Science*, 115:3527–3539.

[Korte and Schmitz, 2016] Korte, M. and Schmitz, D. (2016). Cellular and System Biology of Memory: Timing, Molecules, and Beyond. *Physiological reviews*, 96(2):647–93.

[Kubo et al., 2010] Kubo, T., aki Yanagisawa, H., Yagi, T., Hirono, M., and Kamiya, R. (2010). Tubulin Polyglutamylation Regulates Axonemal Motility by Modulating Activities of Inner-Arm Dyneins. *Current Biology*, 20(5):441–445.

[Kumar et al., 2015] Kumar, S. C., Gadewal, N., and Mohammed, S. M. (2015). Seminal role of deletion of amino acid residues in H1-S2 and S-loop regions in eukaryotic β-tubulin investigated from docking and dynamics perspective. *Journal of Theoretical Biology*, 378:79–88.

[Lacroix et al., 2010] Lacroix, B., Van Dijk, J., Gold, N. D., Guizetti, J., Aldrian-Herrada, G., Rogowski, K., Gerlich, D. W., and Janke, C. (2010). Tubulin polyglutamylation stimulates spastin-mediated microtubule severing. *Journal of Cell Biology*, 189(6):945–954.

[Lanzanò et al., 2017] Lanzanò, L., Scipioni, L., Bona, M. D., Bianchini, P., Bizzarri, R., Cardarelli, F., Diaspro, A., and Vicidomini, G. (2017). Measurement of nanoscale three-dimensional diffusion in the interior of living cells by STED-FCS. *Nature Communications*, 8(65):1–9.

[Latremoliere et al., 2018] Latremoliere, A., Cheng, L., DeLisle, M., Wu, C., Chew, S., Hutchinson, E. B., Sheridan, A., Alexandre, C., Latremoliere, F., Sheu, S. H., Golidy, S., Omura, T., Huebner, E. A., Fan, Y., Whitman, M. C., Nguyen, E., Hermawan, C., Pierpaoli, C., Tischfield, M. A., Woolf, C. J., and Engle, E. C. (2018). Neuronal-Specific TUBB3 Is Not Required for Normal Neuronal Function but Is Essential for Timely Axon Regeneration. *Cell Reports*, 24(7):1865–1879.e9.

[Lee, 2011] Lee, H. K. (2011). Analysis of the adaptor proteins , gephyrin and GRIP1 , in KIF5-driven neuronal transport in Mus musculus, (Linnaeus, 1758). *Universität Hamburg*, Dissertati.

[Lee et al., 1990] Lee, M. K., Tuttle, J. B., Rebhun, L. I., Cleveland, D. W., and Frankfurter, a. (1990). The expression and posttranslational modification of a neuron-specific beta-tubulin isotype during chick embryogenesis. *Cell motility and the cytoskeleton*, 17:118–132.

[Lee Sweeney and Holzbaur, 2018] Lee Sweeney, H. and Holzbaur, E. L. (2018). Motor proteins. *Cold Spring Harbor Perspectives in Biology*, 10(5):1–17.

[Lopes et al., 2020] Lopes, A. T., Hausrat, T. J., Heisler, F. F., Gromova, K. V., Lombino, F. L., Fischer, T., Ruschkies, L., Breiden, P., Thies, E., Hermans-Borgmeyer, I., Schweizer, M., Schwarz, J. R., Lohr, C., and Kneussel, M. (2020). Spastin depletion increases tubulin polyglutamylation and impairs kinesin- mediated neuronal transport , leading to working and associative memory deficits. *PLOS Biology*.

[Luduena, 1993] Luduena, R. F. (1993). Are Tubulin Isotypes Functionally Significant. *Molecular Biology of the Cell*, 4(May):445–457.

[Maas et al., 2009] Maas, C., Belgardt, D., Lee, H. K., Heisler, F. F., Lappe-Siefke, C., Magiera, M. M., van Dijk, J., Hausrat, T. J., Janke, C., and Kneussel, M. (2009). Synaptic activation modifies microtubules underlying transport of postsynaptic cargo. *Proceedings of the National Academy of Sciences of the United States of America*, 106(21):8731–6.

[Magiera et al., 2018] Magiera, M. M., Bodakuntla, S., Žiak, J., Lacomme, S., Marques Sousa, P., Leboucher, S., Hausrat, T. J., Bosc, C., Andrieux, A., Kneussel, M., Landry, M., Calas, A., Balastik, M., and Janke, C. (2018). Excessive tubulin polyglutamylation causes neurodegeneration and perturbs neuronal transport. *The EMBO Journal*, 37(23):e100440.

[Mandelkow et al., 1991] Mandelkow, E. M., Mandelkow, E., and Milligan, R. A. (1991). Microtubule dynamics and microtubule caps: A time-resolved cryo-electron microscopy study. *Journal of Cell Biology*, 114(5):977–991.

[Marcos et al., 2009] Marcos, S., Moreau, J., Backer, S., Job, D., Andrieux, A., and Bloch-Gallego, E. (2009). Tubulin tyrosination is required for the proper organization and pathfinding of the growth cone. *PLoS ONE*, 4(4).

[Maurer et al., 2011] Maurer, S. P., Bieling, P., Cope, J., Hoenger, A., and Surrey, T. (2011). GTPγS microtubules mimic the growing microtubule end structure recognized by end-binding proteins (EBs). *Proceedings of the National Academy of Sciences of the United States of America*, 108(10):3988–3993.

[Maurer et al., 2014] Maurer, S. P., Cade, N. I., Bohner, G., Gustafsson, N., Boutant, E., and Surrey, T. (2014). EB1 accelerates two conformational transitions important for microtubule maturation and dynamics. *Current Biology*, 24(4):372–384.

[McKenney et al., 2016] McKenney, R. J., Huynh, W., Vale, R. D., and Sirajuddin, M. (2016). Tyrosination of α-tubulin controls the initiation of processive

dynein–dynactin motility. *The EMBO Journal*, 35(11):1175–1185.

[Meurer-Grob et al., 2001] Meurer-Grob, P., Kasparian, J., and Wade, R. H. (2001). Microtubule Structure at Improved Resolution †. 40:23.

[Minoura, 2017] Minoura, I. (2017). Towards an understanding of the isotype-specific functions of tubulin in neurons: Technical advances in tubulin expression and purification. *Neuroscience Research*, 122:1–8.

[Mitchison and Kirschner, 1984] Mitchison, T. and Kirschner, M. (1984). Dynamic instability of microtubule growth. *Nature*, 312:23–29.

[Nakagawa et al., 2000] Nakagawa, H., Koyama, K., Murata, Y., Morito, M., Akiyama, T., and Nakamura, Y. (2000). EB3, a novel member of the EB1 family preferentially expressed in the central nervous system, binds to a CNS-specific APC homologue. *Oncogene*, 19(2):210–216.

[Nakajima et al., 2012] Nakajima, K., Yin, X., Takei, Y., Seog, D. H., Homma, N., and Hirokawa, N. (2012). Molecular Motor KIF5A Is Essential for GABAA Receptor Transport, and KIF5A Deletion Causes Epilepsy. *Neuron*, 76(5):945–961.

[Nawrotek et al., 2011] Nawrotek, A., Knossow, M., and Gigant, B. (2011). The determinants that Govern microtubule assembly from the atomic structure of GTP-tubulin. *Journal of Molecular Biology*, 412(1):35–42.

[Nikitczuk et al., 2014] Nikitczuk, J. S., Patil, S. B., Matikainen-ankney, B. A., Scarpa, J., Shapiro, M. L., Benson, D. L., and Huntley, G. W. (2014). N-Cadherin Regulates Molecular Organization of Excitatory and Inhibitory Synaptic Circuits in Adult Hippocampus In Vivo. 24:943–962.

[Nogales et al., 1999] Nogales, E., Whittaker, M., Milligan, R. A., Downing, K. H., and Berkeley, L. (1999). High-Resolution Model of the Microtubule. 96:79–88.

[Pamula et al., 2016] Pamula, M. C., Ti, S. C., and Kapoor, T. M. (2016). The structured core of human β tubulin confers isotype-specific polymerization properties. *Journal of Cell Biology*, 213(4):425–433.

[Panda et al., 1994] Panda, D., Miller, H. P., Banerjee, a., Ludueña, R. F., and Wilson, L. (1994). Microtubule dynamics in vitro are regulated by the tubulin isotype composition. *Proceedings of the National Academy of Sciences of the United States of America*, 91(24):11358–11362.

[Peris et al., 2006] Peris, L., Thery, M., Fauré, J., Saoudi, Y., Lafanechère, L., Chilton, J. K., Gordon-Weeks, P., Galjart, N., Bornens, M., Wordeman, L., Wehland, J., Andrieux, A., and Job, D. (2006). Tubulin tyrosination is a major factor affecting the recruitment of CAP-Gly proteins at microtubule plus ends. *Journal of Cell Biology*, 174(6):839–849.

[Peris et al., 2009] Peris, L., Wagenbach, M., Lafanechère, L., Brocard, J., Moore, A. T., Kozielski, F., Job, D., Wordeman, L., and Andrieux, A. (2009). Motor-dependent microtubule disassembly driven by tubulin tyrosination. *Journal of Cell Biology*, 185(7):1159–1166.

[Pielarski et al., 2013] Pielarski, K. N., van Stegen, B., Andreyeva, A., Nieweg, K., Jüngling, K., Redies, C., and Gottmann, K. (2013). Asymmetric N-Cadherin Expression Results in Synapse Dysfunction, Synapse Elimination, and Axon Retraction in Cultured Mouse Neurons. *PLoS ONE*, 8(1):1–13.

[Pierson et al., 1978] Pierson, G. B., Burton, P. R., and Himes, R. H. (1978). Alterations in Number of Protofilaments in Microtubules assembled in Vitro. *The Journal of cell biology*, 76:223–228.

[Poirier et al., 2010] Poirier, K., Saillour, Y., Bahi-Buisson, N., Jaglin, X. H., Fallet-Bianco, C., Nabbout, R., Castelnau-Ptakhine, L., Roubertie, A., Attie-Bitach, T., Desguerre, I., Genevieve, D., Barnerias, C., Keren, B., Lebrun, N., Boddaert, N., Encha-Razavi, F., and Chelly, J. (2010). Mutations in the neuronal β-tubulin subunit TUBB3 result in malformation of cortical development and neuronal migration defects. *Human Molecular Genetics*, 19(22):4462–4473.

[Randazzo et al., 2019] Randazzo, D., Khalique, U., Belanto, J. J., Kenea, A., Talsness, D. M., Olthoff, J. T., Tran, M. D., Zaal, K. J., Pak, K., Pinal-Fernandez, I., Mammen, A. L., Sackett, D., Ervasti, J. M., and Ralston, E. (2019). Persistent upregulation of the β-tubulin tubb6, linked to muscle regeneration, is a source of microtubule disorganization in dystrophic muscle. *Human Molecular Genetics*, 28(7):1117–1135.

[Renthal et al., 1993] Renthal, R., Schneider, B. G., Miller, M. M., and Ludueña, R. F. (1993). β IV is the major β-tubulin isotype in bovine cilia. *Cell Motility and the Cytoskeleton*, 25(1):19–29.

[Rice et al., 2008] Rice, L. M., Montabana, E. A., and Agard, D. A. (2008). The lattice as allosteric effector: Structural studies of $\alpha\beta$- and γ-tubulin clarify the

role of GTP in microtubule assembly. *Proceedings of the National Academy of Sciences of the United States of America*, 105(14):5378–5383.

[Rogowski et al., 2010] Rogowski, K., van Dijk, J., Magiera, M. M., Bosc, C., Deloulme, J. C., Bosson, A., Peris, L., Gold, N. D., Lacroix, B., Grau, M. B., Bec, N., Larroque, C., Desagher, S., Holzer, M., Andrieux, A., Moutin, M. J., and Janke, C. (2010). A family of protein-deglutamylating enzymes associated with neurodegeneration. *Cell*, 143(4):564–578.

[Roll-Mecak and McNally, 2010] Roll-Mecak, A. and McNally, F. J. (2010). Microtubule-severing enzymes. *Current Opinion in Cell Biology*, 22(1):96–103.

[Saillour et al., 2014] Saillour, Y., Broix, L., Bruel-Jungerman, E., Lebrun, N., Muraca, G., Rucci, J., Poirier, K., Belvindrah, R., Francis, F., and Chelly, J. (2014). Beta tubulin isoforms are not interchangeable for rescuing impaired radial migration due to Tubb3 knockdown. *Human Molecular Genetics*, 23(6):1516–1526.

[Schaedel et al., 2015] Schaedel, L., John, K., Gaillard, J., Nachury, M. V., Blanchoin, L., and Thery, M. (2015). Microtubules self-repair in response to mechanical stress. *Nature Materials*, 14(11):1156–1163.

[Schwer et al., 2001] Schwer, H. D., Lecine, P., Tiwari, S., Italiano, J. E., Hartwig, J. H., and Shivdasani, R. A. (2001). A lineage-restricted and divergent β-tubulin isoform is essential for the biogenesis, structure and function of blood platelets. *Current Biology*, 11(8):579–586.

[Seetapun et al., 2012] Seetapun, D., Castle, B. T., McIntyre, A. J., Tran, P. T., and Odde, D. J. (2012). Estimating the Microtubule GTP Cap Size In Vivo. *Current Biology*, 23(1):1–7.

[Sirajuddin et al., 2014] Sirajuddin, M., Rice, L. M., and Vale, R. D. (2014). Regulation of microtubule motors by tubulin isotypes and post-translational modifications. *Nature cell biology*, 16(4):335–44.

[Song and Brady, 2015] Song, Y. and Brady, S. T. (2015). Post-translational modifications of tubulin: Pathways to functional diversity of microtubules. *Trends in Cell Biology*, 25(3):125–136.

[Song et al., 2013] Song, Y., Kirkpatrick, L. L., Schilling, A. B., Helseth, D. L., Chabot, N., Keillor, J. W., Johnson, G. V. W., and Brady, S. T. (2013). Transglutaminase and Polyamination of Tubulin: Posttranslational Modification for Stabilizing Axonal Microtubules. *Neuron*, 78(1):109–123.

[Stepanova et al., 2003] Stepanova, T., Slemmer, J., Hoogenraad, C. C., Lansbergen, G., Dortland, B., De Zeeuw, C. I., Grosveld, F., van Cappellen, G., Akhmanova, A., and Galjart, N. (2003). Visualization of microtubule growth in cultured neurons via the use of EB3-GFP (end-binding protein 3-green fluorescent protein). *The Journal of Neuroscience*, 23(7):2655–2664.

[Ti et al., 2018] Ti, S. C., Alushin, G. M., and Kapoor, T. M. (2018). Human β-Tubulin Isotypes Can Regulate Microtubule Protofilament Number and Stability. *Developmental Cell*, 47(2):175–190.e5.

[Tischfield et al., 2010] Tischfield, M. A., Baris, H. N., Wu, C., Rudolph, G., Van Maldergem, L., He, W., and Others, A. (2010). Human TUBB3 Mutations Perturb Microtubule Dynamics, Kinesin Interactions, and Axon Guidance. *Cell*, 140(1):74–87.

[Topalidou et al., 2012] Topalidou, I., Keller, C., Kalebic, N., Nguyen, K. C., Somhegyi, H., Politi, K. A., Heppenstall, P., Hall, D. H., and Chalfie, M. (2012). Genetically separable functions of the MEC-17 tubulin acetyltransferase affect microtubule organization. *Current Biology*, 22(12):1057–1065.

[Valentine and Gilbert, 2007] Valentine, M. T. and Gilbert, S. P. (2007). To step or not to step? How biochemistry and mechanics influence processivity in Kinesin and Eg5. *Current Opinion in Cell Biology*, 19(1):75–81.

[VanBuren et al., 2005] VanBuren, V., Cassimeris, L., and Odde, D. J. (2005). Mechanochemical Model of Microtubule Structure and Self-Assembly Kinetics. *Biophysical Journal*, 89(5):2911–2926.

[VanBuren et al., 2002] VanBuren, V., Odde, D. J., and Cassimeris, L. (2002). Estimates of lateral and longitudinal bond energies within the microtubule lattice. *Proceedings of the National Academy of Sciences*, 99(9):6035–6040.

[Vemu et al., 2017] Vemu, A., Atherton, J., Spector, J. O., Moores, C. A., and Roll-Mecak, A. (2017). Tubulin isoform composition tunes microtubule dynamics. *Molecular Biology of the Cell*, pages mbc.E17–02–0124.

[Verhey and Hammond, 2009] Verhey, K. J. and Hammond, J. W. (2009). Traffic control: Regulation of kinesin motors. *Nature Reviews Molecular Cell Biology*, 10(11):765–777.

[Verhey et al., 2011] Verhey, K. J., Kaul, N., and Soppina, V. (2011). Kinesin assembly and movement in cells. *Annual Review of Biophysics*, 40(1):267–288.

[Von Loeffelholz et al., 2017] Von Loeffelholz, O., Venables, N. A., Drummond, D. R., Katsuki, M., Cross, R., and Moores, C. A. (2017). Nucleotide- and Mal3-dependent changes in fission yeast microtubules suggest a structural plasticity view of dynamics. *Nature Communications*, 8(1):1–13.

[Walczak et al., 2013] Walczak, C. E., Gayek, S., and Ohi, R. (2013). Microtubule-depolymerizing kinesins. *Annual Review of Cell and Developmental Biology*, 29:417–441.

[Walczak and Shaw, 2010] Walczak, C. E. and Shaw, S. L. (2010). A MAP for bundling microtubules. *Cell*, 142(3):364–367.

[Whitman, 2016] Whitman, M. C. (2016). Two Unique TUBB3 Mutations Cause Both CFEOM3 and Malformations of Cortical Development. *Swaiman's Pediatric Neurology*, 32(3):211–227.

[Xu et al., 2017] Xu, X., Shangguan, Y., Lu, S., Wang, W., Du, C., Xiao, F., Hu, Y., Luo, J., Wang, L., He, C., Yang, Y., Zhang, Y., Lu, X., Yang, Q., and Wang, X. (2017). Tubulin β-III modulates seizure activity in epilepsy. *Journal of Pathology*, 242(3):297–308.

[Yau et al., 2016] Yau, K. W., Schatzle, P., Tortosa, E., Pages, S., Holtmaat, A., Kapitein, L. C., and Hoogenraad, C. C. (2016). Dendrites In Vitro and In Vivo Contain Microtubules of Opposite Polarity and Axon Formation Correlates with Uniform Plus-End-Out Microtubule Orientation. *Journal of Neuroscience*, 36(4):1071–1085.

[Yau et al., 2014] Yau, K. W., VanBeuningen, S. F. B., Cunha-Ferreira, I., Cloin, B. M. C., VanBattum, E. Y., Will, L., Sch??tzle, P., Tas, R. P., VanKrugten, J., Katrukha, E. A., Jiang, K., Wulf, P. S., Mikhaylova, M., Harterink, M., Pasterkamp, R. J., Akhmanova, A., Kapitein, L. C., and Hoogenraad, C. C. (2014). Microtubule minus-end binding protein CAMSAP2 controls axon specification and dendrite development. *Neuron*, 82(5):1058–1073.

[Yu et al., 2016] Yu, N., Signorile, L., Basu, S., Ottema, S., Lebbink, J. H., Leslie, K., Smal, I., Dekkers, D., Demmers, J., and Galjart, N. (2016). Isolation of Functional Tubulin Dimers and of Tubulin-Associated Proteins from Mammalian Cells. *Current Biology*, 26(13):1728–1736.

[Yue et al., 2014] Yue, F., Cheng, Y., Breschi, A., Vierstra, J., Wu, W., Ryba, T., Sandstrom, R., Ma, Z., Davis, C., Pope, B. D., and More (2014). A comparative encyclopedia of DNA elements in the mouse genome. *Nature*, 515(7527):355–364.

[Zhang et al., 2015] Zhang, R., Alushin, G. M., Brown, A., and Nogales, E. (2015). Mechanistic origin of microtubule dynamic instability and its modulation by EB proteins. *Cell*, 162(4):849–859.

A. Appendix

A.1. ImageJ Macro for video analysis

```
macro "Man_Track" {

Dialog.create("Scale");
   // produces a dialogbox with the title "Scale"
   // the user should enter the pixelsize with unit and the framerate of the
      imaging, the given values are for our spinning disc microscope with
      100x objective
Dialog.addNumber("pixel:", 1);
Dialog.addNumber("known distance:", 0.08);
Dialog.addString("unit:", "um");
Dialog.addNumber("frame rate [s]:", 1);
Dialog.show();
   //shows the dialog box

pixel = Dialog.getNumber();
   //the macro gets the numbers and units from the dialogbox
known = Dialog.getNumber();;
unit = Dialog.getString();
framerate = Dialog.getNumber();;;

run("Set Scale...", "distance=pixel known=known pixel=1 unit=unit");
   //the scale of the current image is set to the values that the user
     entered in the dialog box
run("Set Measurements...", "display redirect=None decimal=3");
   //the settings of measurements are set
setTool("line");
   //selects the line tool
run("ROI Manager...");
   //opens the roi manager
roiManager("Show All");
   //checks the box that all rois are visible in all frames

title1 = "Tracks";
   //sets the title for the later produced table
title2 = "["+title1+"]";
```

```
f=title2;
   //f is the variable for the table

run("New... ", "name="+title2+" type=Table");
   //produces a table
print(f,"\\Headings:Track\tLabel\tlength ["+unit+"]\tduration [s]
      \tvelocity ["+unit+"/s]");
   //shows the table with the given headings
setKeyDown("none");
   //deselects all keys that might have been pressed before
j = 1;
   //gives later the number of the track
count2 = 1;
   //counts the rows of the current track in the result table for the
     calculation of the length of that track
k = 0;
   // counts the clicks inside the image and gives the row for the result
      table

while (!(isKeyDown("alt"))) {
           //this while loop is executed until the alt key is pressed
        IJ.log("Close this window to start a new Track.\nPress Alt and
                    close this window after the last Track.")
           //opens a log window with the given text
        x2=-1; y2=-1; z2=-1; flags2=-1;
           //requirement for the get cursor location command
        logOpened = false;
           //argument for the next while loop
        slice1 = -2;
           //argument for a later if loop, just needed a number which could
             never be equal to slice1 so that the if loop is executed at
             least once

        while (!logOpened || isOpen("Log")) {
           // executes this while loop as long as the log window is opened
                getCursorLoc(x, y, z, flags);
                   //gets the cursor locations all the times, remembers the
                     x,y and z position(frame), the flag is a number which
                     gives the clicking of the mouse button

                if (x!=x2 || y!=y2 || z!=z2 || flags!=flags2) {

                        if (flags==48) {
                           //executes this if loop when the user presses the
                             left mouse button(flag of clicking the left is
                             48)

                              if (z != slice1) {
                                 //executes this if loop when z is not
```

```
85                              equal to slice1, as I set the initial
86                              value of slice1 to -2 and z is the
87                              frame of the stack (which is always
88                              a positive number) this loop is
89                              executed at least once
90
91                          title = getTitle();
92                             //gets the title of the current image
93                          setResult("Label", k, title);
94                             //the following lines fill the results
95                               table, k counts how often this loop
96                               is executed and with that counts the
97                               clicks (left mouse button) of the user
98                               on the image, the label is the title
99                                of the current image
100                         setResult("Track", k, j);
101                            //j counts the repetitions of the first
102                              while loop so it gives the number of
103                              the track
104                         setResult("X", k, x);
105                            // x and y positions of the cursor in
106                               pixel
107                         setResult("Y", k, y);
108                         setResult("Slice", k, z+1);
109                            //z gives the frame, but starts at 0,
110                            thats why I add 1
111                         k=k+1;
112                            //k counts how often this loop is executed
113                              and with that counts the clicks
114                              (left mouse button) of the user
115                              on the image
116                         slice1 = z;
117                            //sets slice1 to z, so if you click twice
118                              in the same frame the if loop is not
119                              executed
120
121                         } else {
122                            //if you click twice in the same frame
123                              this else loop is executed and gives
124                              you an error message
125
126                                 showMessage("Only one click per
127                                              frame allowed.");
128                                 }
129                         }
130                         updateResults();
131                            //updates the results table
132                         logOpened = true;
133                 }
```

```
134                     x2=x; y2=y; z2=z; flags2=flags;
135             }
136
137             dist = 0;
138                //sets the distance of the track to 0
139             count = 0;
140                //counts how often the following for loop is executed,
141                  so it counts the number of times you clicked in the
142                  current track
143
144             for (i=count2; i<nResults; i++) {
145                //count2 is set initially to 1 (1 is the second row in
146                  the result table), nResults is the number of entries
147                  in the result window, so this loop runs through all
148                  the rows in the result window of the current track
149
150                     x1 = getResult("X",i-1);
151                        //get the results for the x and y values of two
152                          consecutive points in the result table
153                     y1 = getResult("Y",i-1);
154                     x2 = getResult("X",i);
155                     y2 = getResult("Y",i);
156
157                     len = sqrt((x2-x1)*(x2-x1) + (y2-y1)*(y2-y1));
158                        //calculates the absolute distance between these
159                        two points
160                     dist = dist + len;
161                        //calculates the distance of the whole track by
162                        adding all the single distances between
163                        consecutive points of the track
164                     count = count + 1;
165                        //counts how often this for loop is executed,
166                        so it counts the number of times you clicked
167                        in the current track
168                     count2 = count2 + 1;
169                        //counts up count2 for the argument of this loop
170             }
171
172             count = count + 1;
173                //if the for loop is not executed anymore count still
174                has to be one larger to account for all the points in
175                the track
176             count2 = count2 + 1;
177             firstSlice = getResult("Slice",nResults - count);
178                //to caclulate the duration of the track we need the
179                  number of the first and the last frame of the stack,
180                  nresults is the last entry of the result table and
181                  count counted the number of points in the track,
182                  so by subtracting we get the first point of the track
```

```
183                 lastSlice = getResult("Slice",nResults-1);
184                 dur = framerate * abs(lastSlice - firstSlice);
185                    //by multiplying the framerate by the duration (in
186                      frames) we get the duration of the track in seconds
187                 vel = dist/dur;
188                    //the velocity is the distance devided by the duration
189                 label = getResultLabel(nResults-1);
190                    //gets the title of the current image out of the result
191                      tabel
192
193                 if(dur!=0) print(f, j +"\t"+ label +"\t"+dist*known/pixel+"\t
194                                  "+dur+"\t"+vel*known/pixel);
195                    //if the duration is not equal to 0 the results get
196                      printed into the "Tracks" table (f), j is the number
197                      of the track, label is the title of the image, the
198                      distance and the velocity have to be multiplied by
199                      the pixelsize which the user defines in the beginning,
200                      because x and y coordinates are given in pixel and
201                      distance and velocity shall be given in the pysical
202                      unit
203
204                 j = j + 1;
205                    //counts the repetitions of the first while loop and
206                    with that the number of tracks
207         }
208
209         setKeyDown("none");
210            //deselects all keys that might have been pressed before
211         selectWindow("ROI Manager");
212            //all opened windows get closed
213         roiManager("reset");
214         run("Close");
215
216         selectWindow("Results");
217         run("Close");
218
219         selectWindow("Tracks");
220         run("Close");
221 }
```

A.2. Microtubule growth model

```
using System;

namespace MT_growth_velocity
{
class Program
{
static void Main(string[] args)
{

int steps = 5000;
   // number of events that are calculated
int startlength = 10;
   // startlength of each protofilament is 10 dimers
double konuser = 30;
   // k_on defined by the user

double Glong1;
// longitudinal energy of Tubb3
double Glong2;
// longitudinal energy of Tubb4
double Glong3;
// longitudinal energy of the remaining isotypes
double Glong4;
// longitudinal energy between Tubb3 and Tubb4
double Glong5;
// longitudinal energy between Tubb3 and the remaining isotypes
double Glong6;
// longitudinal energy between Tubb4 and the remaining isotypes

double Glat1;
   // lateral energy of Tubb3
double Glat2;
   // lateral energy of Tubb4
double Glat3;
   // lateral energy of the remaining isotypes
double Glat4;
   // lateral energy between Tubb3 and Tubb4
double Glat5;
   // lateral energy between Tubb3 and the remaining isotypes
double Glat6;
   // lateral energy between Tubb4 and the remaining isotypes


double conc1 = 0.98;
   // dimer concentration of Tubb3 in the control condition
double conc2 = 1.96;
```

```
47     // dimer concentration of Tubb4 in the control condition
48  double conc3 = 4.06;
49     // dimer concentration of the remaining isotypes in the control
50        condition
51
52  //double conc1 = 0.42;
53     // dimer concentration of Tubb3 in the knock down condition
54  //double conc2 = 2.61;
55     // dimer concentration of Tubb4 in the knock down condition
56  //double conc3 = 3.97;
57     // dimer concentration of the remaining isotypes in the knock down
58        condition
59
60  double kon1 = konuser * conc1;
61     // on rate of Tubb3 multiplied with Tubb3 dimer concentration
62  double kon2 = konuser * conc2;
63     // on rate of Tubb4 multiplied with Tubb4 dimer concentration
64  double kon3 = konuser * conc3;
65     // on rate the remaining isotypes multiplied with their dimer
66        concentration
67
68  double koff;
69     // off rate constant
70  int[] length = new int[15];
71     // array to save the length of the protofilaments
72  int[,] grid = new int[15, steps + startlength + 2];
73     // 2D array to save the dimer types at their position in the MT grid
74  double[,] time = new double[14, steps + startlength + 5];
75     // 2D grid to save the execution time of each event
76  int[] x = { 1, 2, 3 };
77  double[] vel = new double[101];
78     // double to save the velocities
79  double smallest;
80  double meanvel;
81  double MTmeanlength;
82  int row;
83  int protofilament;
84  double totaltime;
85  double totallength;
86  double addedlength;
87  double MTlengthdiff;
88  int dimer1;
89  int dimer2;
90  int dimer3;
91  double latneighbor1;
92  double latneighbor2;
93  double latneighbor3;
94  double latneighbor4;
95  double latneighbor5;
```

```
96  double latneighbor6;
97  double longneighbor1;
98  double longneighbor2;
99  double longneighbor3;
100 double longneighbor4;
101 double longneighbor5;
102 double longneighbor6;
103
104 Random rnd = new Random();
105
106 Glong1 = -5;
107 // longitudinal energy of Tubb3
108 Glong2 = -7.5;
109 // longitudinal energy of Tubb4
110 Glong3 = -7;
111 // longitudinal energy of the remaining isotypes
112 Glong4 = (Glong1 + Glong2) / 2;
113 // longitudinal energy between Tubb3 and Tubb4
114 Glong5 = (Glong1 + Glong3) / 2;
115 // longitudinal energy between Tubb3 and the remaining isotypes
116 Glong6 = (Glong2 + Glong3) / 2;
117 // longitudinal energy between Tubb4 and the remaining isotypes
118
119 Glat1 = -3;
120    // lateral energy of Tubb3
121 Glat2 = -6;
122    // lateral energy of Tubb4
123 Glat3 = -4;
124    // lateral energy of the remaining isotypes
125 Glat4 = (Glat1 + Glat2) / 2;
126    // lateral energy between Tubb3 and Tubb4
127 Glat5 = (Glat1 + Glat3) / 2;
128    // lateral energy between Tubb3 and the remaining isotypes
129 Glat6 = (Glat2 + Glat3) / 2;
130    // lateral energy between Tubb4 and the remaining isotypes
131
132 Array.Clear(vel, 0, vel.Length);
133    // deletes all values in the velocity array and sets them to 0
134
135 for (int w = 1; w <= 100; w++)
136    // everything in this loop is executed 100 times
137 {
138   Array.Clear(grid, 0, grid.Length);
139      // deletes all values in the grid array and sets them to 0
140   length = new int[] { startlength, startlength, startlength, startlength,
141   startlength, startlength, startlength, startlength, startlength, startlength,
142   startlength, startlength, startlength, startlength, startlength };
143      // initializes the startlength of 70 dimers for each protofilament
144   row = 0;
```

```
145   protofilament = 0;
146   totaltime = 0;
147   totallength = 0;
148
149   for (int g = 1; g <= 13; g++)
150      // runs through protofilaments from 1 to 13
151   {
152     for (int h = 1; h <= startlength; h++)
153        // runs through the dimers of the protofilament from 1 to the set
154           startlength (10)
155     {
156       grid[g, h] = x[(rnd).Next(3)];
157          // puts a dimer of a rondom type (1,2 or 3) at this grid position
158     }
159   }
160      // with this a starting grid for the MT is defined
161
162   for (int i = 1; i <= steps; i++)
163      // runs through the events that are executed
164   {
165     Array.Clear(time, 0, time.Length);
166        // deletes all values in the time array and sets them to 0
167     for (int j = 1; j <= 13; j++)
168        // runs through the protofilaments
169     {
170       int s1 = 1;
171
172       while (grid[j, s1] != 0)
173          // this loop is executed as long as a dimer of type 1,2 or 3
174             sits at this grid position, it calculates the off rate constant
175             for each dimer in the lattice and the execution time of each
176             dimer to unbind from the lattice
177       {
178         double countlat1 = 0;
179            // number of lateral neighboring Tubb3 dimers
180         double countlat2 = 0;
181            // number of lateral neighboring Tubb4 dimers
182         double countlat3 = 0;
183            // number of lateral neighboring dimers of the remaining isotypes
184         double countlat4 = 0;
185            // number of lateral neighboring Tubb3 and Tubb4 dimers
186         double countlat5 = 0;
187            // number of lateral neighboring Tubb3 and remaining isotype dimers
188         double countlat6 = 0;
189            // number of lateral neighboring Tubb4 and remaining isotype dimers
190
191         double countlong1 = 0;
192            // number of longitudinal neighboring Tubb3 dimers
193         double countlong2 = 0;
```

```
194            // number of longitudinal neighboring Tubb4 dimers
195         double countlong3 = 0;
196            // number of longitudinal neighboring dimers of the remaining
197               isotypes
198         double countlong4 = 0;
199            // number of longitudinal neighboring Tubb3 and Tubb4 dimers
200         double countlong5 = 0;
201            // number of longitudinal neighboring Tubb3 and remaining
202               isotype dimers
203         double countlong6 = 0;
204            // number of longitudinal neighboring Tubb4 and remaining
205               isotype dimers
206
207         if (grid[j, s1] == 1)
208            // goes into this loop if the dimer type is 1 (Tubb3)
209               calculations of longitudinal neighbor dimer types for the
210               current dimer
211            {
212                    if (grid[j, s1 - 1] == 1) { countlong1 += 1; }
213                    if (grid[j, s1 - 1] == 2) { countlong4 += 1; }
214                    if (grid[j, s1 - 1] == 3) { countlong5 += 1; }
215            }
216
217         if (grid[j, s1] == 2)
218            // goes into this loop if the dimer type is 2 (Tubb4)
219               calculations of longitudinal neighbor dimer types for the
220               current dimer
221            {
222                    if (grid[j, s1 - 1] == 1) { countlong4 += 1; }
223                    if (grid[j, s1 - 1] == 2) { countlong2 += 1; }
224                    if (grid[j, s1 - 1] == 3) { countlong6 += 1; }
225            }
226
227         if (grid[j, s1] == 3)
228            // goes into this loop if the dimer type is 3 (all ramaining
229               isotypes) calculations of longitudinal neighbor dimer types
230               for the current dimer
231            {
232                    if (grid[j, s1 - 1] == 1) { countlong5 += 1; }
233                    if (grid[j, s1 - 1] == 2) { countlong6 += 1; }
234                    if (grid[j, s1 - 1] == 3) { countlong3 += 1; }
235            }
236
237         int s2 = s1;
238
239         while (grid[j, s2] != 0)
240           // this loop is executed as long as a dimer of type 1,2 or 3 sits at
241              this grid position
242         {
```

```
243             if (j == 1)
244                // this loop calculates the number of lateral neighbors for
245                   protofilament 1, because of the MT seam between protofilament
246                   1 and 13 with a longitudinal dimer shift of 1.5 dimers, the
247                   lateral neighbors for protofilament 1 and 13 have to be
248                   calculated seperately from the rest
249             {
250               if (grid[j, s2] == 1)
251                  // goes into this loop if the dimer type is 1 (Tubb3)
252               {
253                 if (s2 == 1)
254                    // calculations of lateral neighbor dimer types for the
255                       first dimer of protofilament 1
256                 {
257                   if (grid[2, s2] == 1) { countlat1 = countlat1 + 1; }
258                   if (grid[2, s2] == 2) { countlat4 = countlat4 + 1; }
259                   if (grid[2, s2] == 3) { countlat5 = countlat5 + 1; }
260                   if (grid[13, s2] == 1) { countlat1 = countlat1 + 1; }
261                   if (grid[13, s2] == 2) { countlat4 = countlat4 + 1; }
262                   if (grid[13, s2] == 3) { countlat5 = countlat5 + 1; }
263                 }
264
265                 if (s2 == 2)
266                    // calculations of lateral neighbor dimer types for the
267                       second dimer of protofilament 1
268                 {
269                   if (grid[2, s2] == 1) { countlat1 = countlat1 + 1; }
270                   if (grid[2, s2] == 2) { countlat4 = countlat4 + 1; }
271                   if (grid[2, s2] == 3) { countlat5 = countlat5 + 1; }
272                   if (grid[13, s2 - 1] == 1) { countlat1 = countlat1 + 1; }
273                   if (grid[13, s2 - 1] == 2) { countlat4 = countlat4 + 1; }
274                   if (grid[13, s2 - 1] == 3) { countlat5 = countlat5 + 1; }
275                 }
276
277                 if (s2 != 1 && s2 != 2)
278                    // calculations of lateral neighbor dimer types for all
279                       following dimers of protofilament 1
280                 {
281                   if (grid[2, s2] == 1) { countlat1 = countlat1 + 1; }
282                   if (grid[2, s2] == 2) { countlat4 = countlat4 + 1; }
283                   if (grid[2, s2] == 3) { countlat5 = countlat5 + 1; }
284                   if (grid[13, s2 - 2] == 1) { countlat1 = countlat1 + 0.5; }
285                   if (grid[13, s2 - 2] == 2) { countlat4 = countlat4 + 0.5; }
286                   if (grid[13, s2 - 2] == 3) { countlat5 = countlat5 + 0.5; }
287                   if (grid[13, s2 - 1] == 1) { countlat1 = countlat1 + 0.5; }
288                   if (grid[13, s2 - 1] == 2) { countlat4 = countlat4 + 0.5; }
289                   if (grid[13, s2 - 1] == 3) { countlat5 = countlat5 + 0.5; }
290                 }
291               }
```

```
292
293             if (grid[j, s2] == 2)
294                // goes into this loop if the dimer type is 2 (Tubb4)
295             {
296               if (s2 == 1)
297                  // calculations of lateral neighbor dimer types for the
298                     first dimer of protofilament 1
299               {
300                 if (grid[2, s2] == 1) { countlat4 = countlat4 + 1; }
301                 if (grid[2, s2] == 2) { countlat2 = countlat2 + 1; }
302                 if (grid[2, s2] == 3) { countlat6 = countlat6 + 1; }
303                 if (grid[13, s2] == 1) { countlat4 = countlat4 + 1; }
304                 if (grid[13, s2] == 2) { countlat2 = countlat2 + 1; }
305                 if (grid[13, s2] == 3) { countlat6 = countlat6 + 1; }
306               }
307
308               if (s2 == 2)
309                  // calculations of lateral neighbor dimer types for the
310                     second dimer of protofilament 1
311               {
312                 if (grid[2, s2] == 1) { countlat4 = countlat4 + 1; }
313                 if (grid[2, s2] == 2) { countlat2 = countlat2 + 1; }
314                 if (grid[2, s2] == 3) { countlat6 = countlat6 + 1; }
315                 if (grid[13, s2 - 1] == 1) { countlat4 = countlat4 + 1; }
316                 if (grid[13, s2 - 1] == 2) { countlat2 = countlat2 + 1; }
317                 if (grid[13, s2 - 1] == 3) { countlat6 = countlat6 + 1; }
318               }
319
320               if (s2 != 1 && s2 != 2)
321                  // calculations of lateral neighbor dimer types for all
322                     following dimers of protofilament 1
323               {
324                 if (grid[2, s2] == 1) { countlat4 = countlat4 + 1; }
325                 if (grid[2, s2] == 2) { countlat2 = countlat2 + 1; }
326                 if (grid[2, s2] == 3) { countlat6 = countlat6 + 1; }
327                 if (grid[13, s2 - 2] == 1) { countlat4 = countlat4 + 0.5; }
328                 if (grid[13, s2 - 2] == 2) { countlat2 = countlat2 + 0.5; }
329                 if (grid[13, s2 - 2] == 3) { countlat6 = countlat6 + 0.5; }
330                 if (grid[13, s2 - 1] == 1) { countlat4 = countlat4 + 0.5; }
331                 if (grid[13, s2 - 1] == 2) { countlat2 = countlat2 + 0.5; }
332                 if (grid[13, s2 - 1] == 3) { countlat6 = countlat6 + 0.5; }
333               }
334             }
335
336             if (grid[j, s2] == 3)
337                // goes into this loop if the dimer type is 3 (all ramaining
338                   isotypes)
339             {
340               if (s2 == 1)
```

```
341                 // calculations of lateral neighbor dimer types for the
342                    first dimer of protofilament 1
343               {
344                 if (grid[2, s2] == 1) { countlat5 = countlat5 + 1; }
345                 if (grid[2, s2] == 2) { countlat6 = countlat6 + 1; }
346                 if (grid[2, s2] == 3) { countlat3 = countlat3 + 1; }
347                 if (grid[13, s2] == 1) { countlat5 = countlat5 + 1; }
348                 if (grid[13, s2] == 2) { countlat6 = countlat6 + 1; }
349                 if (grid[13, s2] == 3) { countlat3 = countlat3 + 1; }
350               }
351
352               if (s2 == 2)
353                  // calculations of lateral neighbor dimer types for the
354                     second dimer of protofilament 1
355               {
356                 if (grid[2, s2] == 1) { countlat5 = countlat5 + 1; }
357                 if (grid[2, s2] == 2) { countlat6 = countlat6 + 1; }
358                 if (grid[2, s2] == 3) { countlat3 = countlat3 + 1; }
359                 if (grid[13, s2 - 1] == 1) { countlat5 = countlat5 + 1; }
360                 if (grid[13, s2 - 1] == 2) { countlat6 = countlat6 + 1; }
361                 if (grid[13, s2 - 1] == 3) { countlat3 = countlat3 + 1; }
362               }
363
364               if (s2 != 1 && s2 != 2)
365                  // calculations of lateral neighbor dimer types for all
366                     following dimers of protofilament 1
367               {
368                 if (grid[2, s2] == 1) { countlat5 = countlat5 + 1; }
369                 if (grid[2, s2] == 2) { countlat6 = countlat6 + 1; }
370                 if (grid[2, s2] == 3) { countlat3 = countlat3 + 1; }
371                 if (grid[13, s2 - 2] == 1) { countlat5 = countlat5 + 0.5; }
372                 if (grid[13, s2 - 2] == 2) { countlat6 = countlat6 + 0.5; }
373                 if (grid[13, s2 - 2] == 3) { countlat3 = countlat3 + 0.5; }
374                 if (grid[13, s2 - 1] == 1) { countlat5 = countlat5 + 0.5; }
375                 if (grid[13, s2 - 1] == 2) { countlat6 = countlat6 + 0.5; }
376                 if (grid[13, s2 - 1] == 3) { countlat3 = countlat3 + 0.5; }
377               }
378             }
379           }
380
381           if (j == 13)
382              // this loop calculates the number of lateral neighbors for
383                 protofilament 13, because of the MT seam between protofilament
384                 1 and 13 with a longitudinal dimer shift of 1.5 dimers, the
385                 lateral neighbors for protofilament 1 and 13 have to be
386                 calculated seperately from the rest
387           {
388             if (grid[j, s2] == 1)
389                // goes into this loop if the dimer type is 1 (Tubb3)
```

```
390             {
391               if (grid[12, s2] == 1) { countlat1 = countlat1 + 1; }
392               if (grid[12, s2] == 2) { countlat4 = countlat4 + 1; }
393               if (grid[12, s2] == 3) { countlat5 = countlat5 + 1; }
394               if (grid[1, s2 + 1] == 1) { countlat1 = countlat1 + 0.5; }
395               if (grid[1, s2 + 1] == 2) { countlat4 = countlat4 + 0.5; }
396               if (grid[1, s2 + 1] == 3) { countlat5 = countlat5 + 0.5; }
397               if (grid[1, s2 + 2] == 1) { countlat1 = countlat1 + 0.5; }
398               if (grid[1, s2 + 2] == 2) { countlat4 = countlat4 + 0.5; }
399               if (grid[1, s2 + 2] == 3) { countlat5 = countlat5 + 0.5; }
400             }
401
402             if (grid[j, s2] == 2)
403                // goes into this loop if the dimer type is 2 (Tubb4)
404             {
405               if (grid[12, s2] == 1) { countlat4 = countlat4 + 1; }
406               if (grid[12, s2] == 2) { countlat2 = countlat2 + 1; }
407               if (grid[12, s2] == 3) { countlat6 = countlat6 + 1; }
408               if (grid[1, s2 + 1] == 1) { countlat4 = countlat4 + 0.5; }
409               if (grid[1, s2 + 1] == 2) { countlat2 = countlat2 + 0.5; }
410               if (grid[1, s2 + 1] == 3) { countlat6 = countlat6 + 0.5; }
411               if (grid[1, s2 + 2] == 1) { countlat4 = countlat4 + 0.5; }
412               if (grid[1, s2 + 2] == 2) { countlat2 = countlat2 + 0.5; }
413               if (grid[1, s2 + 2] == 3) { countlat6 = countlat6 + 0.5; }
414             }
415
416             if (grid[j, s2] == 3)
417                // goes into this loop if the dimer type is 3 (all ramaining
418                   isotypes)
419             {
420               if (grid[12, s2] == 1) { countlat5 = countlat5 + 1; }
421               if (grid[12, s2] == 2) { countlat6 = countlat6 + 1; }
422               if (grid[12, s2] == 3) { countlat3 = countlat3 + 1; }
423               if (grid[1, s2 + 1] == 1) { countlat5 = countlat5 + 0.5; }
424               if (grid[1, s2 + 1] == 2) { countlat6 = countlat6 + 0.5; }
425               if (grid[1, s2 + 1] == 3) { countlat3 = countlat3 + 0.5; }
426               if (grid[1, s2 + 2] == 1) { countlat5 = countlat5 + 0.5; }
427               if (grid[1, s2 + 2] == 2) { countlat6 = countlat6 + 0.5; }
428               if (grid[1, s2 + 2] == 3) { countlat3 = countlat3 + 0.5; }
429             }
430           }
431
432           if (j != 1 && j != 13)
433              // this loop calculates the number of lateral neighbors for
434                 protofilament 2 to 12
435           {
436             if (grid[j, s2] == 1)
437                // goes into this loop if the dimer type is 1 (Tubb3)
438               {
```

```
439               if (grid[j + 1, s2] == 1) { countlat1 = countlat1 + 1; }
440               if (grid[j + 1, s2] == 2) { countlat4 = countlat4 + 1; }
441               if (grid[j + 1, s2] == 3) { countlat5 = countlat5 + 1; }
442               if (grid[j - 1, s2] == 1) { countlat1 = countlat1 + 1; }
443               if (grid[j - 1, s2] == 2) { countlat4 = countlat4 + 1; }
444               if (grid[j - 1, s2] == 3) { countlat5 = countlat5 + 1; }
445             }
446
447             if (grid[j, s2] == 2)
448                // goes into this loop if the dimer type is 2 (Tubb4)
449             {
450               if (grid[j + 1, s2] == 1) { countlat4 = countlat4 + 1; }
451               if (grid[j + 1, s2] == 2) { countlat2 = countlat2 + 1; }
452               if (grid[j + 1, s2] == 3) { countlat6 = countlat6 + 1; }
453               if (grid[j - 1, s2] == 1) { countlat4 = countlat4 + 1; }
454               if (grid[j - 1, s2] == 2) { countlat2 = countlat2 + 1; }
455               if (grid[j - 1, s2] == 3) { countlat6 = countlat6 + 1; }
456             }
457
458             if (grid[j, s2] == 3)
459                // goes into this loop if the dimer type is 3 (all
460                   ramaining isotypes)
461             {
462               if (grid[j + 1, s2] == 1) { countlat5 = countlat5 + 1; }
463               if (grid[j + 1, s2] == 2) { countlat6 = countlat6 + 1; }
464               if (grid[j + 1, s2] == 3) { countlat3 = countlat3 + 1; }
465               if (grid[j - 1, s2] == 1) { countlat5 = countlat5 + 1; }
466               if (grid[j - 1, s2] == 2) { countlat6 = countlat6 + 1; }
467               if (grid[j - 1, s2] == 3) { countlat3 = countlat3 + 1; }
468             }
469           }
470           s2++;
471              // the value of s2 is increased by 1, with this the program
472                 jumps to the next dimer in the protofilament and calculates
473                 its lateral neighbors; because if a dimer deep in the
474                 lattice unbinds all the dimers above it unbind and all
475                 lateral energies have to be summed up
476         }
477
478         double sum_Glat = (countlat1 * Glat1) + (countlat2 * Glat2) +
479         (countlat3 * Glat3) + (countlat4 * Glat4) + (countlat5 * Glat5)
480         + (countlat6 * Glat6);
481           // calculates the total lateral energy of the current dimer
482         double sum_Glong = (countlong1 * Glong1) + (countlong2 * Glong2)
483         + (countlong3 * Glong3) + (countlong4 * Glong4) + (countlong5 *
484         Glong5) + (countlong6 * Glong6);
485           // calculates the total longitudinal energy of the current dimer
486
487         koff = konuser / Math.Exp(-1 * (sum_Glat + sum_Glong)) * 100000;
```

```
488             // calculates the off rate constant of the current dimer
489           time[j, s1] = -Math.Log(rnd.NextDouble()) / koff;
490             // calculates the execution time of the current dimer to unbind
491
492           s1++;
493              // the value of s1 is increased by 1, with this the program
494                 jumps to the next dimer in the protofilament to calculate
495                 the number of lateral neighbors of this and all the above
496                 dimers
497         }
498
499         if (j == 1)
500            // this loop calculates the executions times of dimers binding to
501               protofilament 1
502         {
503           if (length[1] > 0 && grid[13, length[1] - 1] != 0 &&
504               grid[2, length[1] + 1] != 0)
505              // goes into this loop if protofilament 1 has a length greater
506                 than 0, and is shorter than protofilaments 13 and 2
507           {
508             time[j, 0] = -Math.Log(rnd.NextDouble()) / (kon1 / 10);
509             time[j, steps + startlength + 3] =
510                  -Math.Log(rnd.NextDouble()) / (kon2 / 10);
511             time[j, steps + startlength + 4] =
512                  -Math.Log(rnd.NextDouble()) / (kon3 / 10);
513                // the execution times of dimers of type 1, 2 or 3 binding
514                   to the protofilament tip are calculated
515           }
516           else
517           {
518             if (length[1] > 0 && grid[13, length[1] - 1] == 0 &&
519                 grid[2, length[1] + 1] == 0)
520                // goes into this loop if protofilament 1 has a length greater
521                   than 0, and is longer or of the same length than
522                   protofilaments 13 and 2
523             {
524               time[j, 0] = -Math.Log(rnd.NextDouble()) / (kon1);
525               time[j, steps + startlength + 3] =
526                    -Math.Log(rnd.NextDouble()) / (kon2);
527               time[j, steps + startlength + 4] =
528                    -Math.Log(rnd.NextDouble()) / (kon3);
529                  // the execution times of dimers of type 1, 2 or 3
530                     binding to the protofilament tip are calculated
531             }
532             else
533                // this loop is executed when protofilament 1 is shorter than
534                   one of the neighboring protofilaments and longer than the
535                   other
536             {
```

```
537               time[j, 0] = -Math.Log(rnd.NextDouble()) / (kon1 / 2);
538               time[j, steps + startlength + 3] =
539                    -Math.Log(rnd.NextDouble()) / (kon2 / 2);
540               time[j, steps + startlength + 4] =
541                   -Math.Log(rnd.NextDouble()) / (kon3 / 2);
542                  // the execution times of dimers of type 1, 2 or 3
543                     binding to the protofilament tip are calculated
544             }
545           }
546         }
547
548         if (j == 13)
549            // this loop calculates the executions times of dimers binding
550               to protofilament 13
551         {
552           if (grid[12, length[13] + 1] != 0 && grid[1, length[13] + 2] != 0)
553              // goes into this loop if protofilament 13 is shorter than
554                 protofilaments 12 and 1
555           {
556             time[j, 0] = -Math.Log(rnd.NextDouble()) / (kon1 / 10);
557             time[j, steps + startlength + 3] =
558                  -Math.Log(rnd.NextDouble()) / (kon2 / 10);
559             time[j, steps + startlength + 4] =
560                  -Math.Log(rnd.NextDouble()) / (kon3 / 10);
561                // the execution times of dimers of type 1, 2 or 3
562                   binding to the protofilament tip are calculated
563           }
564           else
565           {
566             if (grid[12, length[13] + 1] == 0 && grid[1, length[13] + 2] == 0)
567                // goes into this loop if protofilament 1 is longer or of the
568                   same length than protofilaments 13 and 2
569             {
570               time[j, 0] = -Math.Log(rnd.NextDouble()) / (kon1);
571               time[j, steps + startlength + 3] =
572                    -Math.Log(rnd.NextDouble()) / (kon2);
573               time[j, steps + startlength + 4] =
574                    -Math.Log(rnd.NextDouble()) / (kon3);
575                  // the execution times of dimers of type 1, 2 or 3
576                     binding to the protofilament tip are calculated
577             }
578             else
579                // this loop is executed when protofilament 13 is shorter than
580                   one of the neighboring protofilaments and longer than the
581                   other
582             {
583               time[j, 0] = -Math.Log(rnd.NextDouble()) / (kon1 / 2);
584               time[j, steps + startlength + 3] =
585                    -Math.Log(rnd.NextDouble()) / (kon2 / 2);
```

```
586               time[j, steps + startlength + 4] =
587                    -Math.Log(rnd.NextDouble()) / (kon3 / 2);
588                  // the execution times of dimers of type 1, 2 or 3
589                     binding to the protofilament tip are calculated
590             }
591           }
592         }
593
594         if (j != 1 && j != 13)
595            // this loop calculates the executions times of dimers binding
596               to protofilaments 2 to 12
597         {
598
599           if (grid[j - 1, length[j] + 1] != 0 && grid[j + 1, length[j] + 1] != 0)
600              // goes into this loop if the current protofilament is shorter
601                 than its two neighboring protofilaments
602           {
603             time[j, 0] = -Math.Log(rnd.NextDouble()) / (kon1 / 10);
604             time[j, steps + startlength + 3] =
605                  -Math.Log(rnd.NextDouble()) / (kon2 / 10);
606             time[j, steps + startlength + 4] =
607                 -Math.Log(rnd.NextDouble()) / (kon3 / 10);
608           }
609           else
610           {
611             if (grid[j - 1, length[j] + 1] == 0 && grid[j + 1, length[j] + 1] == 0)
612                // goes into this loop if the current protofilament is longer
613                   or of the same length than its two neighboring protofilaments
614             {
615               time[j, 0] = -Math.Log(rnd.NextDouble()) / (kon1);
616               time[j, steps + startlength + 3] =
617                    -Math.Log(rnd.NextDouble()) / (kon2);
618               time[j, steps + startlength + 4] =
619                    -Math.Log(rnd.NextDouble()) / (kon3);
620             }
621             else
622                // this loop is executed when the current protofilament is
623                   shorter than one of the neighboring protofilaments and
624                   longer than  the other
625             {
626               time[j, 0] = -Math.Log(rnd.NextDouble()) / (kon1 / 2);
627               time[j, steps + startlength + 3] =
628                    -Math.Log(rnd.NextDouble()) / (kon2 / 2);
629               time[j, steps + startlength + 4] =
630                    -Math.Log(rnd.NextDouble()) / (kon3 / 2);
631             }
632           }
633         }
634       }
```

```
635
636         smallest = time[1, 0];
637
638         for (int k = 1; k <= 13; k++)
639         {
640           for (int l = 0; l <= steps + startlength + 4; l++)
641           {
642             if (time[k, l] != 0 && time[k, l] <= smallest)
643             {
644               smallest = time[k, l];
645               protofilament = k;
646               row = l;
647             }
648           }
649         }
650            // this loops determine the shortest execution time of all before
651               calculated times and saves the protofilament number and the row
652
653
654
655         if (row == 0)
656            // row = 0 means that a dimer of type 1 (Tubb3) binds to the
657               corresponding protofilament
658         {
659           length[protofilament] = length[protofilament] + 1;
660              // the length of the protofilament is increased by 1
661           grid[protofilament, length[protofilament]] = 1;
662              // the number in the grid array is set to 1
663         }
664         else
665         {
666           if (row == steps + startlength + 3)
667              // row = steps + startlength + 3 means that a dimer of type 2
668                 (Tubb4) binds to the corresponding protofilament
669           {
670             length[protofilament] = length[protofilament] + 1;
671                // the length of the protofilament is increased by 1
672             grid[protofilament, length[protofilament]] = 2;
673                // the number in the grid array is set to 2
674           }
675           else
676           {
677             if (row == steps + startlength + 4)
678                // row = steps + startlength + 4 means that a dimer of type 3
679                   (all remaining isotypes) binds to the corresponding
680                   protofilament
681             {
682               length[protofilament] = length[protofilament] + 1;
683                  // the length of the protofilament is increased by 1
```

```
684             grid[protofilament, length[protofilament]] = 3;
685                // the number in the grid array is set to 3
686           }
687           else
688              // this loop is executed when a dimer unbinds
689           {
690             int countrow = row;
691                // sets the value of countrow to the value of row, which
692                   means the following while loop starts at the dimer with
693                   the shortest execution time
694
695             while (grid[protofilament, countrow] != 0)
696                // this loop is executed as long as the dimer type at this
697                   grid position is 1, 2 or 3
698             {
699               grid[protofilament, countrow] = 0;
700                  // removes the dimer from this grid position
701               length[protofilament] = length[protofilament] - 1;
702                  // the length of the protofilament is decreased by 1
703               countrow++;
704                  // increases the values of countrow by 1, which means that
705                     all dimers above the dimer with the shortest execution
706                     time are removed as well
707             }
708           }
709         }
710       }
711
712       totaltime = totaltime + smallest;
713          // calculates the total elapsed time by summing all calculated
714             execution times
715       DateTime start = DateTime.Now;
716          // sets the date and time to the current values, which are used
717             as seeds for the random numbers
718     }
719
720     addedlength = length[1] + length[2] + length[3] + length[4] + length[5] +
721                   length[6] + length[7] + length[8] + length[9] + length[10] +
722                   length[11] + length[12] + length[13];
723        // summes up the lengths of all protofilaments
724     MTmeanlength = addedlength / 13;
725        // calculates the mean MT length
726     MTlengthdiff = MTmeanlength - startlength;
727        // substracs the startlength of the protofilaments from the mean MT
728           length
729     totallength = MTlengthdiff * 8;
730        // transforms the lenfth from number of dimers into nm (length of 1
731           dimer is 8 nm)
732
```

```
733     vel[w] = totallength / totaltime;
734        // calculates the velocity
735
736     dimer1 = 0;
737     dimer2 = 0;
738     dimer3 = 0;
739     latneighbor1 = 0;
740     latneighbor2 = 0;
741     latneighbor3 = 0;
742     latneighbor4 = 0;
743     latneighbor5 = 0;
744     latneighbor6 = 0;
745     longneighbor1 = 0;
746     longneighbor2 = 0;
747     longneighbor3 = 0;
748     longneighbor4 = 0;
749     longneighbor5 = 0;
750     longneighbor6 = 0;
751
752     for (int j = 1; j <= 13; j++)
753       // runs through the protofilaments
754     {
755       for (int i = startlength + 1; i <= steps + startlength + 1; i++)
756         // starts counting the dimer types in the protofilaments above the
757            starting grid
758       {
759         if (grid[j, i] == 0)
760           // stops if there is no dimer at this space of the grid
761         {
762                    break;
763               }
764
765               if (grid[j, i] == 1) { dimer1 += 1; }
766               if (grid[j, i] == 2) { dimer2 += 1; }
767               if (grid[j, i] == 3) { dimer3 += 1; }
768                 // counts the number of incorporated dimer types
769
770               if (j == 1)
771                 // this loop calculates the dimer types of lateral neighbors
772                    for protofilament 1
773               {
774                 if (grid[j, i] == 1)
775                   // goes into this loop if the dimer type is 1 (Tubb3)
776                 {
777                   if (grid[j, i - 1] == 1) { longneighbor1 += 1; }
778                       if (grid[j, i - 1] == 2) { longneighbor4 += 1; }
779                       if (grid[j, i - 1] == 3) { longneighbor5 += 1; }
780                       if (grid[13, i - 2] == 1) { latneighbor1 += 0.5; }
781                       if (grid[13, i - 2] == 2) { latneighbor4 += 0.5; }
```

```
782                     if (grid[13, i - 2] == 3) { latneighbor5 += 0.5; }
783                     if (grid[13, i - 1] == 1) { latneighbor1 += 0.5; }
784                     if (grid[13, i - 1] == 2) { latneighbor4 += 0.5; }
785                     if (grid[13, i - 1] == 3) { latneighbor5 += 0.5; }
786                 }
787
788                 if (grid[j, i] == 2)
789                       // goes into this loop if the dimer type is 2 (Tubb4)
790                 {
791                 if (grid[j, i - 1] == 1) { longneighbor4 += 1; }
792                 if (grid[j, i - 1] == 2) { longneighbor2 += 1; }
793                 if (grid[j, i - 1] == 3) { longneighbor6 += 1; }
794                 if (grid[13, i - 2] == 1) { latneighbor4 += 0.5; }
795                 if (grid[13, i - 2] == 2) { latneighbor2 += 0.5; }
796                 if (grid[13, i - 2] == 3) { latneighbor6 += 0.5; }
797                 if (grid[13, i - 1] == 1) { latneighbor4 += 0.5; }
798                 if (grid[13, i - 1] == 2) { latneighbor2 += 0.5; }
799                 if (grid[13, i - 1] == 3) { latneighbor6 += 0.5; }
800                 }
801
802                 if (grid[j, i] == 3)
803                   // goes into this loop if the dimer type is 3 (all ramaining
804                           isotypes)
805                 {
806           if (grid[j, i - 1] == 1) { longneighbor5 += 1; }
807                     if (grid[j, i - 1] == 2) { longneighbor6 += 1; }
808                     if (grid[j, i - 1] == 3) { longneighbor3 += 1; }
809                     if (grid[13, i - 2] == 1) { latneighbor5 += 0.5; }
810                     if (grid[13, i - 2] == 2) { latneighbor6 += 0.5; }
811                     if (grid[13, i - 2] == 3) { latneighbor3 += 0.5; }
812                     if (grid[13, i - 1] == 1) { latneighbor5 += 0.5; }
813                     if (grid[13, i - 1] == 2) { latneighbor6 += 0.5; }
814                   if (grid[13, i - 1] == 3) { latneighbor3 += 0.5; }
815                 }
816               }
817
818               if (j != 1)
819                 // this loop calculates the dimer types of lateral neighbors
820                    for all other protofilament
821         {
822           if (grid[j, i] == 1)
823                     // goes into this loop if the dimer type is 1 (Tubb3)
824                 {
825                   if (grid[j, i - 1] == 1) { longneighbor1 += 1; }
826                     if (grid[j, i - 1] == 2) { longneighbor4 += 1; }
827                     if (grid[j, i - 1] == 3) { longneighbor5 += 1; }
828                     if (grid[j - 1, i] == 1) { latneighbor1 += 1; }
829                     if (grid[j - 1, i] == 2) { latneighbor4 += 1; }
830                     if (grid[j - 1, i] == 3) { latneighbor5 += 1; }
```

```
831                 }
832                 if (grid[j, i] == 2)
833                   // goes into this loop if the dimer type is 2 (Tubb4)
834                 {
835                   if (grid[j, i - 1] == 1) { longneighbor4 += 1; }
836                       if (grid[j, i - 1] == 2) { longneighbor2 += 1; }
837                       if (grid[j, i - 1] == 3) { longneighbor6 += 1; }
838                       if (grid[j - 1, i] == 1) { latneighbor4 += 1; }
839                       if (grid[j - 1, i] == 2) { latneighbor2 += 1; }
840                       if (grid[j - 1, i] == 3) { latneighbor6 += 1; }
841                 }
842                 if (grid[j, i] == 3)
843                   // goes into this loop if the dimer type is 3 (all ramaining
844                          isotypes)
845                 {
846                   if (grid[j, i - 1] == 1) { longneighbor5 += 1; }
847                       if (grid[j, i - 1] == 2) { longneighbor6 += 1; }
848                       if (grid[j, i - 1] == 3) { longneighbor3 += 1; }
849                       if (grid[j - 1, i] == 1) { latneighbor5 += 1; }
850                       if (grid[j - 1, i] == 2) { latneighbor6 += 1; }
851                       if (grid[j - 1, i] == 3) { latneighbor3 += 1; }
852                  }
853                }
854               }
855       }
856
857       int dimertotal = dimer1 + dimer2 + dimer3;
858         // calculates the total dimer amount in the MT
859       double lattotal = latneighbor1 + latneighbor2 + latneighbor3 +
860       latneighbor4 + latneighbor5 + latneighbor6;
861         // counts the total number of lateral connections
862       double longtotal = longneighbor1 + longneighbor2 + longneighbor3 +
863       longneighbor4 + longneighbor5 + longneighbor6;
864         // counts the total number of longitudinal connections
865
866       Console.WriteLine(Math.Round(vel[w], 4) + " ; " + dimertotal + " ;
867       " + dimer1 + " ; " + dimer2 + " ; " + dimer3 + " ; " + lattotal + " ;
868       " + latneighbor1 + " ; " + latneighbor2 + " ; " + latneighbor3 + " ; "
869       + latneighbor4 + " ; " + latneighbor5 + " ; " + latneighbor6 + " ; "
870       + longtotal + " ; " + longneighbor1 + " ; " + longneighbor2 + " ; "
871       + longneighbor3 + " ; " + longneighbor4 + " ; " + longneighbor5 + "
872       ; " + longneighbor6);
873       // writes the velocity and dimercounts into the console
874   }
875   Console.Read();
876      // keeps the console open until the user presses enter
877 }
878 }
879 }
```

A.3. Scientific contributions

A.3.1. Conferences

Co-coordination of the international DFG Research Unit FOR 2419 Symposium, Uncovering Synaptic Plasticity - From Molecules to Memory, February 16th, 2018

A.3.2. Scientific talks

DFG Research Unit FOR 2419 Symposium, Uncovering Synaptic Plasticity - From Molecules to Memory, February 16th, 2018
Short talk: The Role of Microtubule Isoforms in Neuronal Transport Processes.

A.3.3. Poster presentations

37th Blankenese Conference, Synaptic Plasticity versus Stability - Information Uptake, Processing and Coding, May 6th - 10th, 2017
Poster: Biophysical mechanisms of the microtubule network in synaptic transport processes.

DFG Research Unit FOR 2419 Symposium, Uncovering Synaptic Plasticity - From Molecules to Memory, February 16th, 2018
Poster: The Role of Microtubule Isoforms in Neuronal Transport Processes.

EMBO EMBL Symposium, Microtubules - From Atoms to Complex Systems, May 27th - 30th, 2018
Poster: The Role of Microtubule Isoforms in Neuronal Transport Processes.

A.3.4. Publications

Hausrat TJ, Radwitz J, Lombino FL, Breiden P, Kneussel M. Alpha- and beta-tubulin isotypes are differentially expressed during brain development. Dev Neurobiol. 2020. doi: 10.1002/dneu.22745.